NOVEL OPTICAL ANTENNAS INSPIRED BY METAMATERIAL ARCHITECTURES

A THESIS
SUBMITTED TO THE DEPARTMENT OF ELECTRICAL AND ELECTRONICS ENGINEERING
AND THE GRADUATE SCHOOL OF ENGINEERING AND SCIENCES
OF BILKENT UNIVERSITY
IN PARTIAL FULLFILMENT OF THE REQUIREMENTS
FOR THE DEGREE OF
MASTER OF SCIENCE

By
Veli Tayfun Kılıç
August 2011

I certify that I have read this thesis and that in my opinion it is fully adequate, in scope and in quality, as a thesis for the degree of Master of Science.

_____

Assoc. Prof. Dr. Hilmi Volkan Demir (Supervisor)

I certify that I have read this thesis and that in my opinion it is fully adequate, in scope and in quality, as a thesis for the degree of Master of Science.

_____

Assoc. Prof. Dr. Vakur B. Erturk

I certify that I have read this thesis and that in my opinion it is fully adequate, in scope and in quality, as a thesis for the degree of Master of Science.

_____

Prof. Dr. Sencer Koc

Approved for the Graduate School of Engineering and Sciences:

_____

Prof. Dr. Levent Onural

Director of Graduate School of Engineering and Sciences

ABSTRACT

NOVEL OPTICAL ANTENNAS INSPIRED BY METAMATERIAL ARCHITECTURES

Veli Tayfun Kilic
M.S. in Electrical and Electronics Engineering
Supervisor: Assoc. Prof. Dr. Hilmi Volkan Demir

August 2011

The spatial resolution of conventional optical systems is commonly constrained by the diffraction limit. This is a fundamental problem important for various high-tech applications including density limitation in data storage devices (CD, DVD, and Blue-ray discs), crosstalk in detectors, and blurred images in microscopy. To overcome this limit, different types of optical antennas have been investigated to date. However, these antennas either do not exhibit a maximum level of field intensity enhancement that can be achieved via field localization using plasmons or they have large field intensity enhancement at the cost of complicated three-dimensional architectures or very sharp tips, which are hard to fabricate. In this thesis, to address this problem, we investigate a new class of planar optical antennas inspired by metamaterial architectures including E-shape and comb shape. We found that the field intensity enhancements inside the gap regions of such comb-shaped nanoantennas were significantly increased compared to the single or array of dipoles, despite operating across an electrical length significantly reduced with respect to their resonance wavelength. We also showed that the field intensity localization of a single dipole nanoantenna can be at least doubled using single ring resonator with the same gap size by decreasing field radiations from end points and obtaining continuous current flow. These results indicate that comb-shaped planar nanoantennas hold great promise for strong field localization.

Keywords: Optical antennas, split ring resonator, comb-shape, dipole, plasmonics, surface plasmons, localized plasmons, FDTD.

ÖZET

METAMALZEME MİMARİLERİNDEN ESİNLENİLEREK OLUŞTURULAN ORİJİNAL OPTİK ANTENLER

Veli Tayfun Kılıç
Elektrik ve Elektronik Mühendisliği Bölümü Yüksek Lisans
Tez Yöneticisi: Doç. Dr. Hilmi Volkan Demir
Ağustos 2011

Geleneksel optik sistemlerin çözünürlükleri genellikle kırılım limiti ile sınırlıdır. Bu; bir çok yüksek teknoloji uygulamalarında CD, DVD ve mavi ışın diskleri gibi veri depolayıcı aletlerin kapasitelerinin sınırlı olması, dedektörlerdeki sinyal karışmaları, bulanık mikroskopik görüntüler gibi önemli sorunlara neden olur. Bu problemin üstesinden gelebilmek amacıyla günümüze dek bir çok farklı türde optik anten çalışılmıştır. Ancak, bu antenler ya plazmonların ışığı odaklaması ile elde edilebilecek en yüksek dalga şiddetine sahip değiller ya da üretimi zor olan karmaşık 3 boyutlu yapılara veya çok sivri uçlara sahiplerdir. Bu tezde bu probleme karşılık olarak metamalzeme mimarilerinden esinlenilerek oluşturulan E ve tarak şekilleri kullanan yenilikçi düzlemsel optik antenleri çalıştık. Rezonans dalga boyuna kıyasla elektriksel uzunluğu önemli ölçüde küçük olmasına rağmen, bağlı tarak şeklindeki nanoantenlerin boşluklarında odaklanan ışığın şiddetinin tek veya sıra halindeki dipollerin boşluklarında odaklanan ışığın şiddetinden önemli ölçüde fazla olduğunu bulduk. Ayrıca, dipol nanoantendeki odaklanan ışığın şiddetinin aynı boşluğa sahip tek halka rezonatör şeklindeki anten ile uç noktalardan yayılan ışığı azaltmak ve akımın kesintisiz akmasını sağlamak suretiyle iki katından fazlasına çıkarılabileceğini gösterdik. Bu sonuçlar şunu göstermektedir ki tarak şeklindeki düzlemsel nanoantenler ışığın güçlü bir şekilde odaklanması açısından büyük umut vaat etmektedir.

Anahtar Kelimeler: Optik antenler, yarık halka resonatörler, tarak şekli, dipol, plazmonik, yüzey plazmonları, lokalize plazmonlar, FDTD.

Acknowledgements

I would like to express my deepest gratitude to my supervisor Assoc. Prof. Dr. Hilmi Volkan Demir for his guidance and support throughout my M.S. study. He was always helpful and kind to me and I am indebted to him for allowing time whenever I need, even if he was very busy.

I would like to thank Assoc. Prof. Dr. Vakur B. Erturk for his contributions and guidance during my research efforts. He was like my second supervisor. I am indebted to him for giving very useful comments and suggestions during our meetings.

I would also like to thank Prof. Dr. Sencer Koc for reading and commenting on this thesis and for being a member of my thesis committee on this hot August day.

I am very proud to dedicate my thesis to my mother; Necla Kilic, my father; Samet Kilic and my brother; Ismail Kilic for their endless love and endless supports in my whole life. The words are not enough to describe my love and acknowledgement to them.

I would like to thank Tubitak (The Scientific and Technological Research Council of Turkey) for their financial support during my M.S. study.

I would also like to thank Bilkent University EE Department and especially Ihsan Dogramaci the founder of our University (I pray for him) for their contributions and providing such good circumstances during both my undergraduate and graduate study.

I would like to thank former and recent members of Demir Research Group. I would especially like to thank Mustafa Akin Sefunc, Ugur Karatay, Ozan Yerli, Emre Unal, Ozgun Akyuz, Sayim Gokyar, Kivanc Gungor, Hatice Ertugrul, Can Uran, Talha Erdem, Burak Guzelturk, Ahmet Fatih Cihan, Shahab Akhavan, Yusuf Kalestemur, Sedat Nizamoglu, Evren Mutlugun, Emre Sari, Nihan Kosku Perkgoz, Urartu Seker, Pedro L. Hernandez, Onur Akin and Refik Sina Toru for their friendship and collaborations.

Lastly, I cannot pass without mentioning some of my colleagues` names. I am really grateful to my office friends; Ismail Uyanik, Ali Nail Inal, Deniz Kerimoglu, Naci Saldi, Gunes Bayir, Mahmut Yavuzer, Samet Guler for our wonderful late night studies and also to my friends from department; M. Kenan Ozel, Hasan Hamzacebi, Cagri Goken for their support and good friendship.

Table of Contents

List of Figures

List of Tables

To Necla, Samet and İsmail Kılıç

Chapter 1

Introduction

The spatial resolution of a conventional optical system is constrained by the diffraction limit of λ/2NA given the operating optical wavelength λ and the numerical aperture NA of the system [1]. Figure 1.1 illustrates the focusing of light through a lens and shows energy (or intensity) distribution of the focused light.

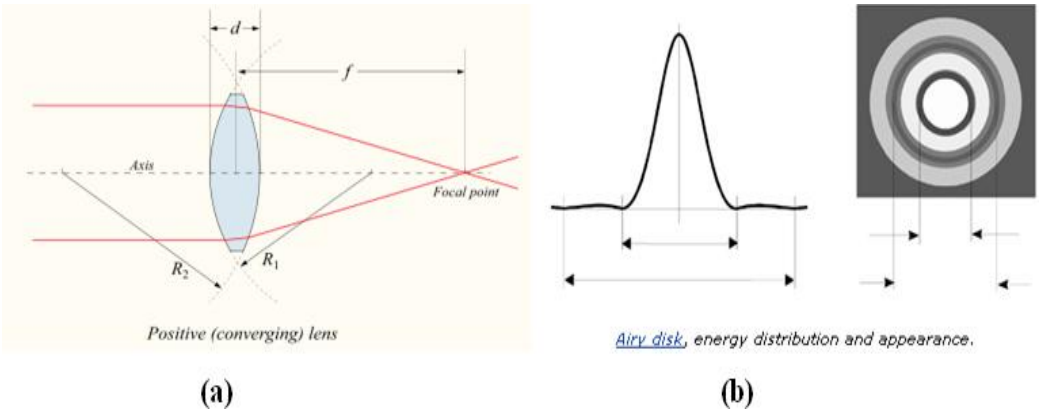

Figure 1.1: (a) Light focusing by a positive converging lens, (b) Energy distribution of focused light (Airy disk) (the images were taken from "http://www.wikipremed.com/" and "http://spie.org/", respectively).

This diffraction limit gives rise to important problems in a number of applications including limited density in data storage, blurred images in microscopy and crosstalk in detectors. Since the diffraction limit is directly proportional to the wavelength of light, to cope with these limits, shorter and shorter wavelengths are being used as the associated technologies improve over time. For instance, to increase capacity of the data storage devices blue wavelength lasers are taking place of old CD lasers today. This development in optical data storage devices is tabulated in Table 1.1. However, despite using shorter and shorter wavelength, the fundamental limit is not overcome in such conventional optical systems.

System	**Year**	**λ [μm]**	**N_0**	**λ/N_0 [μm]**	**Capacity [GB/layer]**	**Diameter [cm]**	**Playing time [min.]**
Video long play	1978	0.633	0.40	1.56	4.5	30	30-60
Laser disc	1983	0.785	0.50	1.57	4.5	30	60
Compact disc	1983	0.785	0.45	1.74	0.65	12	74
DVD	1995	0.650	0.60	1.08	4.7	12	135
HD-DVD	2006	0.405	0.65	0.62	16	12	135
Blu ray	2006	0.405	0.85	0.48	23	12	135

Table 1.1: Physical parameters and storage capacities of optical disc systems in chronological order [2].

However, the production and handling of such blue ray lasers are difficult and costly. In addition, since the diffraction limit is approximately half of the wavelength, light focusing is still constrained within a size of 100 nm`s. Therefore, another technique is required to confine light in a region far beyond the diffraction limit.

Plasmonics offers a solution to meet this requirement. Today it is one of the leading topics in the area of nanophotonics. In terms of physics, we can understand plasmons as collective charge oscillations or free electron gases in metals. Plasmonics investigates how the electromagnetic field can be confined in a region smaller than the wavelength [3,4].

The interaction between radiating electromagnetic fields and conduction electrons on metallic surfaces leads to a field localization. Such plasmonic interactions are of fundamental importance as they allow for confining fields beyond the diffraction limit [4-6]. As a result, today plasmonics is exploited in a wide range of applications including plasmon waveguides, subwavelength apertures for enhanced optical transmission, optical nanoscale antennas, plasmon enhanced Raman scattering, surface-plasmon-polariton-based sensors and plasmonic integrated circuits [4-7].

Although plasmonic applications such as transmission apertures and waveguides help us to confine light in a region smaller than the diffraction limit, the low intensity field may pose a problem. Typically, the resultant electromagnetic excitations die out very quickly as we move farther. Therefore, obtaining higher field intensity is a necessity for plasmonic applications. Plasmonic structures such as optical nanoantennas accomplish this demand by obtaining field spots with very high intensities in a region beyond the diffraction limit [8]. Consequently, they offer a wide variety of important applications including scanning near field optical microscopy, ultra-high density data storage and very sensitive optical detectors.

To this end, different types of optical antennas have been widely investigated [9-27]. Among them dipole and related architectures have been studied most extensively thanks to their simple geometries [10-18]. Their spectral response, tuned by the material parameters (metal, substrate, medium) as well as the geometrical parameters (antenna length, gap size, etc.), have been numerically

computed and experimentally observed. Unfortunately, the field enhancement obtained in these dipole antennas has not reached the largest possible levels that can be achieved using such plasmonic interactions unless very sharp tips, which are difficult to fabricate, are used. Also, nanoantennas of different shapes such as spherical [19-21] and elliptical [20-22] antennas have been reported. For example, three-dimensionally V-shaped structures [23] have been shown to lead to higher enhancement levels. However, while this kind of three-dimensional architectures are capable of providing larger peak field intensity in their localized regions, they are unfavorably harder to fabricate due to their relatively complex construction. Consequently, challenging fabrication of sharp tips or 3D structures hindered the application of large field enhancement in practical architectures. Therefore, there is now a strong need to enable high field enhancement levels while sustaining relatively simple, planar fabrication at the same time.

To address this problem, in this thesis, we study and demonstrate planar optical antennas based on split ring resonator (SRR) architectures. Although various forms and variants of SRRs have been extensively studied especially for metamaterials till date [28], there is no prior report that links SRR antennas evolving from dipole antennas for their capabilities of field localization. This work provides a comparative study for the field localization of such SRR inspired antennas. The design idea of our SRR antenna is to increase the field localization inside the gap region by connecting the end points of the dipole and decreasing the field radiation from there. Our numerical results show that this connection allows the induced current to flow continuously from one gap side to the other over the SRR antenna on resonance. As a result, we observe that large field enhancements are obtained inside the gap region of SRR-shaped antenna. For comparison purposes, we also simulated the single dipole nanoantennas with various lengths but having a constant gap region, which is the same with our SRR antenna. We notice that the field intensity enhancement of dipole nanoantenna can be increased more than two-fold with our SRR architecture. In

addition, our simulation results indicate that the resonance wavelength of SRR-shaped antenna is contingent upon the antenna geometry. It is found that the resonance wavelength changes linearly with the path length of the surface current, which is expected from classical antenna theory.

Furthermore, in this thesis, we study some other antenna architectures such as comb structures. We simulate the antenna architectures starting from a single dipole to comb structure step by step. Although these comb architectures have also been previously studied especially for metamaterials in the radio frequency by our group, again there is no prior study on their usage as optical antennas for field localization. The design and usage idea of these comb structure antennas are similar to the SRR architecture. We aim to increase field localizations inside the gap regions by both decreasing field radiations from the end points and allowing continuous current flow. Our computational results show that the field localizations inside the gap regions of a single or array of dipole nanoantennas can be increased by using a connected comb shaped nanoantenna. More interestingly, the resonance wavelength of the connected comb shaped nanoantenna is red-shifted with respect to the single and array of dipoles, whose lengths are constant and the same with the comb nanoantenna teeth. In addition, our results present that the resonance wavelength of the connected comb shaped nanoantenna increases and additional resonances emerge as we increase the number of teeth.

In this thesis work, we studied all our proposed antenna concepts computationally and presented our numerical results that were obtained by using finite-difference time-domain (FDTD) technique simulations (Lumerical Solutions Inc., Canada). The FDTD method is currently the state-of-the-art to simulate the propagation of waves. It is based on solving Maxwell`s curl equations in time domain on lattice of cells [29-31]. With this method, we are able to use measured and complex dielectric constants of materials in our

simulations. Also, we are able to span large frequency (or wavelength) regimes by simply taking a Fourier transform.

This thesis is organized as follows. In Chapter 1, we briefly introduce optical antennas and describe our motivation. We examine the diffraction limit problem of classical optical systems and discuss plasmonic applications used to overcome this problem. Here, the optical antenna structures reported in the previous literature are also shortly mentioned. At the end of the chapter, we briefly explain our proposed optical antenna structures to enhance field localizations of previously reported antennas. In Chapter 2, we review the fundamentals of plasmonics. We begin with a summary of plasmonics history and continue with the theoretical derivation of surface plasmon polaritons and localized surface plasmons. We also explain the connection of optical antennas with the plasmonics. This chapter is concluded with a brief description of finite-difference time-domain method and a commercial FDTD tool (Lumerical Solutions Inc., Canada). In Chapter 3, we present the field enhancement change and its relationship to the resulting surface currents on different antenna structures. We present the numerical results of variant antenna geometry simulations from single dipole to SRR. In Chapter 4, we parametrically study both SRR shape and dipole antennas. We systematically change some of their geometrical parameters and observe how the resonance behavior alters. Subsequently, we examine our novel antenna architecture of connected comb-shape. We simulate various antenna geometries step by step, including single and array of dipoles and comb-shaped antennas. Also, the effect of teeth number in the connected comb architecture is investigated, too. Finally, in Chapter 5, we conclude our thesis with a summary of all numerical analysis results based on the FDTD technique.

Chapter 2

Fundamentals of Plasmonics

Plasmonics is one of the important topics of the field of nanophotonics. It is mainly about the interactions between the radiated electromagnetic fields and the conduction electrons on metallic surfaces, which enable to confine light in a region far below the diffraction limit. Thus, these metal-field interactions are of crucial importance and explained by the surface plasmon theory [3-7].

In this chapter, we review the fundamentals of plasmonics. We start our discussion with a brief history of plasmons. Subsequently, we examine the two kinds of plasmons: surface plasmon polaritons and localized surface plasmons. In our examination we follow theoretical approach starting from the basic electromagnetics of metals. After that, we proceed with the explanation of how plasmonics is related to optical antennas and how it helps with field localization. At the end, we conclude the chapter with a brief description of finite-difference time-domain method and the FDTD tool (Lumerical Solutions Inc., Canada) that we used in our numerical analysis.

2.1 Brief History

Long before the scientific explanations of electromagnetic theory, the optical properties of metals were used to generate vibrant colors in glass artifacts or to stain window in churches. One of the first and famous applications of surface plasmons in the history is the Lycurgus Cup, which dates back to the Late Roman (4th century AD). The property of this cup is to change its color with holding up to light. The green color of cup changes to red when it is illuminated thoroughly. The contained tiny gold and silver particles provide this fascinating optical property. The Lycurgus Cup is represented in Figure 2.1.

Figure 2.1: The Lycurgus Cup in British museum without direct illumination (left) and under direct illumination (right) (photos were taken from "http://www.britishmuseum.org/explore/highlights/highlight_objects/pe_mla/t/the_lycurgus_cup.aspx").

The first scientific studies on surface plasmons antedated to the beginning of the 20th century. The surface waves on a conductor of finite conductivity were described mathematically by Sommerfeld in 1899 and then Zenneck in 1907. In 1902, the unexpected intensity drop of reflected light from metallic gratings was

reported by R. W. Wood [32]. The explanation of this observation remained unknown till Fano`s work in 1941.

In 1904, Maxwell Garnett explained the reason of vivid colors seen in metal doped glasses and metallic films [33]. In this work, he used the Drude model for metals developed by Paul Drude and the electromagnetic properties of tiny metallic spheres were studied using Lord Rayleigh approach. Around the same years, in 1908 Gustav Mie explained the scattering of light from spherical particles with his theory, which is known as Mie theory today [34].

The research on the topic of metal optics or plasmonics accelerated after the mid of twentieth century. In 1956, David Pines theoretically defined the energy losses in metals based on collective free electron oscillations [35]. Since he called these oscillations as `plasmons` for the first time, his work is also one of the milestones for plasmonics area. Later in 1957, in his study Rufus Ritchie exhibited the existence of plasmon modes near the metal surfaces [36]. This study is also very important because it is the first work that describes surface plasmons theoretically. In addition, eleven years later Ritchie linked his study with the diffraction gratings [37]. In 1968, another milestone in the field of plasmonics was achieved by Erich Kretschmann and Heinz Raether [38]. In their study the excitation of surface plasmons with visible light was shown. Moreover, in 1974 Cunningham and his colleagues used the term `surface plasmon-polariton` for the first time in their study.

In the last two decades, with the developments in nanofabrication process the researchers have mostly focused on the applications of plasmonics. For instance, in 1997 Takahara and his colleagues reported their work on guiding optical beam in a nanometer sized metallic wire [39]. Also in 1998, with his colleagues Thomas Ebessen opened a new perspective by demonstrating extraordinary light transmission through subwavelength holes [40]. In all of these examples, the important point about plasmonics is the ability of confining fields in a region

smaller than the operating wavelength. Today this makes the plasmonics one of the hottest topics where researchers work for various applications spanning from waveguides to optical data storage devices, to sensors, to spectroscopy, to imaging, and so on.

2.2 Surface Plasmon Polaritons

Surface plamon polaritons (SPPs) are the excited electromagnetic fields that propagate along the interface between a dielectric and a conductor (metal) [3]. These waves are confined around the surface because they die out into both the metal and the dielectric. The collective electron oscillation on metal-dielectric interface, which is based on the interaction of the free electrons in metals with the incident electromagnetic field, creates surface plasmon polaritons. Depending on the dielectric functions of different mediums (metal and dielectric), SPPs can be obtained over a wide frequency range spanning from DC to near UV [4].

In plasmonics we mostly deal with nanometer sized structures. However, the deep knowledge of quantum mechanics is not required to understand classical plasmonic interactions (except for the topic of quantum plasmonics) because of the high density of free carriers leading to small spacings of the electron energy levels when compared to thermal excitations of energy k_BT at room temperature [3]. Therefore, the interaction between metals and electromagnetic fields can be comprehended by classical electromagnetic theory.

To this aim, we start to examine surface plasmon polaritons beginning from Maxwell`s equations.

$$\nabla \cdot \mathbf{D}(\boldsymbol{r},t) = \rho_{ext}(\boldsymbol{r},t) \tag{2.1}$$

$$\nabla \cdot \mathbf{B}(\boldsymbol{r},t) = 0 \tag{2.2}$$

$$\nabla \times \mathbf{E}(\boldsymbol{r},t) = -\frac{\delta \mathbf{B}(\boldsymbol{r},t)}{\delta t} \tag{2.3}$$

$$\nabla \times \mathbf{H}(\boldsymbol{r},t) = \mathbf{J}_{ext}(\boldsymbol{r},t) + \frac{\delta \mathbf{D}(\boldsymbol{r},t)}{\delta t} \tag{2.4}$$

In these Maxwell`s equations $\mathbf{E}(\boldsymbol{r},t)$ is the electric field intensity (V/m), $\mathbf{H}(\boldsymbol{r},t)$ is the magnetic field intensity (A/m), $\mathbf{D}(\boldsymbol{r},t)$ is the electric displacement density (C/m^2) and $\mathbf{B}(\boldsymbol{r},t)$ is the magnetic flux density (Tesla or Wb/m^2). Also ρ_{ext} and $\mathbf{J}_{ext}$ are the sources that represent external charge density (C/m^3) and current density (A/m^2), respectively.

In linear, isotropic and nonmagnetic media the vectorial quantities above are linked with constitutive relations.

$$\mathbf{D}(\boldsymbol{r},t) = \varepsilon \mathbf{E}(\boldsymbol{r},t) \tag{2.5}$$

$$\mathbf{B}(\boldsymbol{r},t) = \mu \mathbf{H}(\boldsymbol{r},t) \tag{2.6}$$

All these equations are in time domain. However, solving for these equations is difficult due to derivatives. For that reason, we will continue with calculations in frequency (phasor) domain.

For simplicity, we assume that the sources ρ_{ext} and $\mathbf{J}_{ext}$ vary sinusoidally with time at angular frequency ω. Thus, in linear medium, the resulting fields also vary sinusoidally with the same angular frequency ω and are called time-harmonic fields.

With $e^{-i\omega t}$ time convention,

$$\mathbf{E}(\boldsymbol{r},t) = Re\left\{\mathbf{E}(\boldsymbol{r})\ e^{-i\omega t}\right\} \tag{2.7}$$

and similar representation holds for other quantities.

From (2.7) we obtain $\frac{\delta}{\delta t} = -i\omega$ harmonic time dependence in phasor domain. Therefore, Maxwell equations turn into the following in the phasor domain.

$$\nabla \bullet \mathbf{D}(\boldsymbol{r}) = \rho_{ext}(\boldsymbol{r}) \tag{2.8}$$

$$\nabla \bullet \mathbf{B}(\boldsymbol{r}) = 0 \tag{2.9}$$

$$\nabla \times \mathbf{E}(\boldsymbol{r}) = i\omega \mathbf{B}(\boldsymbol{r}) \tag{2.10}$$

$$\nabla \times \mathbf{H}(\boldsymbol{r}) = \mathbf{J}_{ext}(\boldsymbol{r}) - i\omega \mathbf{D}(\boldsymbol{r}) \tag{2.11}$$

$$\mathbf{D}(\boldsymbol{r}) = \varepsilon \mathbf{E}(\boldsymbol{r}) \tag{2.12}$$

$$\mathbf{B}(\boldsymbol{r}) = \mu \mathbf{H}(\boldsymbol{r}) \tag{2.13}$$

In plasmonic systems generally there is no external charge or current sources because plasmonics are generated with the light excitation. Thus, taking $\rho_{ext} = 0$ and $\mathbf{J}_{ext} = 0$ make calculations easier. From now on we will also consider in our calculations that there are no source terms in our equations.

We plug (2.13) into (2.10) and write ∇ operator in the cartesian coordinates for simplicity, which yields:

$$\left(\hat{\boldsymbol{a}}_x \frac{\delta}{\delta x} + \hat{\boldsymbol{a}}_y \frac{\delta}{\delta y} + \hat{\boldsymbol{a}}_z \frac{\delta}{\delta z}\right) \times \left(\hat{\boldsymbol{a}}_x \mathrm{E}_x + \hat{\boldsymbol{a}}_y \mathrm{E}_y + \hat{\boldsymbol{a}}_z \mathrm{E}_z\right) = i\omega\mu\left(\hat{\boldsymbol{a}}_x \mathrm{H}_x + \hat{\boldsymbol{a}}_y \mathrm{H}_y + \hat{\boldsymbol{a}}_z \mathrm{H}_z\right) \tag{2.14}$$

The fields in both sides in *x*, *y* and *z* directions should be equal as given below.

$$\frac{\delta \mathrm{E}_z}{\delta y} - \frac{\delta \mathrm{E}_y}{\delta z} = i\omega\mu \mathrm{H}_x \tag{2.15}$$

$$\frac{\delta \mathrm{E}_x}{\delta z} - \frac{\delta \mathrm{E}_z}{\delta x} = i\omega\mu \mathrm{H}_y \tag{2.16}$$

$$\frac{\delta \mathrm{E}_y}{\delta x} - \frac{\delta \mathrm{E}_x}{\delta y} = i\omega\mu \mathrm{H}_z \tag{2.17}$$

Similarly, if we put (2.12) into (2.11) and write ∇ operator in cartesian coordinates, we obtain:

$$\left(\hat{\boldsymbol{a}}_x \frac{\delta}{\delta x} + \hat{\boldsymbol{a}}_y \frac{\delta}{\delta y} + \hat{\boldsymbol{a}}_z \frac{\delta}{\delta z}\right) \times \left(\hat{\boldsymbol{a}}_x \mathrm{H}_x + \hat{\boldsymbol{a}}_y \mathrm{H}_y + \hat{\boldsymbol{a}}_z \mathrm{H}_z\right) = -i\omega\varepsilon\left(\hat{\boldsymbol{a}}_x \mathrm{E}_x + \hat{\boldsymbol{a}}_y \mathrm{E}_y + \hat{\boldsymbol{a}}_z \mathrm{E}_z\right) \tag{2.18}$$

Again the fields in both sides in *x*, *y* and *z* directions should be equal.

$$\frac{\delta \mathrm{H}_z}{\delta y} - \frac{\delta \mathrm{H}_y}{\delta z} = -i\omega\varepsilon \mathrm{E}_x \tag{2.19}$$

$$\frac{\delta \mathrm{H}_x}{\delta z} - \frac{\delta \mathrm{H}_z}{\delta x} = -i\omega\varepsilon \mathrm{E}_y \tag{2.20}$$

$$\frac{\delta \mathrm{H}_y}{\delta x} - \frac{\delta \mathrm{H}_x}{\delta y} = -i\omega\varepsilon \mathrm{E}_z \tag{2.21}$$

A simple metal-dielectric boundary is sketched in Figure 2.2. Since the selected coordinate axes should not affect the results, in the figure the propagation direction of surface plasmon ploaritons is chosen in *x*-direction.

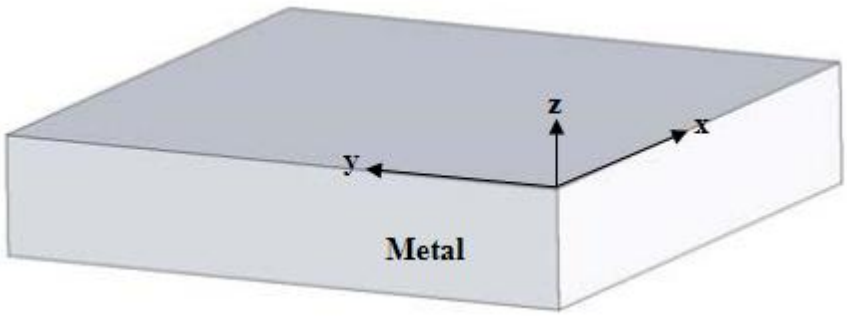

Figure 2.2: Simple metal-dielectric boundary.

For simplicity if we assume that the metal is infinitely long in $\pm$ *y* directions, then the wave`s amplitude should not change in *y*-direction. Also since the wave is on the same surface during its propagation in *x*-direction, only its phase changes with position in *x*-direction. Therefore, the propagating waves in *x*-direction can be described as such:

$$\mathbf{E}(x,y,z)=\mathbf{E}(z)e^{i\beta x} \tag{2.22}$$

$$\mathbf{H}(x,y,z)=\mathbf{H}(z)e^{i\beta x} \tag{2.23}$$

where $\beta=k_x$ is the propagation constant that corresponds to the wave vector component in the direction of propagation.

From these equations it is obvious that $\frac{\delta}{\delta x}=i\beta$ and $\frac{\delta}{\delta y}=0$. These equalities simplify the equations of (2.15)-(2.17) and (2.19)-(2.21) as follows.

$$\frac{\delta \mathrm{E}_y}{\delta z}=-i\omega\mu \mathrm{H}_x \tag{2.24}$$

$$\frac{\delta \mathrm{E}_x}{\delta z}-i\beta \mathrm{E}_z=i\omega\mu \mathrm{H}_y \tag{2.25}$$

$$i\beta \mathrm{E}_y=i\omega\mu \mathrm{H}_z \tag{2.26}$$

$$\frac{\delta \mathrm{H}_y}{\delta z}=i\omega\varepsilon \mathrm{E}_x \tag{2.27}$$

$$\frac{\delta \mathrm{H}_x}{\delta z}-i\beta \mathrm{H}_z=-i\omega\varepsilon \mathrm{E}_y \tag{2.28}$$

$$i\beta \mathrm{H}_y=-i\omega\varepsilon \mathrm{E}_z \tag{2.29}$$

From this set of equations, it is seen that our simple metal-dielectric system supports two sets of solutions, one of which is TE (transverse-electric) while the other is TM (transverse magnetic). For TEM waves all E_x, E_y, E_z, H_x, H_y and H_z fields vanish so system does not allow TEM waves.

First consider TE (s) waves. For TE case, $E_x = E_z = H_y = 0$. Thus, the six equations of (2.24)-(2.29) reduce to:

$$\mathrm{H}_x=i\frac{1}{\omega\mu}\frac{\delta \mathrm{E}_y}{\delta z} \tag{2.30}$$

$$\mathrm{H}_z=\frac{\beta}{\omega\mu}\mathrm{E}_y \tag{2.31}$$

If we substitute these two equalities into (2.28), we obtain TE wave equation.

$$\frac{\delta^2 \mathrm{E}_y}{\delta z^2} + \left(k^2 - \beta^2\right)\mathrm{E}_y = 0 \tag{2.32}$$

where $k = \omega\sqrt{\mu\varepsilon}$ is the propagation constant. Since our structure interfaces two media of metal (z<0) and dielectric (z>0), we have a different solution of the wave equation for each medium. The important point is that the boundary conditions should be satisfied in each case.

Next we look at the wave solution that is confined to the interface, which implies a decaying wave inside both the metal and the dielectric. The solution of TE wave equation, which satisfies all these requirements, is represented step by step below.

In the dielectric (z>0):

$$\mathrm{E}_y(z) = A_1 e^{i\beta x} e^{-k_{zd} z} \tag{2.33}$$

Substituting it into (2.30) and (2.31) yields:

$$\mathrm{H}_x(z) = -i\frac{k_{zd}}{\omega\mu_0} A_1 e^{i\beta x} e^{-k_{zd} z} \tag{2.34}$$

$$\mathrm{H}_z(z) = \frac{\beta}{\omega\mu_0} A_1 e^{i\beta x} e^{-k_{zd} z} \tag{2.35}$$

In the metal (z<0):

$$\mathrm{E}_y(z) = A_2 e^{i\beta x} e^{k_{zm} z} \tag{2.36}$$

Substituting it into (2.30) and (2.31) yields:

$$\mathrm{H}_x(z) = i\frac{k_{zm}}{\omega\mu_0} A_2 e^{i\beta x} e^{k_{zm} z} \tag{2.37}$$

$$\mathrm{H}_z(z) = \frac{\beta}{\omega\mu_0} A_2 e^{i\beta x} e^{k_{zm} z} \tag{2.38}$$

From the boundary conditions, the tangential electric field and magnetic field (E_y and H_x) should be continuous at the interface (z=0) in our system.

From (2.33) and (2.36):

$$A_1 e^{i\beta x} e^{-k_{zd} z}\Big|_{z=0} = A_2 e^{i\beta x} e^{k_{zm} z}\Big|_{z=0} \tag{2.39}$$

$$A_1 = A_2 \tag{2.40}$$

From (2.34) and (2.37):

$$-i\frac{k_{zd}}{\omega\mu_0} A_1 e^{i\beta x} e^{-k_{zd} z}\Big|_{z=0} = i\frac{k_{zm}}{\omega\mu_0} A_2 e^{i\beta x} e^{k_{zm} z}\Big|_{z=0} \tag{2.41}$$

$$-k_{zd} A_1 = k_{zm} A_2 \tag{2.42}$$

Placing (2.40) into (2.42) will give us:

$$-k_{zd} = k_{zm} \tag{2.43}$$

For fields being evanescent and thus decaying into both metal and dielectric mediums, the real parts of k_{zd} and k_{zm} should be positive. That requirement contradicts with (2.43). Therefore, for TE mode there is no surface mode that exist [3].

Next consider TM (p) waves. For TM case, $E_y = H_x = H_z = 0$. Thus, the six equations of (2.24)-(2.29) boil down to:

$$E_x = -i\frac{1}{\omega\varepsilon}\frac{\delta H_y}{\delta z} \tag{2.44}$$

$$E_Z = -\frac{\beta}{\omega\varepsilon} H_y \tag{2.45}$$

If we combine these two equalities into (2.25), it turns into TM wave equation:

$$\frac{\delta^2 H_y}{\delta z^2} + \left(k^2 - \beta^2\right) H_y = 0 \tag{2.46}$$

where $k = \omega\sqrt{\mu\varepsilon}$ is the propagation constant. Again, since our structure contains metal (z<0) and dielectric (z>0), we obtain different solutions of the wave equation for different mediums.

The magnetic field as the solution of the wave equation is given in (2.47) and (2.50). These demonstrate that the field expectedly decays in $\pm z$-directions, which means that the field propagates only along the surface. Further calculations of these surface plasmon polariton waves are derived below.

In dielectric (z>0):

$$\mathrm{H}_y(z) = A_1 e^{i\beta x} e^{-k_{zd} z} \tag{2.47}$$

Putting it into (2.44) and (2.45) gives:

$$\mathrm{E}_x(z) = i\frac{k_{zd}}{\omega\varepsilon_0\varepsilon_d} A_1 e^{i\beta x} e^{-k_{zd} z} \tag{2.48}$$

$$\mathrm{E}_z(z) = -\frac{\beta}{\omega\varepsilon_0\varepsilon_d} A_1 e^{i\beta x} e^{-k_{zd} z} \tag{2.49}$$

In metal (z<0):

$$\mathrm{H}_y(z) = A_2 e^{i\beta x} e^{k_{zm} z} \tag{2.50}$$

Plugging it into (2.44) and (2.45) yields:

$$\mathrm{E}_x(z) = -i\frac{k_{zm}}{\omega\varepsilon_0\varepsilon_m} A_2 e^{i\beta x} e^{k_{zm} z} \tag{2.51}$$

$$\mathrm{E}_z(z) = -\frac{\beta}{\omega\varepsilon_0\varepsilon_m} A_2 e^{i\beta x} e^{k_{zm} z} \tag{2.52}$$

Again from the boundary conditions, the tangential electric field and magnetic field (E_x and H_y) should be continuous at the interface (z=0) in our system.
From (2.47) and (2.50):

$$A_1 e^{i\beta x} e^{-k_{zd} z}\Big|_{z=0} = A_2 e^{i\beta x} e^{k_{zm} z}\Big|_{z=0} \tag{2.53}$$

$$A_1 = A_2 \tag{2.54}$$

From (2.48) and (2.51):

$$i\frac{k_{zd}}{\omega\varepsilon_0\varepsilon_d} A_1 e^{i\beta x} e^{-k_{zd} z}\Big|_{z=0} = -i\frac{k_{zm}}{\omega\varepsilon_0\varepsilon_m} A_2 e^{i\beta x} e^{k_{zm} z}\Big|_{z=0} \tag{2.55}$$

$$-\frac{k_{zd}}{\varepsilon_d} A_1 = \frac{k_{zm}}{\varepsilon_m} A_2 \tag{2.56}$$

Finally, substituting (2.54) into (2.56) gives us what we would like to find:

$$-\frac{k_{zd}}{\varepsilon_d} = \frac{k_{zm}}{\varepsilon_m} \tag{2.57}$$

Since k_{zd} and k_{zm} should be positive for fields being confined at the surface, ε_d and ε_m should have opposite signs according to (2.57). In other words, the surface plasmon polaritons can exist only at the interface between materials with oppositely signed dielectric permittivities, i.e., between a conductor and an insulator [3].

Resultantly, it is proved that only TM mode surface waves can exist on the surface between a dielectric and a metal. These allowed surface modes for TM polarization look like as sketched in Figure 2.3.

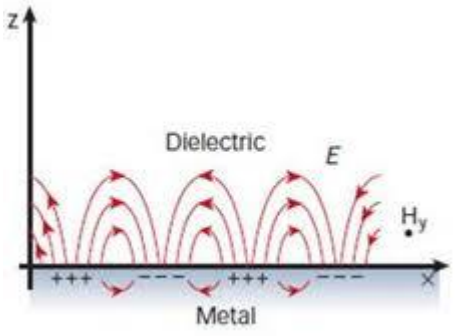

Figure 2.3: Surface plasmon polaritons for TM modes (captured from "http://ralukaszew.people.wm.edu/new_projects.htm").

Now we know the medium and polarization conditions for the existence of surface plasmon polaritons. However, to develop a deeper understanding of the polaritons we should further take a closer look at the dispersion relation.

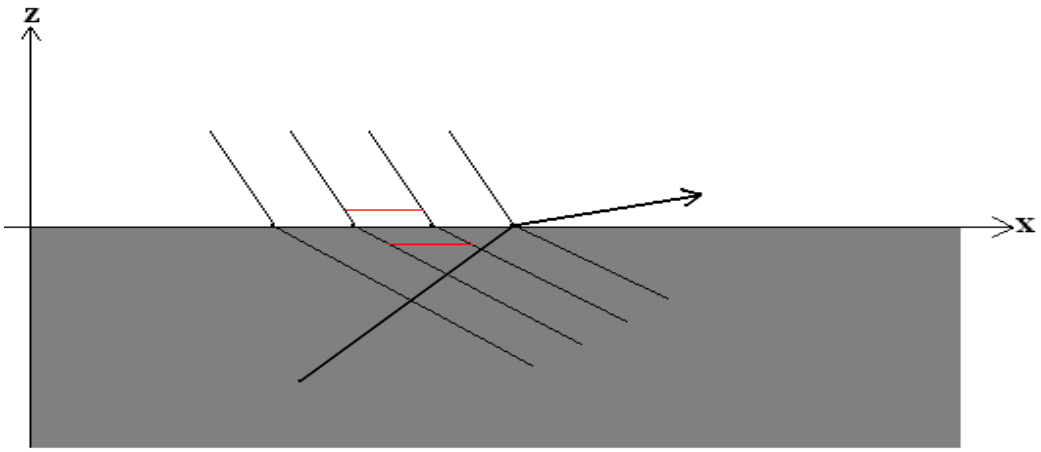

Figure 2.4: Refraction of light at a boundary.

The refraction of light at a boundary and corresponding wavefronts are illustrated in Figure 2.4. In these phenomena, the wavefront components at the boundary (represented with red lines) should be continuous. In our system of dielectric and metal interface, for plasmon polaritons, the same situation holds true. The wavefront components at the boundary should be continuous for the evanescent waves that decay towards both metal and dielectric. Therefore, we have (2.58) for our metal-dielectric boundary, which serves as our starting point for a deeper analysis.

$$\lambda_{xm} = \lambda_{xd} \rightarrow k_{xm} = k_{xd} \tag{2.58}$$

Since we assume there is no propagation in *y*-direction:

$$k_{xm}{}^2 + k_{zm}{}^2 = \left(\frac{\omega}{c} \sqrt{\varepsilon_m} \right)^2 \tag{2.59}$$

$$k_{xd}{}^2 + k_{zd}{}^2 = \left(\frac{\omega}{c} \sqrt{\varepsilon_d} \right)^2 \tag{2.60}$$

So if we combine (2.59) and (2.60) into (2.58), we obtain:

$$k_{sp} = k_{xm} = k_{xd} = \left(\sqrt{\varepsilon_m \frac{\omega^2}{c^2} - k_{zm}{}^2} \right) = \left(\sqrt{\varepsilon_d \frac{\omega^2}{c^2} - k_{zd}{}^2} \right) \tag{2.61}$$

$$\varepsilon_m \frac{\omega^2}{c^2} - {k_{zm}}^2 = \varepsilon_d \frac{\omega^2}{c^2} - {k_{zd}}^2 \tag{2.62}$$

Placing (2.57) into (2.62) yields:

$$\varepsilon_m \frac{\omega^2}{c^2} - {k_{zm}}^2 = \varepsilon_d \frac{\omega^2}{c^2} - {k_{zm}}^2 \frac{{\varepsilon_d}^2}{{\varepsilon_m}^2} \tag{2.63}$$

$$\left(\varepsilon_m - \varepsilon_d\right)\frac{\omega^2}{c^2} = {k_{zm}}^2 \left(1 - \frac{{\varepsilon_d}^2}{{\varepsilon_m}^2}\right) \tag{2.64}$$

$${k_{zm}}^2 = \left(\frac{{\varepsilon_m}^2}{\varepsilon_m + \varepsilon_d}\right)\frac{\omega^2}{c^2} \tag{2.65}$$

Finally let's put (2.65) into (2.61):

$$k_{sp} = k_x = \sqrt{\varepsilon_m \frac{\omega^2}{c^2} - \frac{{\varepsilon_m}^2}{\varepsilon_m + \varepsilon_d}\frac{\omega^2}{c^2}} = \sqrt{\frac{\varepsilon_m \varepsilon_d}{\varepsilon_m + \varepsilon_d}\frac{\omega^2}{c^2}} \tag{2.66}$$

to obtain

$$k_{sp} = k_x = \frac{\omega}{c}\sqrt{\frac{\varepsilon_m \varepsilon_d}{\varepsilon_m + \varepsilon_d}} \tag{2.67}$$

This equation given in (2.67) is the dispersion relation of surface plasmon polaritons that propagate along the interface between a metal and a dielectric. Here, k_{sp} is the wave number of the surface wave, ω is the angular frequency, c is the speed of light in vacuum, and ε_m and ε_d are the metal and dielectric medium permittivities, respectively. The dielectric constants of dielectric materials are positive and do not change a lot with frequency. However, the dielectric constants of metals can be either positive or negative depending on the frequency. These dielectric constants are plotted in Figure 2.5.

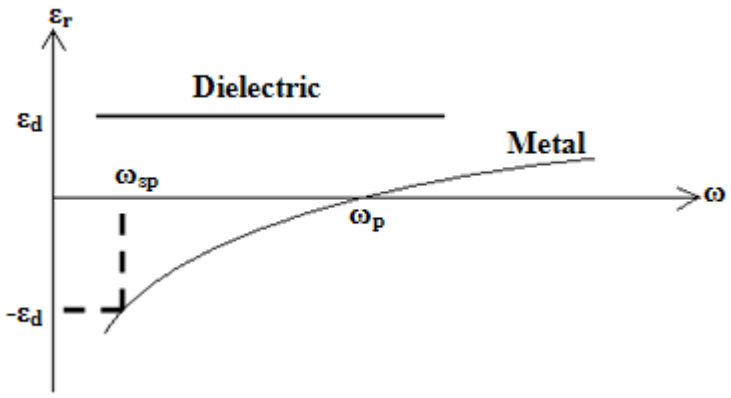

Figure 2.5: General relative permittivity vs. angular frequency for metal and dielectric.

In Figure 2.5, it is defined that $\omega=\omega_{sp}$ when $\varepsilon_m = -\varepsilon_d$, because in dispersion relation (2.67), if $\varepsilon_m = -\varepsilon_d$, then $k_{sp} \to \infty$. Also as seen from Figure 2.5 at low frequencies, the metal dielectric constant increases in magnitude in negative direction. Therefore, at low ω:

$$k_{sp} = k_x = \frac{\omega}{c} \lim_{\varepsilon_m \to -\infty} \sqrt{\frac{\varepsilon_m \varepsilon_d}{\varepsilon_m + \varepsilon_d}} = \frac{\omega}{c} \sqrt{\varepsilon_d} \qquad (2.67)$$

The light line is defined to indicate the boundary on the dispersion relation for waves that propagate inside the dielectric. The dispersion relation of surface plasmon polaritons (2.67) is presented along with the light line in Figure 2.6.

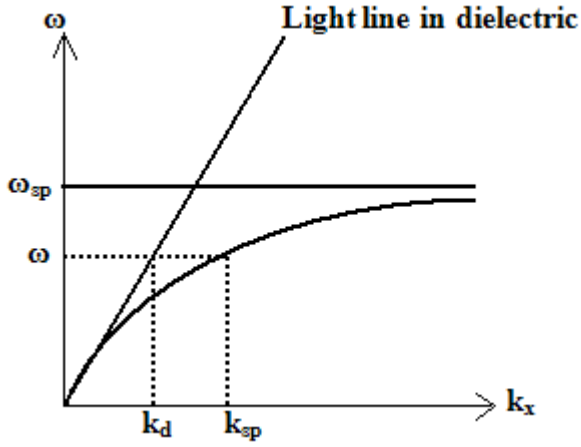

Figure 2.6: Dispersion relations of SPPs.

As can be seen from Figure 2.6, the allowed solutions of surface plasmon polaritons lie below the light line. It means that supported polariton modes at the interface have greater momentum (k_{sp}) than the propagating modes inside the dielectric (k_d) with the same frequency. This momentum mismatch is the reason why the propagating modes inside the dielectric (usually air) cannot be directly coupled into the SPP modes. To overcome this momentum mismatch and excite SPPs modes below the light line, we need a trick.

The first possible trick is the excitation of SPPs with illumination from a high index medium (with dielectric prism). Kretschmann geometry is the most commonly known structure in this technique. To excite SPP modes at the interface between metal and dielectric (such as air), light is sent from a third medium with high index (such as glass) towards the metal. Passing through the glass, the incident light totally internally reflects from the glass-metal interface and creates evanescent fields on the surface. If metal is not too thick, these fields couple into the SPP modes on the metal-air interface.

Other two common tricks are the excitation of SPPs with grating structures and excitation of SPPs with dots. In grating structures, due to periodicity of gratings, the momentum of surface polaritons will shift periodically. As a result, for correct grating geometries, SPP modes on the surface can be excited with light illumination. Similarly, dot will shift the momentum of surface polaritons but, in this case different than the gratings, not periodically. This shift in the momentum is related to spatial fourier transform of the dot and provides the required momentum to make up for the mismatch.

2.3 Localized Surface Plasmons

In the previous section we have seen that surface plasmon polaritons are the excited surface waves occurring at the metal-dielectric interface. These polaritons are propagating, dispersive electromagnetic waves and can only be

excited by TM polarized fields under the momentum matching condition. On the other hand, localized surface plasmons are non-propagating, making the second type of surface plasmons. Localized surface plasmons are non-propagating excitations based on the interaction of the conduction electrons on metal particles with the incident electromagnetic field that penetrates into the metal. More deeply, the electrons in the metal particles are driven by the incident electromagnetic field but a restoring force arises due to curved surfaces. As a result, electrons start to oscillate collectively on resonance. This resonance phenomenon is named localized surface plasmon. In contrast to surface plasmon polaritons, localized surface plasmons can be excited by direct light illumination. It means that the localized surface plasmons can be excited with light having either TE or TM polarizations [3].

The analytical description of localized surface plasmons is a part of the Mie`s theory. With Mie`s theory, the absorption and scattering of light from a metal sphere is explained theoretically [41-43]. In this absorption and scattering analysis different approximations are used such as quasistatic and dipole approximations [41, 44, 45].

Localized surface plasmons are important because it is the one that occurs in optical antenna structures and helps the field localization and intensity enhancements in these structures. We will examine localized surface plasmons in optical antennas in detail in next section.

2.4 Plasmonics in Optical Antennas

Recent studies in plasmonic applications show that with optical antennas light can be concentrated in a localized region beyond the diffraction limit with an highly increased intensity level [8]. In literature various types of optical antennas have been investigated till date [9-27]. Because of their easy geometries, dipole and related shapes have been mostly studied [10-18].

Therefore, in this section to understand how plasmonics is related to optical antennas and how it helps field localization, we will study simple dipole geometry as shown in Figure 2.7.

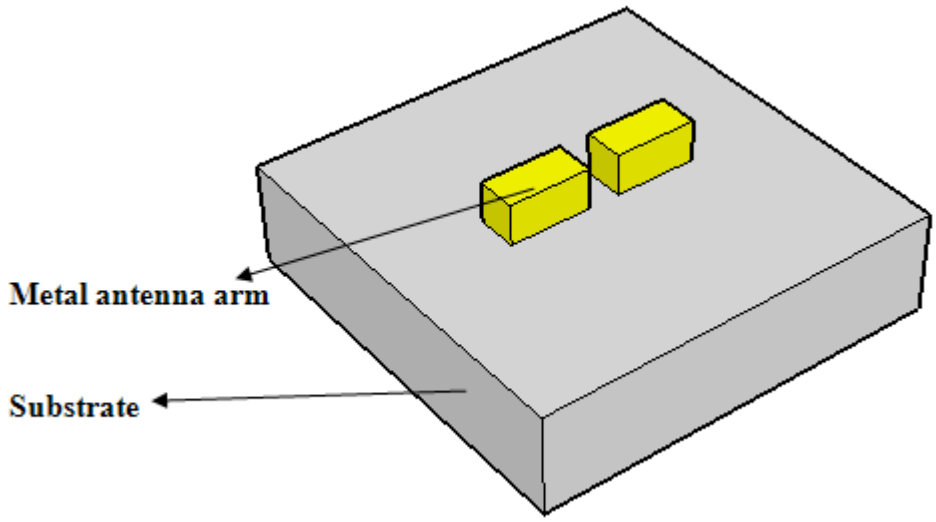

Figure 2.7: Simple dipole antenna geometry.

In optical antennas the field enhancement is usually examined in terms of transmission. The metal antenna arms are illuminated directly or from the substrate side with an incident wave. As a result of interaction between this incident wave and conduction electrons on metals, localized surface plasmons are generated. In other words, incident electromagnetic field interacts with the free metal electrons and causes collective charge oscillations on the metal. These free charges accumulate mostly at the corners, resulting in `lightning rod effect` [13, 21]. Due to discontinuities at the corners, these oscillating charges result intense field radiations from there. This is the idea behind the field localization and enhancement of optical antennas. These localized surface plasmons and resultant field localization and radiations can be observed in one of our simulation outputs presented in Figure 2.8.

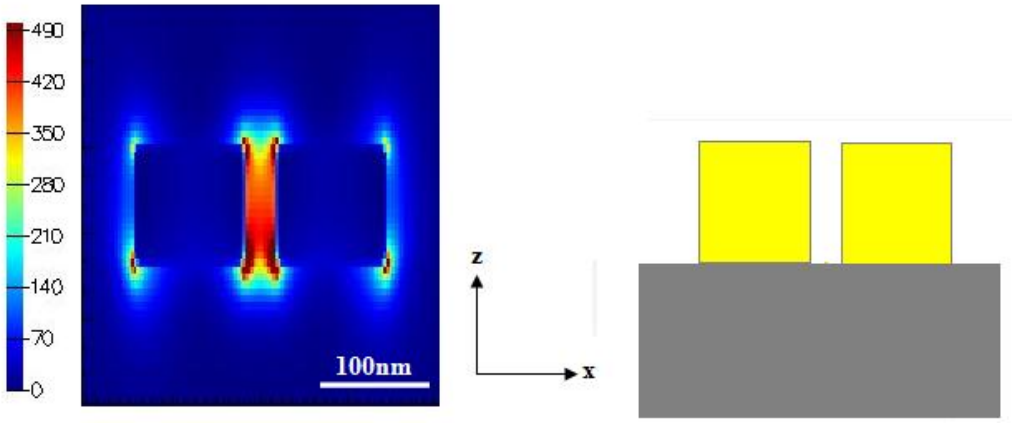

Figure 2.8: Simulated localized surface plasmons and field radiations (left), along with the cross-section of dipole antenna (right).

In this simulation we illuminate antenna from substrate side with a plane wave polarized along the *x*-direction. It is obvious in the result that large field enhancement of two orders of magnitude is achieved as a result of localized surface plasmon excitations. On the other hand, the same enhancement levels cannot be reached under the illumination of plane wave polarized along the *y*-direction. We can understand this observation by looking into the field-charge (plasmon) relation. When the incident field is polarized along the dipole axis, then with the effect of incident light free electrons move opposite to that field, say towards the right (+*x* here) direction. In this case, right faces of antenna arms charge negatively and left faces of antenna arms charge positively. As a result, on one side of the gap positive charges and on the other side of the gap negative charges accumulate. These opposite charges interact with each other and produce large field enhancement inside the gap area. However, if the incident field polarization is perpendicular to the dipole axis, there is no such opposite charge accumulation and no such large field enhancement in the gap region. Thus, all these explanations point out that the polarization of incident light is important for the magnitude of the localized field, while the localized surface plasmons arise in both polarizations.

2.5 Finite-Difference Time-Domain (FDTD) Method and Simulation Tool Lumerical

The finite-difference time-domain (FDTD) method is one of the most efficient and powerful techniques to solve three-dimensional electromagnetic problems. It is based on the solution of time-dependent Maxwell`s equations (2.1)-(2.4) on discretized spatial grids. In this method; first, electric field vector components are solved on a discretized spatial grid at a given instant time. Then, magnetic field vector components are solved on the same grid at next instant time. These calculations continue repeatedly until the desired transient condition is held. This method is first introduced by Kane S. Yee in 1966 [46] and then further developed by Taflove in the 1970s [47]. Today, with the advancements in computer systems, FDTD became one of the most powerful tools in engineering simulations for the modeling of wave propagation, scattering, diffraction, reflection and so on.

Although FDTD method is based on the calculations in the time domain, the frequency domain response can easily be obtained by taking the Fourier transform of the time domain results. This allows us to calculate complex electric and magnetic field components, complex power flow quantity (Poynting`s vector), etc. in the frequency domain.

In our numerical simulations, we used a commercial FDTD software tool (Lumerical Solutions Inc., Vancouver, Canada). Lumerical is generally used for high frequency and micro- or nano-sized simulations. It is an easy tool to use because, in addition to script files, Lumerical provides a user interface, shown in Figure 2.9.

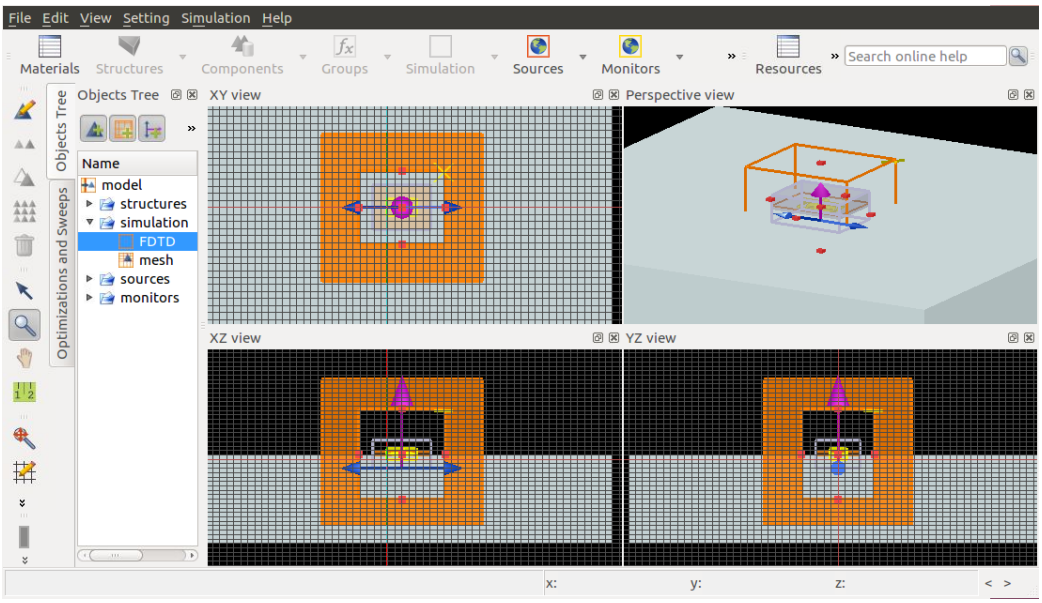

Figure 2.9: A screenshot taken from our simulations showing Lumerical software user interface.

Our simulation process in Lumerical can be summarized into four parts. These include generating a structure and assigning corresponding material types (or index values) to the parts of this structure, setting source region, type and properties (spanning wavelength, polarity etc.), adjusting appropriate simulation region and meshing, and placing data monitors and calculation of required field quantities.

In Lumerical, constructing objects in any geometry in 2D or 3D is possible by simply using the user interface or writing a proper script file code. The optical properties of these created objects can be assigned directly by entering intended dielectric parameters and related frequencies. In addition, in Lumerical`s database, material types with experimental refractive index (n, k) data published in literature such as those by Palik or Johnson and Christy are available. The capability to assign frequency dependent optical parameter is beneficial for users in wide spectrum range simulations.

Another feature of Lumerical is that it supports various source types including dipole, Gaussian, plane wave and total field scattered field (TFSF). For appropriate illumination source users select one of these types. Also, the other source properties (wavelength, polarization, incident angle, illumination area, etc.) can be adjusted in Lumerical by users. These features provide very wide flexibility in terms of illumination.

The simulation region is an important consideration in FDTD simulations. Since computational power is not sufficient to mesh large areas (or volumes), in real life applications, we need to truncate simulation regions and make FDTD calculations in these finite (bounded) simulation regions. Depending on the simulations, Lumerical provides different types of boundary conditions such as perfectly matched layer boundary condition (PML), periodic boundary condition and Bloch boundary condition. The aim of using PML boundary condition is to absorb outgoing waves maximally coming from computational domain and reflect them minimally back into the computational domain. On the other hand, Bloch and periodic boundary conditions are used when the simulated structures extend to infinity periodically, and the simulated field repeats with and without phase shift between each period, respectively. Moreover, the mesh size is another important parameter for simulations. Smaller mesh size yields more correct results, but it requires higher computational power. Therefore, there is a trade-off between meshing accuracy and required memory. In Lumerical, to help with this issue uniform and non-uniform meshing are allowed. In our simulations we used both of them and made our simulations as accurate as possible.

Finally, after constructing and adjusting all above simulation structures and parameters, the required data are collected in an intended area via data monitors. Also, in Lumerical, these collected data such as field intensities are used in other calculations and derivations including power flow and averaged field intensity enhancement with script file codes.

Chapter 3

Field Enhancement and Surface Current Relations

As we mentioned earlier in the introduction chapter, there is a strong need to enable higher field enhancement levels in optical antennas while sustaining relatively simple, planar fabrication at the same time. To this end, we design and study optical antenna made of a split ring resonator architecture. We aim to increase field localization inside the gap region by connecting end points of a starting dipole into the final ring resonator. We expect that this simple connection decreases the field radiations from end points of the dipole and allows continuous current flow over the antenna.

In this chapter, we investigate the field intensity enhancement change and its relationship with the resulting surface currents for various antenna geometries. We simulate different architectures evolving from a single dipole to a split ring resonator including double dipoles and C-shape.

3.1 Method and Geometry

In our analysis, we focus on the field intensity enhancement inside the gap regions of antennas over a wide wavelength spectrum from 400 to 7000 nm. Our simulations are performed over such a wide range of spectrum because we expect to see red shift of resonance in the ring shaped antenna with respect to the single dipole antenna. Also, to describe their relation with the resonance, we examine the induced surface currents in metal on resonance. Since surface currents are related to tangential magnetic fields, in our analysis we first look at the emerged tangential fields on each surface and then evaluate resulting surface currents.

In our computations we calculate the field intensity enhancement with respect to the incident field intensity averaged over the gap volume, which is given by

$$field\ enhancement = \frac{1}{V}\int_V \left|\frac{E(x,y,z)}{E_{inc}}\right|^2 dV \qquad (3.1)$$

where V is the gap volume, and $E(x, y, z)$ and E_{inc} are the field inside the gap region and the incident (source) field, respectively.

We illuminate the antennas through the substrate with a plane wave (TFSF source) polarized along the *x*-direction (the same direction with dipole orientation). A part of the computational domain that includes the antenna and some additional volume surrounding the antenna (extended by 300 nm, 300 nm and 25 nm from the antenna in the *x*-, *y*- and *z*-directions, respectively) is meshed uniformly with a mesh size of 2.5 nm. The rest of the computational domain is meshed using a coarser mesh size. The computational domain is truncated with perfectly matched layers. We meshed volumes that include antennas uniformly for fair comparisons. Although a further finer mesh will

result in more accurate results, 2.5 nm is a good choice for the mesh step to study and demonstrate proof-of-concept for our ideas.

In our simulations presented in this chapter, we use Au [48] as the metal and SiO_2 [49] as the dielectric platform (substrate) on which antennas are patterned because silica is commonly available, cheap and transparent over a wide spectrum including the visible and near infrared regions. In addition, the geometrical parameters of the antennas are kept constant to avoid an unfair comparison due to the lightning rod effect [13, 21]. The gap size (*g*), the metal width (*w*) and the metal thickness (*t*) are set to be 30, 40 and 40 nm, respectively, since patterns with these features can be realized using currently available nanofabrication processes. We also set arm lengths of dipole constant at 100 nm (leading to a dipole length of *l*=230 nm). Since we have a constant gap size (*g*), metal thickness (*t*), metal width (*w*) and dipole length (*l*), we will not present these parameters again. Our starting antenna geometry of a single dipole is illustrated in Figure 2.9.

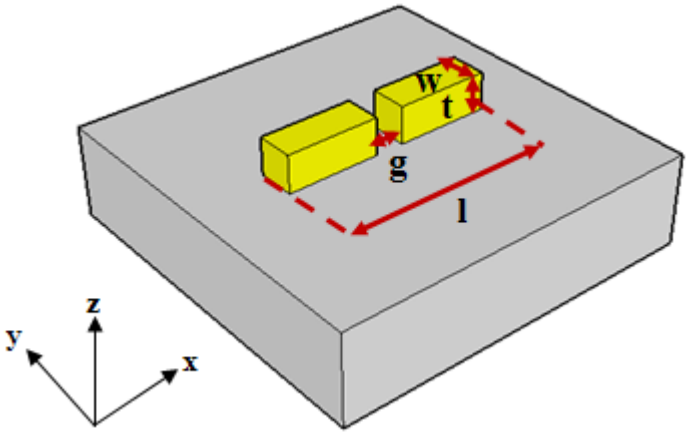

Figure 3.1: Single dipole antenna geometry.

3.2 Simulation Results and Discussion

Our antenna structures and simulation results starting from the single dipole to split ring resonator (SRR) architecture are given in the following subsections one by one.

3.2.1 Single Dipole

Normalized field intensity enhancement averaged over the gap volume of antenna (see Figure 3.3) calculated using (3.1) is plotted in Figure 3.3 as a function of wavelength (in μm). As pointed, the maximum enhancement of 455 is observed at the resonance wavelength of 765 nm.

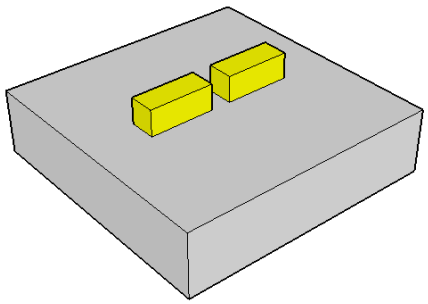

Figure 3.2: Single dipole antenna geometry.

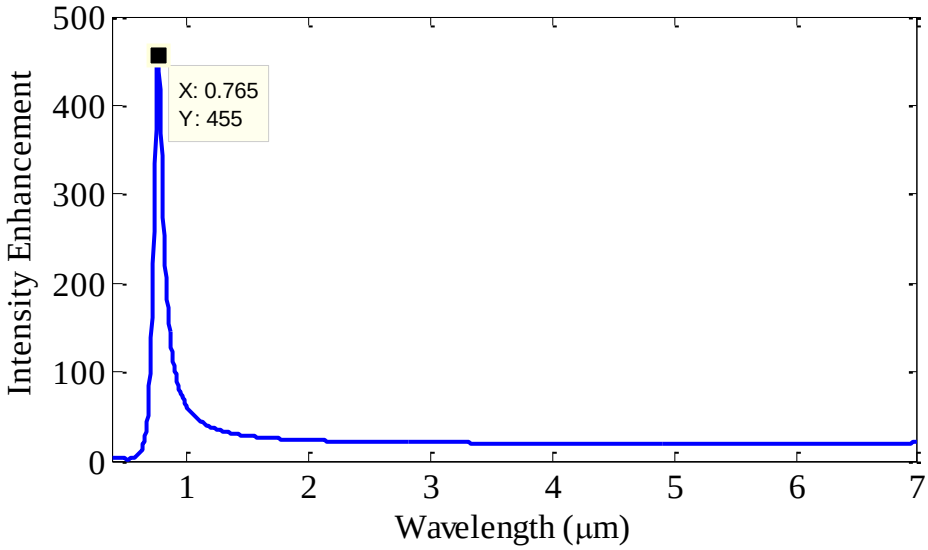

Figure 3.3: Field intensity enhancement with respect to optical wavelength.

To examine the surface currents we examine the magnetic field intensities on surfaces at the resonance wavelength of 765 nm. Figures 3.4-3.9 represent this information for each surface. However, due to the symmetry of surfaces at constant *x* planes, we consider only one arm (in *–x* direction) of dipole. From Figure 3.4-3.9, it is seen that the tangential magnetic field components continuously exist mainly on 4 faces of the antenna arms, which are the bottom, top and constant *y* surfaces.

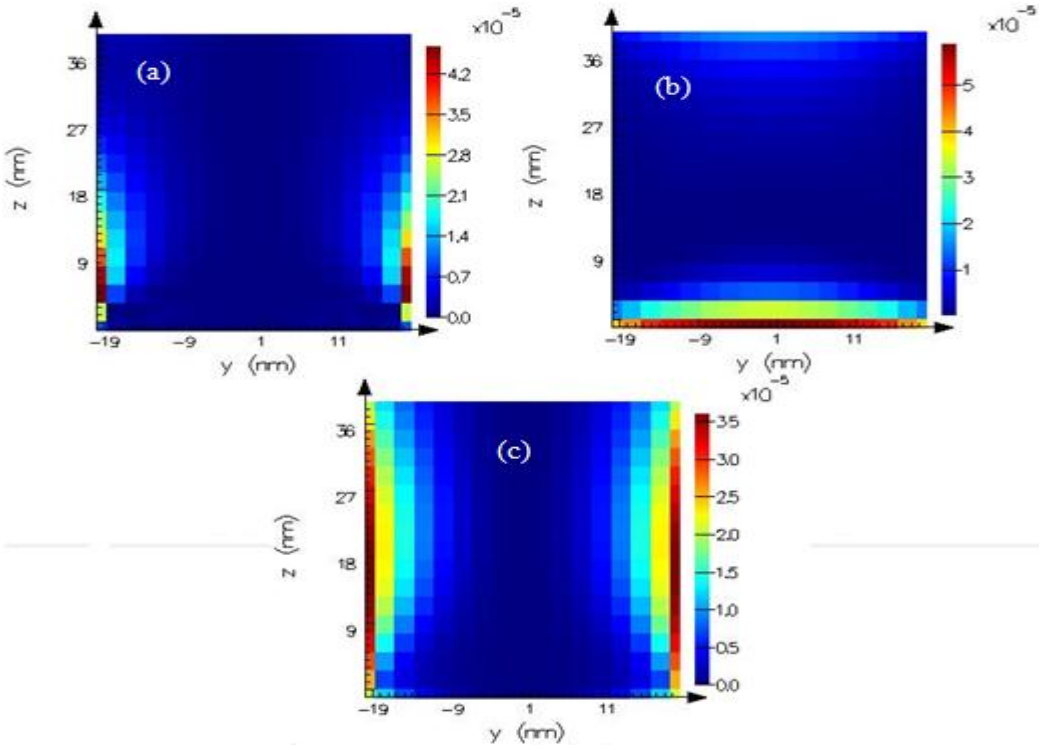

Figure 3.4: Magnetic field component intensities at 765 nm on constant *x* surface (in –*x* direction) of the left arm: (a) H_x, (b) H_y, and (c) H_z.

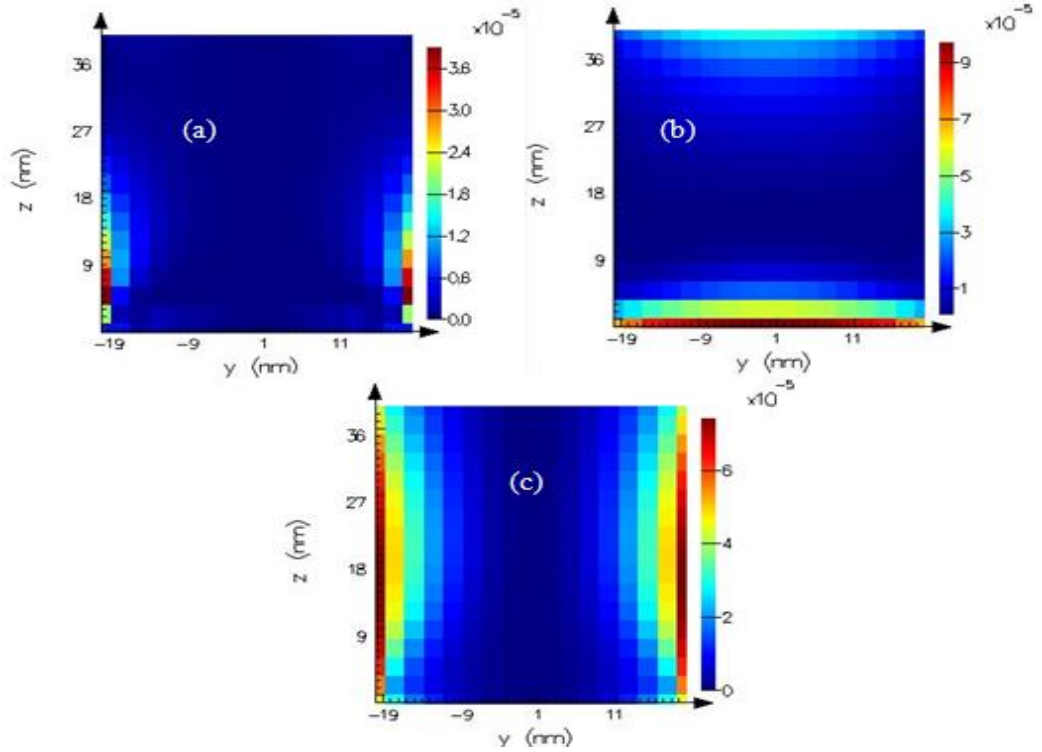

Figure 3.5: Magnetic field component intensities at 765 nm on constant *x* surface (in +*x* direction) of the left arm: (a) H_x, (b) H_y, and (c) H_z.

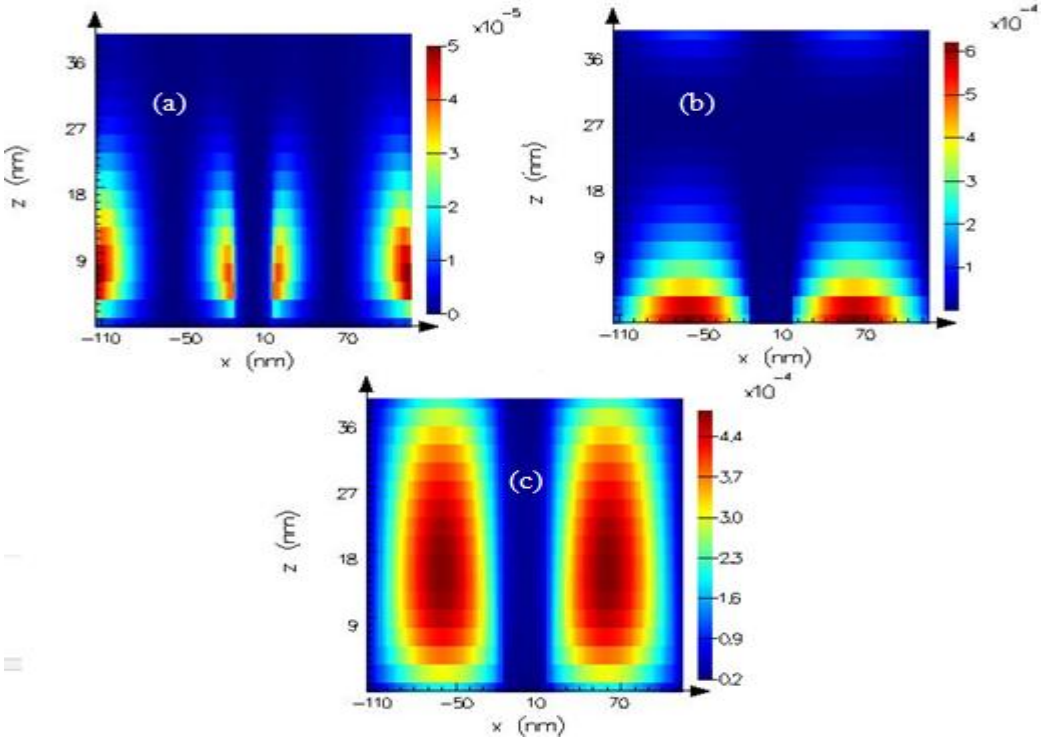

Figure 3.6: Magnetic field component intensities at 765 nm on constant *y* surfaces (in -*y* direction) of both arms together: (a) H_x, (b) H_y, and (c) H_z.

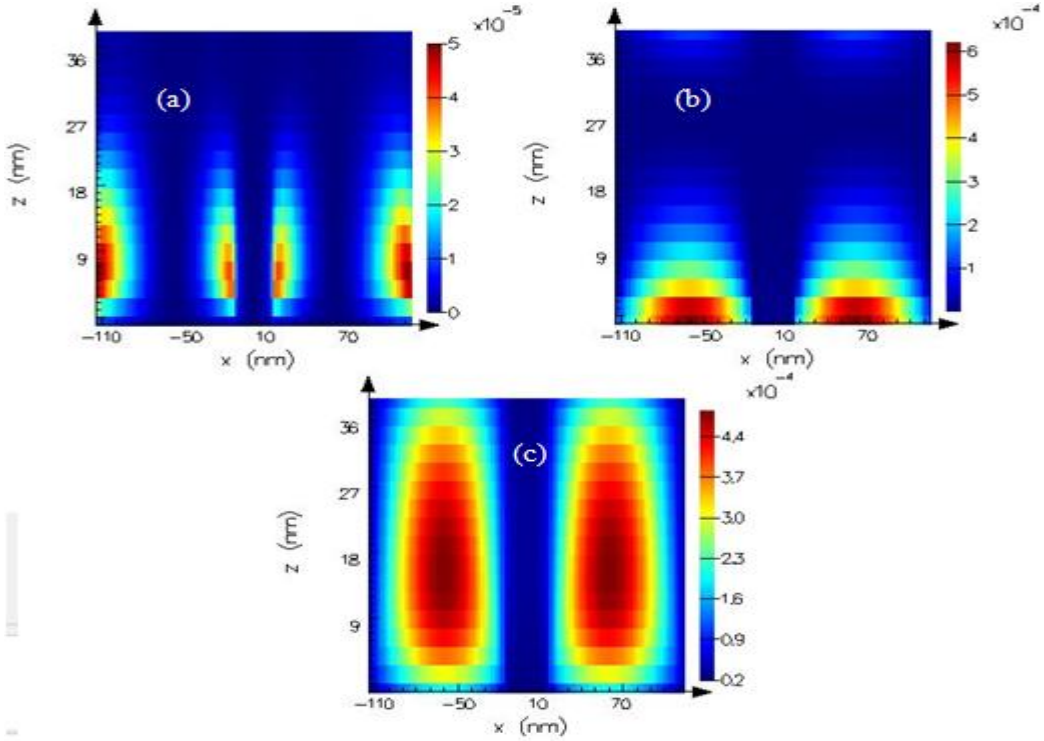

Figure 3.7: Magnetic field component intensities at 765 nm on constant *y* surfaces (in +*y* direction) of both arms together: (a) H_x, (b) H_y, and (c) H_z.

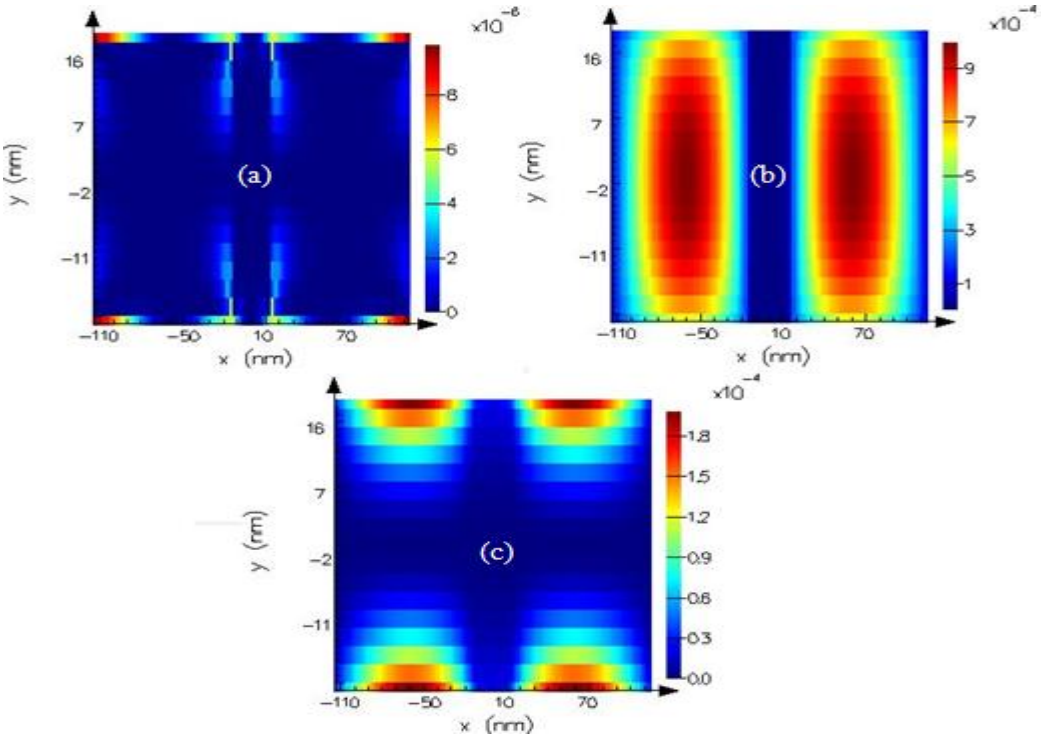

Figure 3.8: Magnetic field component intensities at 765 nm on the antenna`s bottom surface (constant *z* surface in -*z* direction): (a) H_x, (b) H_y, and (c) H_z.

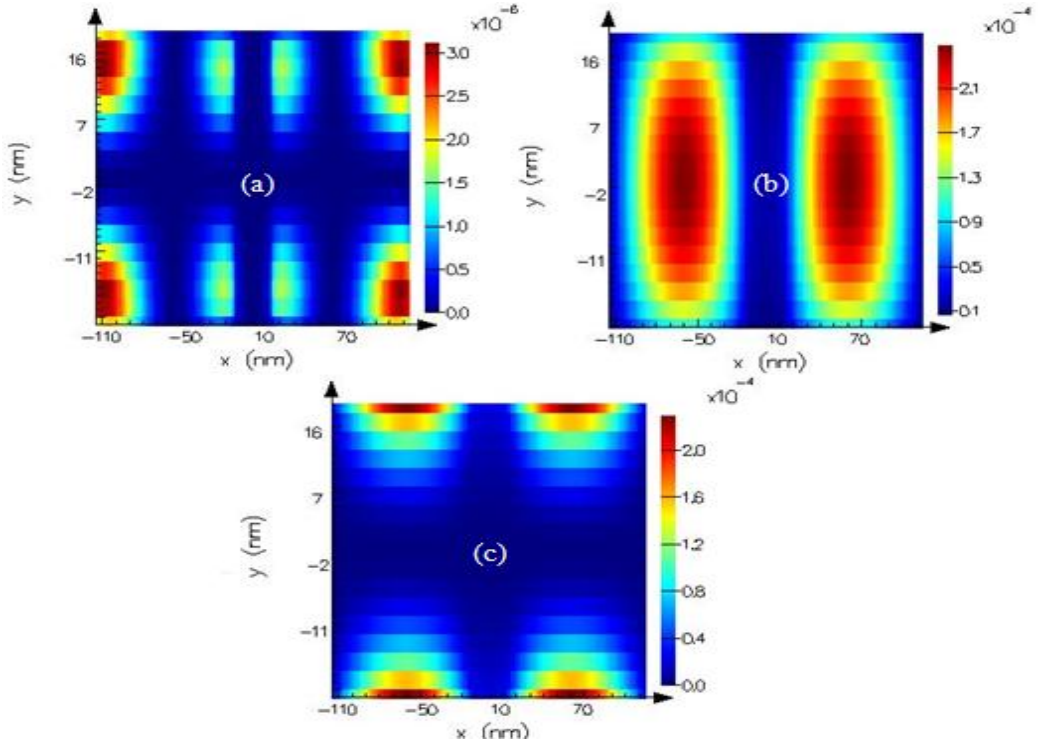

Figure 3.9: Magnetic field component intensities at 765 nm on the antenna`s top surface (constant *z* surface in +*z* direction): (a) H_x, (b) H_y, and (c) H_z.

On the constant x surfaces, the tangential magnetic fields H_y and H_z have very small values on the level of 10^{-5}. They exist only near the edges and are discontinuous. Thus, they do not construct the surface flowing current. They are due to tangential fields and edge discontinuities on the other faces. Besides, on the constant y surfaces, the tangential field H_z is much higher than H_x and is continuous over the surface. Therefore, H_z is the dominant surface tangential field and causes the surface currents on constant y surfaces. In addition, similarly on the bottom and top surfaces, H_y is much higher than H_x and is continuous over the metal surfaces. Therefore, on the top and bottom surfaces, H_y is the dominant surface tangential field and allows for the surface currents. We sketch the tangential magnetic fields roughly, in Figure 3.10.

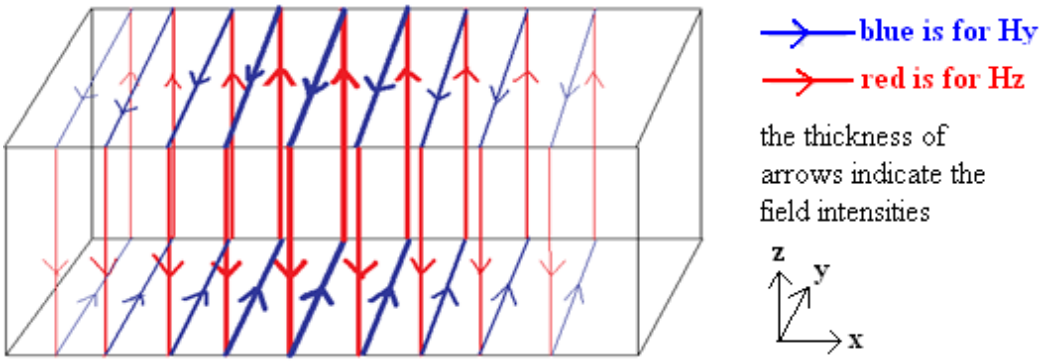

Figure 3.10: Dominant tangential magnetic fields on the surfaces of the dipole arm.

Based on the surface current formula ($\mathbf{n}\times\mathbf{H}=\mathbf{J}_s$), for the above tangential magnetic fields, surface current is directed in $+x$ (from left to right) over these 4 surfaces. Since the field is oscillatory in time, the tangential magnetic fields are oscillatory, too. Thus, the surface currents are oscillatory, too, in time pointing $\pm x$ directions.

Moreover, as expected, continuous tangential magnetic field (H_y) is smaller on the top surface than on the bottom surface and the tangential field intensities are the same on constant y surfaces because of the symmetry. Consequently, the surface current flow is larger on the bottom surface than the top surface and is similar on constant y surfaces. Also as seen from the field plots of the bottom

surface, there is no current flowing in the gap region. This is expected, too, because of SiO_2 properties.

In summary, it can be said that the surface current flows over 4 surfaces (top, bottom and constant *y* surfaces) in $\pm x$ directions. They are continuous over these surfaces, but at the edges they encounter discontinuities and thus they radiate.

3.2.2 Double Dipoles (with *s* =100 nm center-to-center distance)

Because of the symmetry, the field intensities that we calculate inside the dipole gap regions (Figure 3.11) are the same. Therefore, the normalized field intensity enhancements averaged over the gap volumes of either of the antennas calculated using (3.1) is plotted in Figure 3.12.

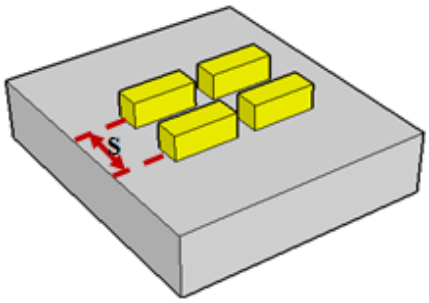

Figure 3.11: Double dipoles with s=100 nm center-to-center distance.

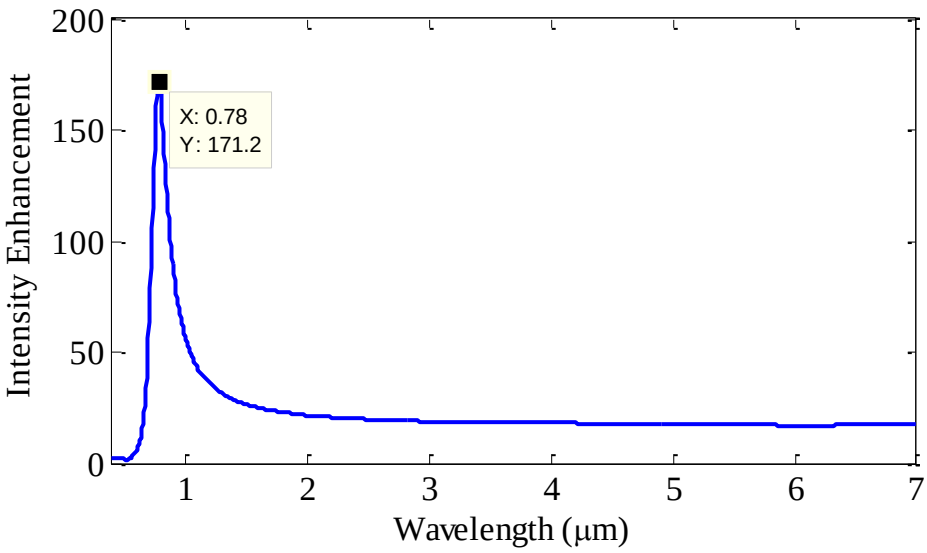

Figure 3.12: Field intensity enhancement of the double dipoles.

The maximum enhancement of 171.2 is observed at the resonance wavelength of 780 nm. If we compare with the single dipole results, the intensity enhancement decreases by 283.8 and the resonant wavelength red-shifts by 15 nm. The reason of these observations is the coupling of dipoles. The radiated fields from an antenna propagate and interact with the fields or surface currents of the other antenna. Here, this interaction happens destructively.

In addition, when we examine magnetic fields on the surfaces, it is observed that the magnetic field and current behaviors of double dipole structure is similar to those of single dipole structure. More clearly, the dominant tangential magnetic field components are H_y and H_z on the constant z and constant y surfaces, respectively. These fields are continuous and create the surface currents on these four surfaces. In addition, there is no current flow inside the gap region and on constant x surfaces. Also similar to the single dipole case, surface currents on the bottom surface is expectedly larger than on the top surface.

On the other hand, there are also some differences between the single and double dipole case results. First, due to coupling, the tangential magnetic fields and hence surface currents are lower in the double dipole antenna (with a separation distance s=100 nm). This is the reason why the *E*-field intensity at the gap is less for the double dipole case. In addition, again due to coupling, the magnetic fields and thus the surface currents are not the same for the constant y plane surfaces of the metal arms.

3.2.3 Double C-shape (with s =100 nm center-to-center distance)

When we connect the double dipoles in Figure 3.11 with the same metal part of 40 nm in width (made of Au), our structure turns into a double C-shape pair as sketched in Figure 3.13.

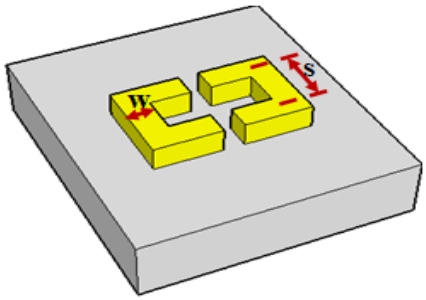

Figure 3.13: Double C-shape antenna structure (with s=100 nm center-to-center distance and w=40 nm width).

Again, because of the symmetry, the field intensities that we calculate inside the gap regions are the same. The normalized field intensity enhancements averaged over the gap volumes calculated using (3.1) is plotted in Figure 3.14.

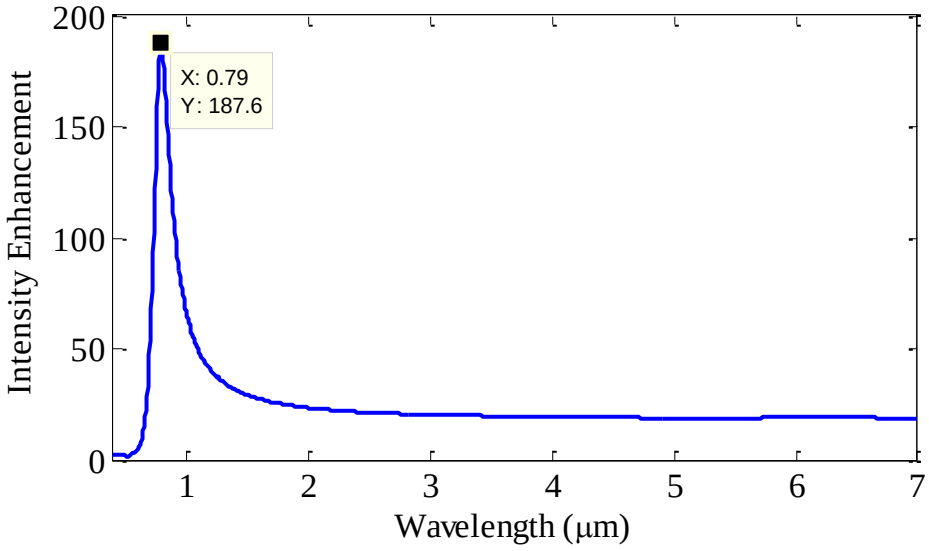

Figure 3.14: Field intensity enhancement of double C-shape pair.

The maximum enhancement of 187.6 is obtained at the resonance wavelength of 790 nm. If we compare with the previous case (the double dipoles with *s*=100 nm distance), the enhancement peak is stronger in the double C-shape case (by an amount of 16.4) and the resonance wavelength is red-shifted by 10 nm. Although we expect it to be stronger, this little enhancement in the field intensity is due to the end connections of dipoles. When we connect the dipoles, radiations from the edges and corners on the end surfaces, which do not

look into gap regions, decrease. This can be seen by mapping the electric field intensities.

The *x*-*y* top view of our double C-shape antenna structure is given in Figure 3.15. To be clear in the explanations below, we named the dipoles as antenna 1 and 2, and represent the *x* and *y* coordinates of locations. Again, because of the symmetry, examining the magnetic fields and the surface currents on one C-shape antenna is acceptable.

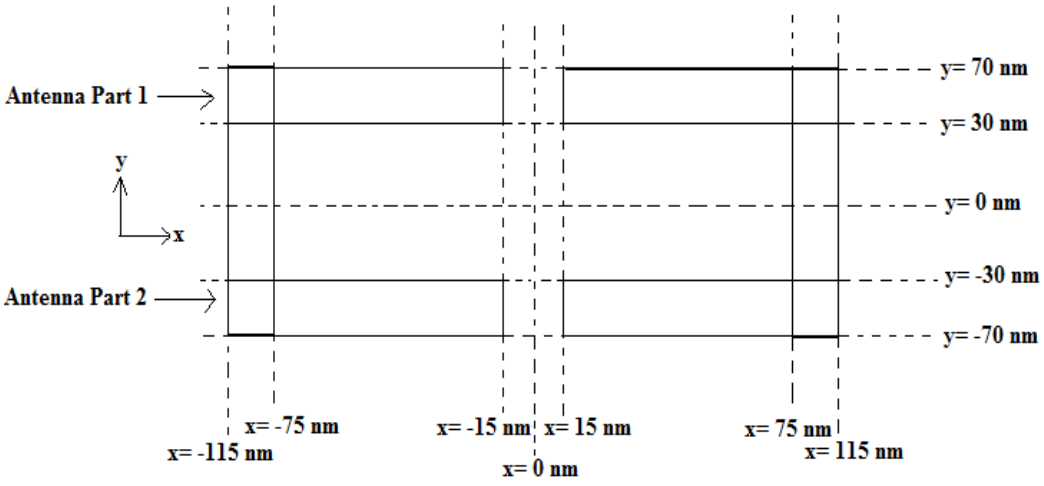

Figure 3.15: Top perspective of our double C-shape antenna.

Based on the examination of the magnetic fields on the surfaces of the right C-shaped antenna on resonance, our observations are as follows. First, H_z is the dominant tangential field component on constant *y* surfaces and H_y is the dominant tangential field component on constant z surfaces (top and bottom) of dipoles (antenna parts 1 and 2), which is similar to unconnected double dipole. However, H_y magnitudes and their surface currents are stronger on the bottom surfaces than on the top surfaces of the dipoles, which are expected as in the previous cases. Similarly, H_z magnitudes and their surface currents are weaker on the inner surfaces ($y=\pm 30$ nm) than on the outer surfaces ($y=\pm 70$ nm) of the dipoles. The magnitude of H_z is very large at the edges ($x=75$ nm, $y=\pm 30$ nm) of the inner surfaces of antenna parts 1 and 2, but this sharply reduces at the edges, which indicates the discontinuity of the surface current and so does the

radiation. Moreover, as in the single dipole, there is no continuous tangential magnetic field and, therefore, there is no current flow on x=15 nm surfaces of the antennas. Only the reactive magnetic fields, which occur due to the edge discontinuities on the surfaces, or the extensions of tangential magnetic fields of the side faces are seen.

In addition, the dominant tangential magnetic field component is H_y on the bottom (z=0 nm) surface of the right connection (75 nm < x < 115 nm) and it is the largest at the intersection parts with the antenna parts 1 and 2 and lower at the middle part. It is somehow lower than H_y field on the bottom surface of the antenna parts 1 and 2 but it is still on the order of 10^{-4}. Therefore, the current is in the same direction ($\pm x$) on the bottom (z=0 nm) surface of the whole C-structure. On the other hand, the tangential magnetic field (H_y) intensity on the upper (z=40 nm) surface is much lower than the bottom (z=0 nm) surface. It is on the order of 10^{-5} at the intersection parts with the antenna parts 1 and 2 (near of the edges) and lower at the middle part. Thus, the surface current on the top surface is too small. Similarly, the tangential magnetic field components (H_y and H_z) are very small on x=115 nm surface (right surface of the right connection). Only the reactive components of the side faces' tangential fields are seen near the edges. This means that the current flow is very low on x=115 nm surface of the connection part. Furthermore, the tangential H-field components are very small on the x=75 nm surface, too. H_z ~$1.4\text{x}10^{-4}$ is observed near the edges (y=-30 and 30 nm), but between them it decreases and at the middle it is too low. Therefore, there is no noticeable current flow on x=75 nm face of the right connection.

As a result, the current density $\mathbf{J_S}$ is directed along $\pm x$ on the first and second dipole antenna arms (antenna parts 1 and 2) and also on the connection part. However, on the upper, right and left faces (3 faces except z=0 nm face) of the right connection, the currents are very weak. Therefore, most of the current discontinue at the edges and corners; so, they radiate. The remaining current

flows mostly through the bottom surface of the right connection. Since our structure is symmetric with respect to x=0 nm plane, these results also hold for the left C-shaped part. The dominant tangential magnetic fields and their resulting surface currents are illustrated in Figures 3.16 and 3.17, respectively.

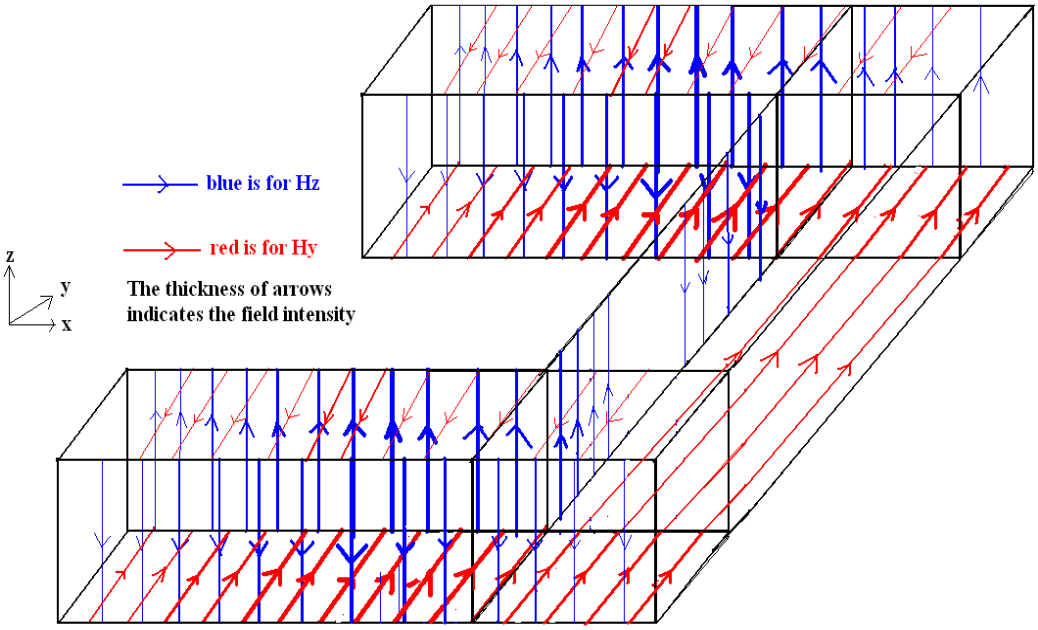

Figure 3.16: Dominant tangential field components.

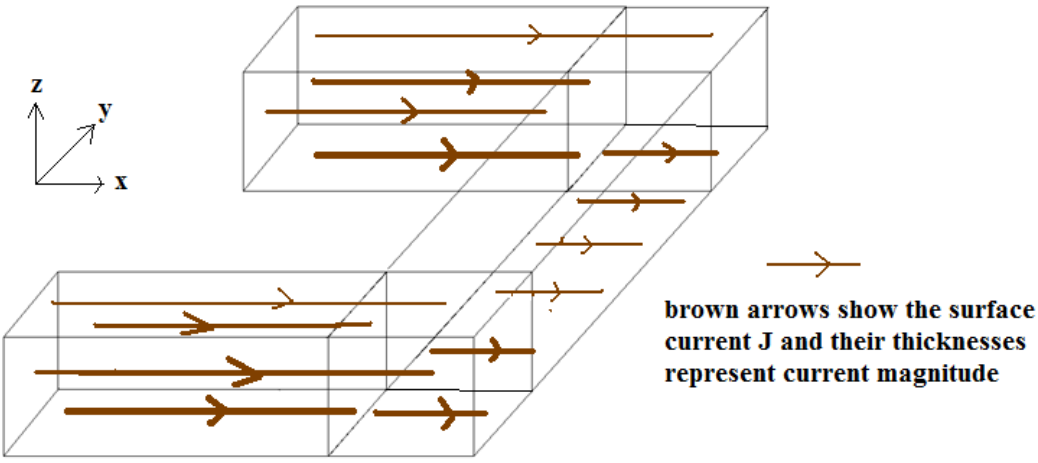

Figure 3.17: Surface current flows on double C-shaped antenna (on right part) (J= nxH).

3.2.4 Split Ring Resonator (SRR) Shape (Connected Double C-shapes) (with *s* =100 nm center-to-center distance)

At last when we combine one of the antenna arms of the double C-shape structure (in Figure 3.13), we obtain our targeted structure of the split ring resonator (SRR) shaped antenna. Its structure is presented in Figure 3.18. The normalized field intensity enhancement averaged over the gap volume calculated using (3.1) is plotted in Figure 3.19.

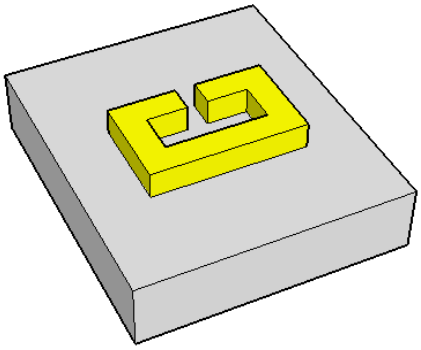

Figure 3.18: SRR-shaped antenna structure.

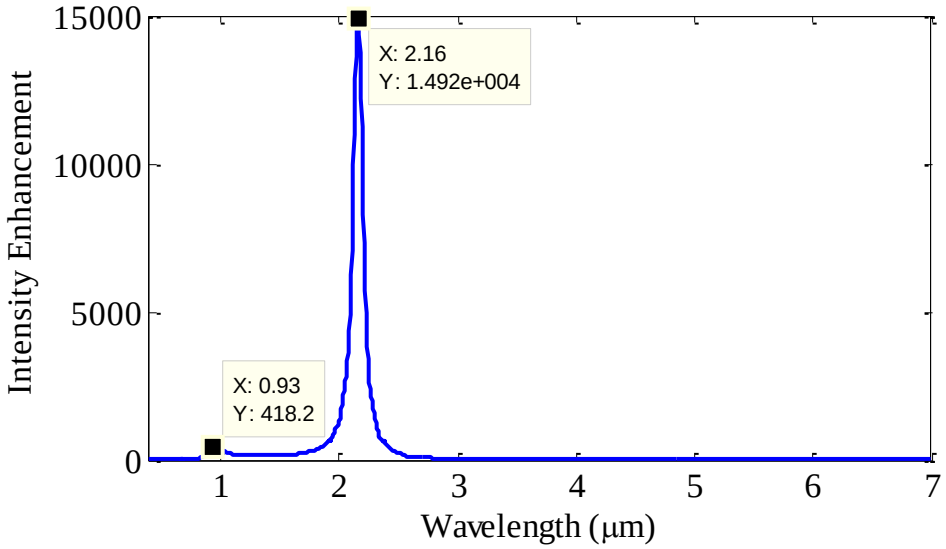

Figure 3.19: Field intensity enhancement of SRR.

As seen, with our simple connection, the peak value of field intensity enhancement increases by nearly 80 times (from 187.6 to 14920) and its wavelength red-shifts by 1370 nm (from 790 to 2160 nm). In addition, in SRR antenna, more than one peak is observed. This additional peak at the shorter wavelength (or at higher frequency) corresponds to the higher order mode supported by our new SRR antenna architecture.

To see its relation with the surface currents, we examined the magnetic field components on the surfaces of our SRR antenna on both resonances. Since our structure still exhibits symmetry in *x*-direction, it is acceptable to investigate and plot fields on surfaces of either left or right antenna parts. To make our plots and comments more clear, we roughly sketched SRR geometry from top view with some labels and coordinates presented in Figure 3.20.

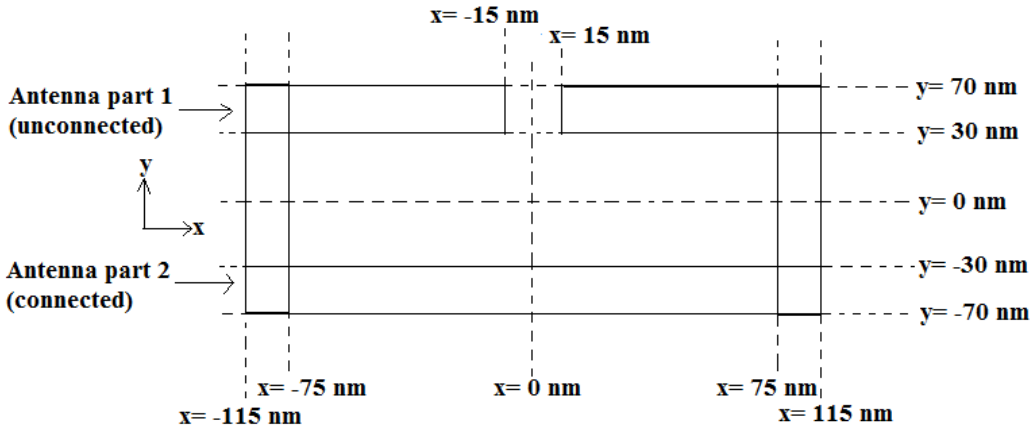

Figure 3.20: Top view of our SRR-shaped antenna.

We first analyzed the magnetic field intensities on the surfaces at the resonance wavelength of 2160 nm. Figures 3.21-3.25 represent the magnetic field maps for each surface. Let`s start with the surfaces of antenna part 1.

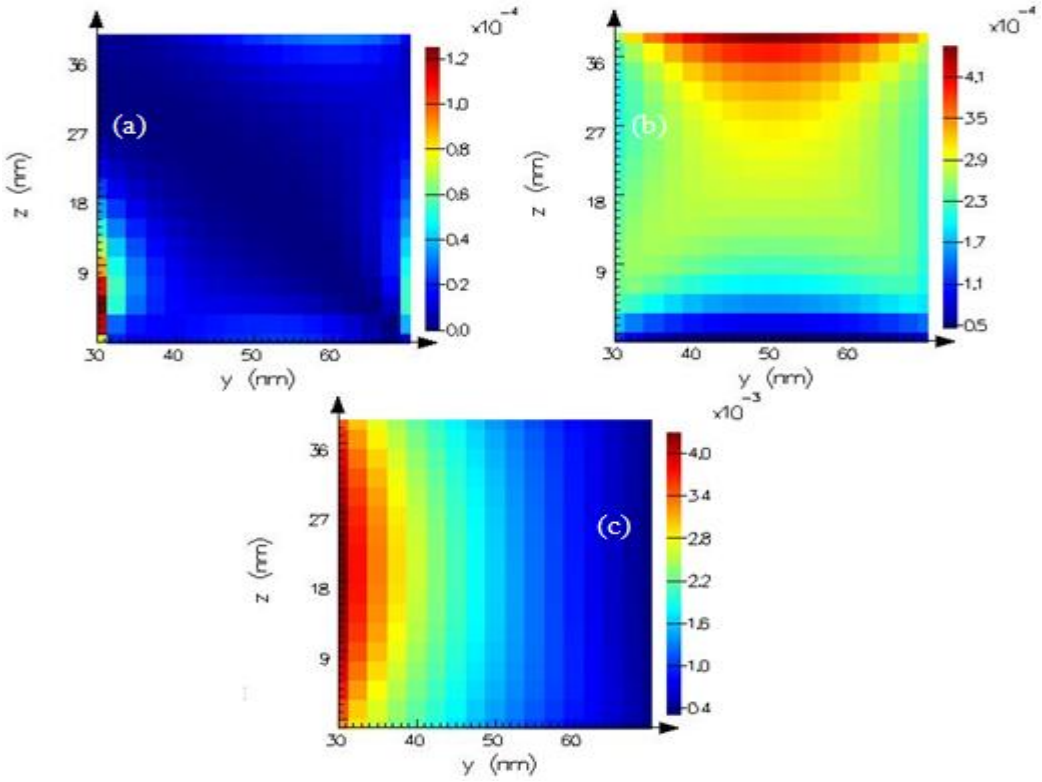

Figure 3.21: Magnetic field component intensities at 2160 nm on constant *x=15 nm* surface of antenna part 1 right arm: (a) H_x, (b) H_y, and (c) H_z.

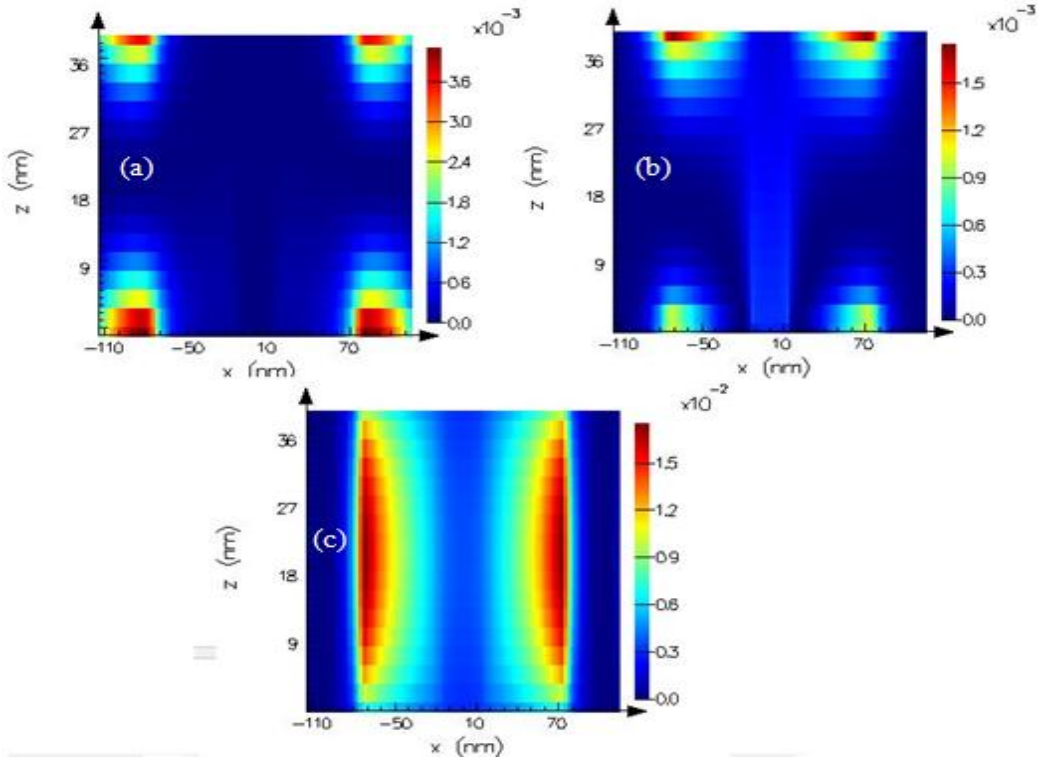

Figure 3.22: Magnetic field component intensities at 2160 nm on constant *y=30 nm* surface of antenna part 1: (a) H_x, (b) H_y, and (c) H_z.

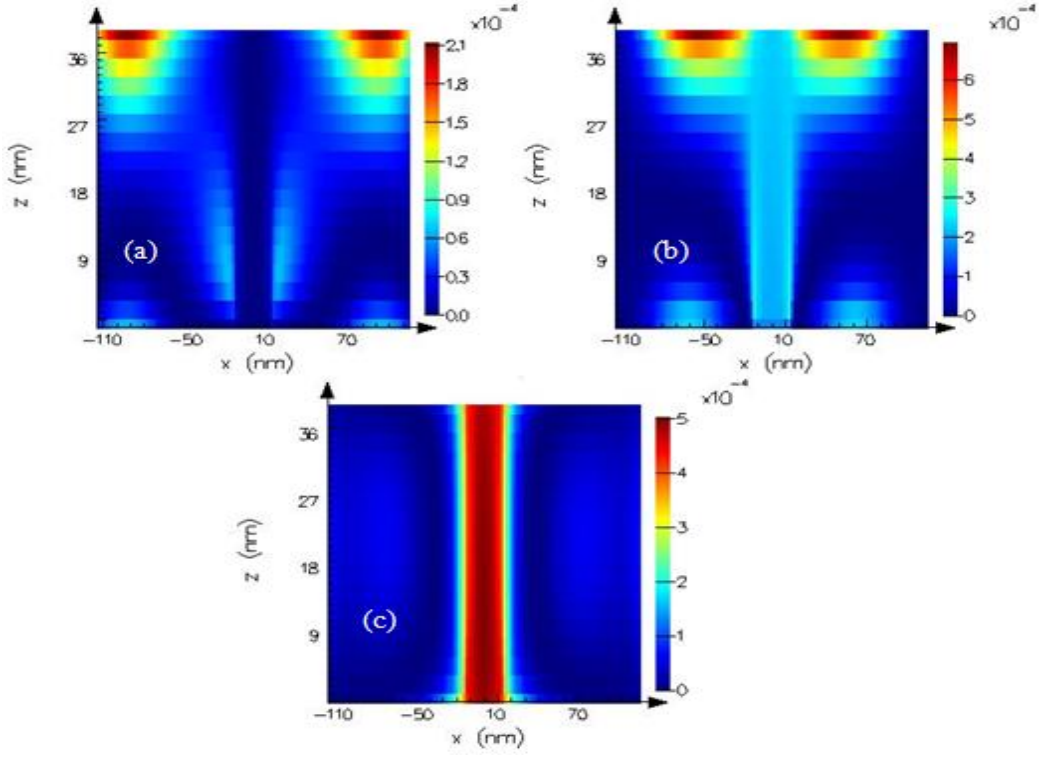

Figure 3.23: Magnetic field component intensities at 2160 nm on constant *y=70 nm* surface of antenna part 1: (a) H_x, (b) H_y, and (c) H_z.

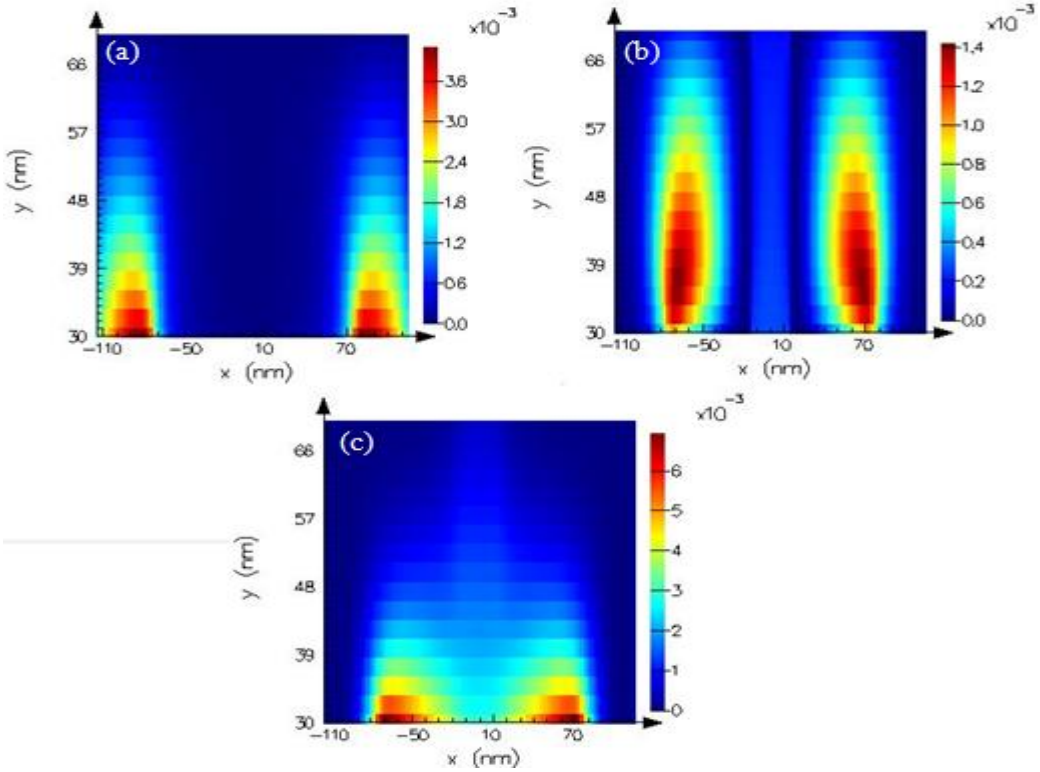

Figure 3.24: Magnetic field component intensities at 2160 nm on constant *z=0 nm (bottom)* surface of antenna part 1: (a) H_x, (b) H_y, and (c) H_z.

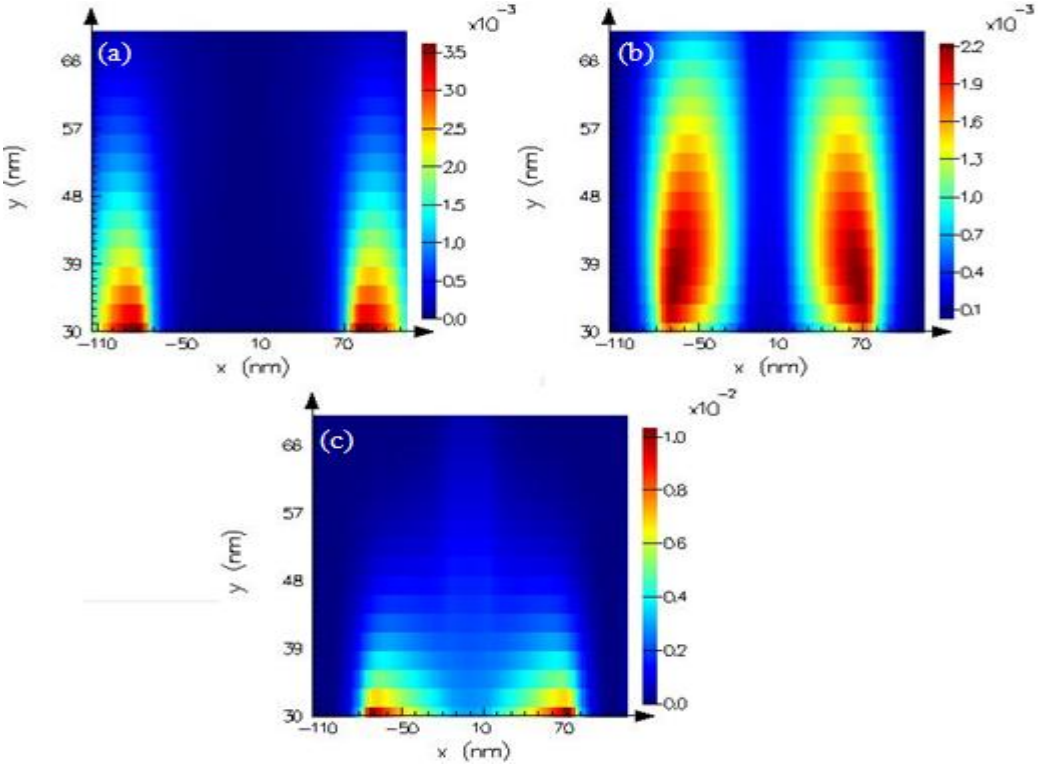

Figure 3.25: Magnetic field component intensities at 2160 nm on constant *z=40 nm (top)* surface of antenna part 1: (a) H_x, (b) H_y, and (c) H_z.

We can conclude from Figure 3.21-Figure 3.25 that for the unconnected dipole antenna (antenna part 1) H_z is the dominant and continuous tangential magnetic field component on constant y=30 nm surface and H_y is the dominant and continuous tangential magnetic field component on constant z=0 nm (bottom) and z=40 nm (top) surfaces. As expected from very large field enhancements, these tangential magnetic fields are much higher than the tangential magnetic fields on the surfaces of unconnected double C-shaped antenna. For the SRR case, H_z is on the order of 10^{-2} and H_y is on the order of 10^{-3}. However, different from the previous simulations, there is no considerable amount of continuous tangential magnetic field over y=70 nm surface. Again different from previous simulations, the tangential magnetic field component H_y on z=40 nm surface is slightly stronger than H_y on z=0 nm surface, but this difference is not too large and can be as well due to simulation inaccuracy. In addition, H_z magnitude is very large at the edge of the inner surface of antenna part 1 (x=$\pm$75 nm and y=30 nm). We expect H_z to sharply reduce at the edge, which indicates the discontinuity of surface current and the radiation, but it is continuous as the right connection part as we observe in Figures 3.26-3.29. Furthermore, as in the case of unconnected double C-shapes, there is no considerable amount of continuous tangential magnetic field and hence no current flow on x=15 nm surface. Only the reactive magnetic fields or the extensions of tangential magnetic fields of the neighbor faces are observed.

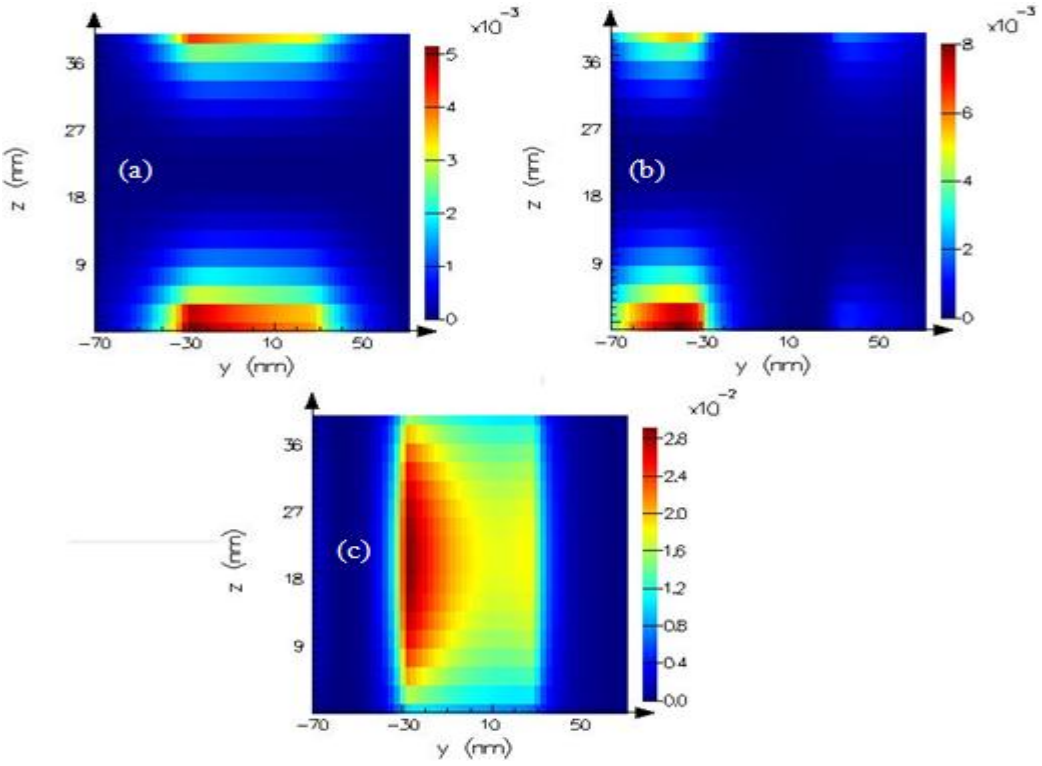

Figure 3.26: Magnetic field component intensities at 2160 nm on constant *x=75 nm* surface of the right connection part: (a) H_x, (b) H_y, and (c) H_z.

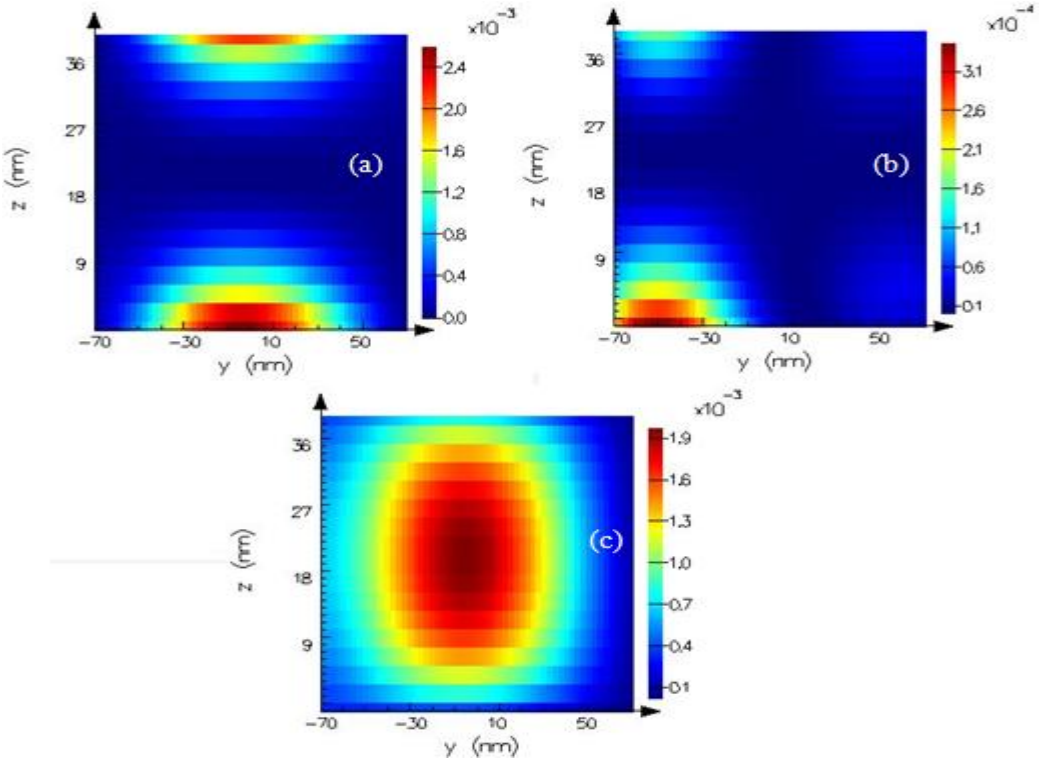

Figure 3.27: Magnetic field component intensities at 2160 nm on constant *x=115 nm* surface of the right connection part: (a) H_x, (b) H_y, and (c) H_z.

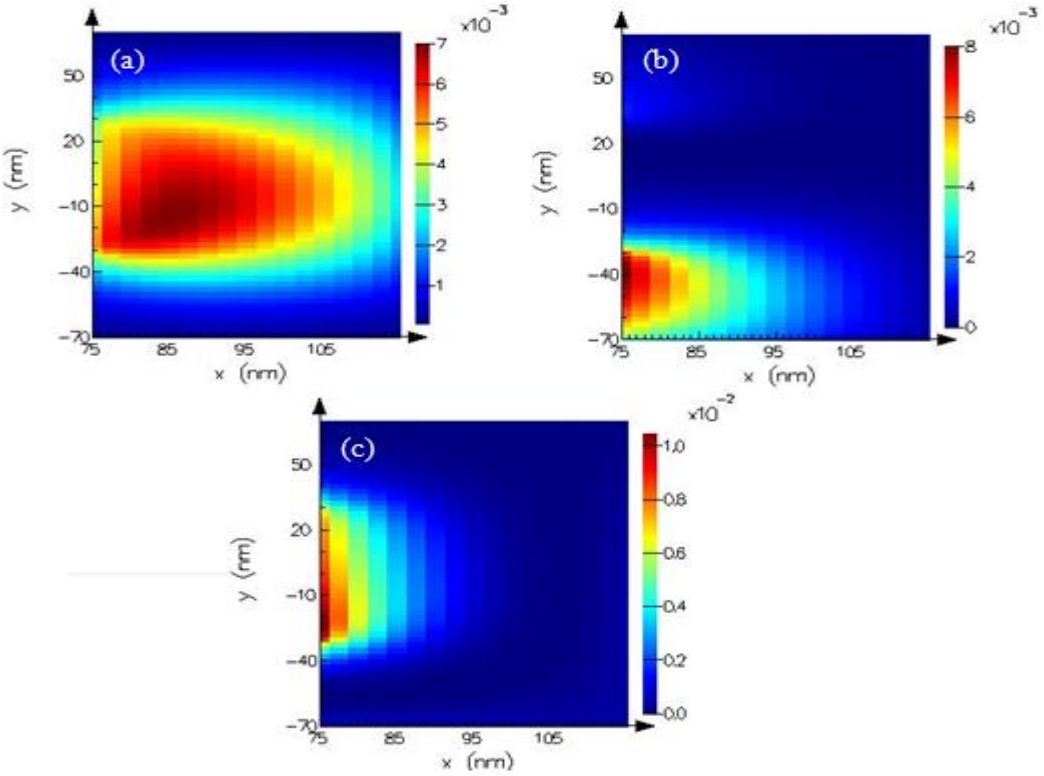

Figure 3.28: Magnetic field component intensities at 2160 nm on constant *z=0 nm (bottom)* surface of the right connection part: (a) H_x, (b) H_y, and (c) H_z.

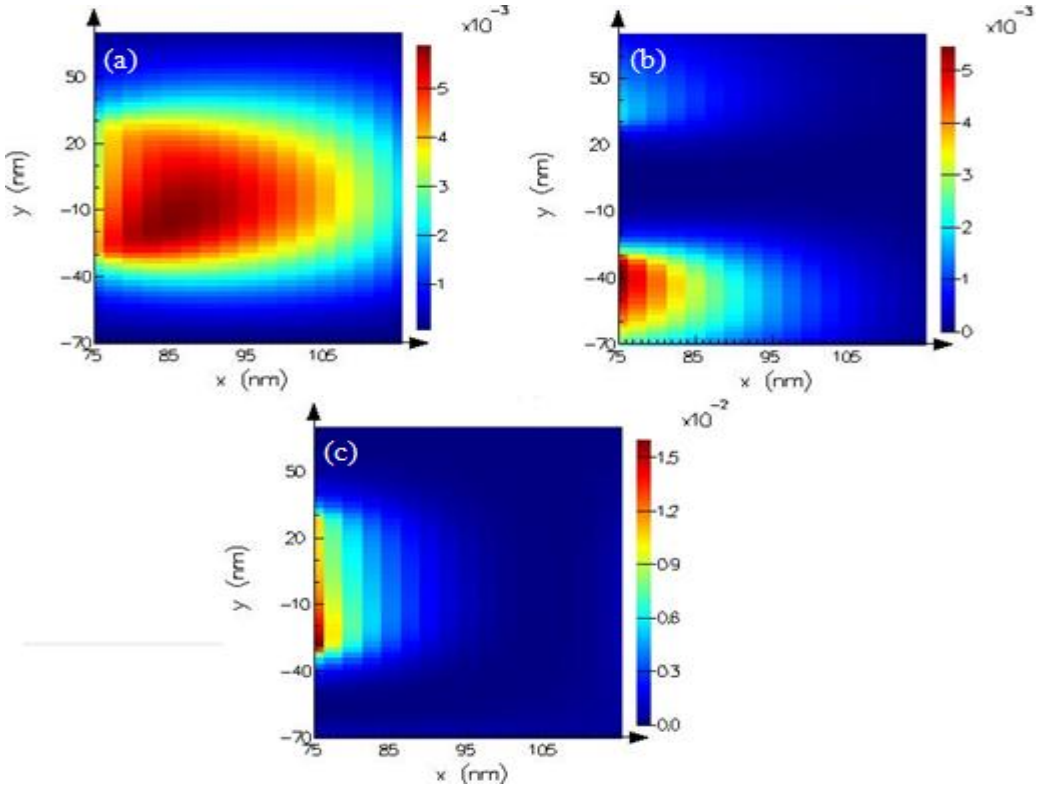

Figure 3.29: Magnetic field component intensities at 2160 nm on constant *z=40 nm (top)* surface of the right connection part: (a) H_x, (b) H_y, and (c) H_z.

Next we continue with the right connection part, which ties antenna part 1 and antenna part 2 in Figure 3.20. It is conferred from Figure 3.26-Figure 3.29 that in SRR-shaped antenna there is a huge amount of tangential field H_z on the inner surface (x=75 nm) of the right connection part, which is different from unconnected double C-shapes. It has a considerably huge value, i.e., 2.8×10^{-2} near y=-30 nm edge and 1.8×10^{-2} near y=30 nm edge. Also these figures represent us that this field is a result of continuation and interaction of the H_z tangential fields on antenna parts 1 and 2. Consequently, this H_z is the dominant and continuous tangential field component on x=75 nm constant surface of the right connection part and this results in the surface current flowing in $\pm y$ directions.

Similarly, on the outer surface (x=115 nm) of the right connection, H_z is the dominant and continuous tangential magnetic field. It is substantially smaller than H_z fields on the inner surface, i.e., on the order of 10^{-3}. Therefore, the surface current flow on the outer surface (x=115 nm) of the right connection part is in the same direction with the inner (x=75 nm) surface (along $\pm y$ directions) but it is smaller in magnitude.

Very interestingly and different from previous simulations, the continuous and dominant tangential field component on the bottom (z=0 nm) and top (z=40 nm) surfaces of the right connection is H_x, which is on the order of 1×10^{-3}. Therefore, the surface current flow is along $\pm y$ directions on the bottom and top surfaces of the connection part.

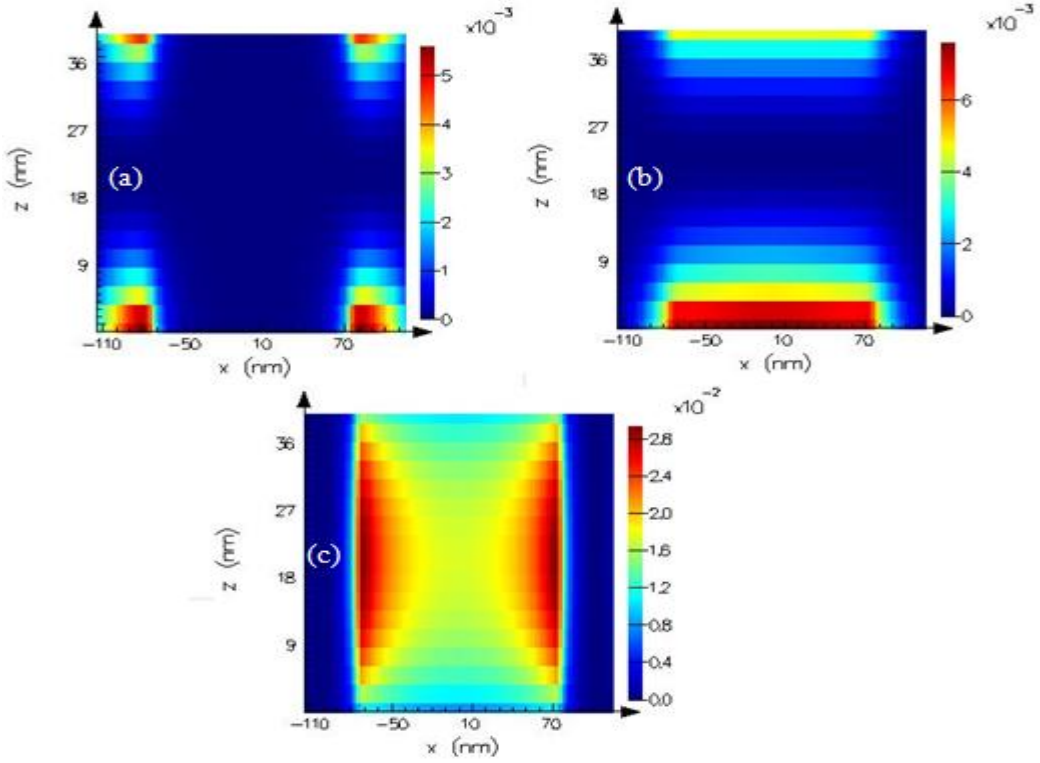

Figure 3.30: Magnetic field component intensities at 2160 nm on constant *y=-30 nm* surface of antenna part 2: (a) H_x, (b) H_y, and (c) H_z.

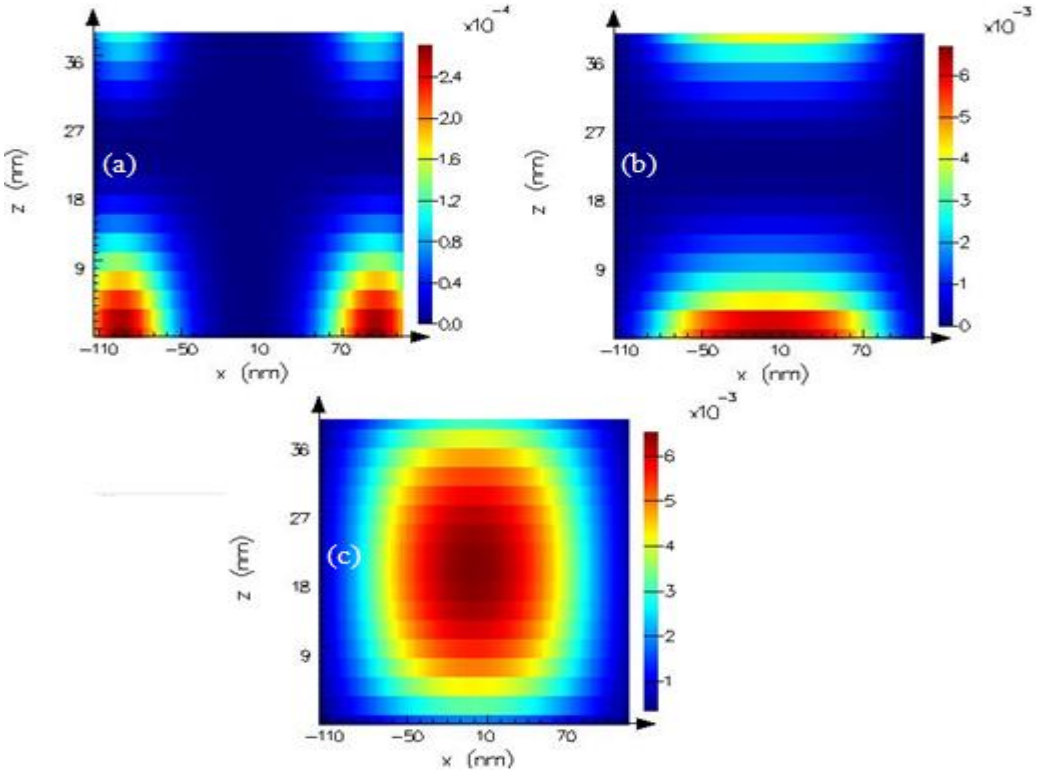

Figure 3.31: Magnetic field component intensities at 2160 nm on constant *y=-70 nm* surface of antenna part 2: (a) H_x, (b) H_y, and (c) H_z.

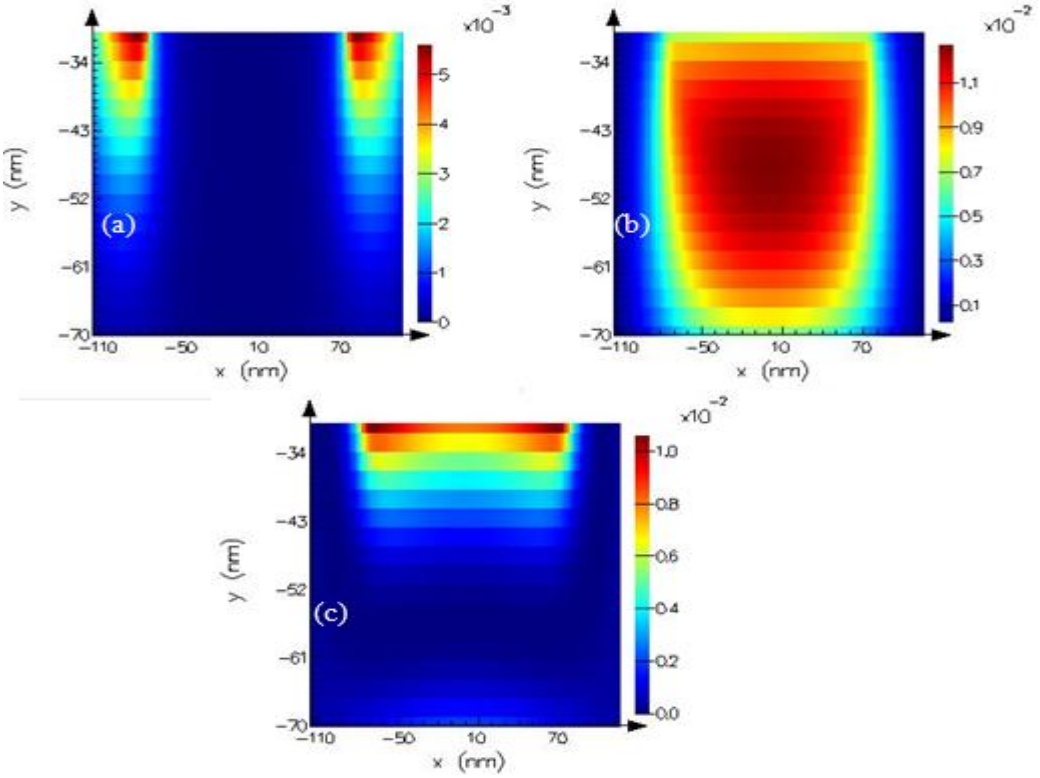

Figure 3.32: Magnetic field component intensities at 2160 nm on constant *z=0 nm* (bottom) surface of antenna part 2: (a) H_x, (b) H_y, and (c) H_z.

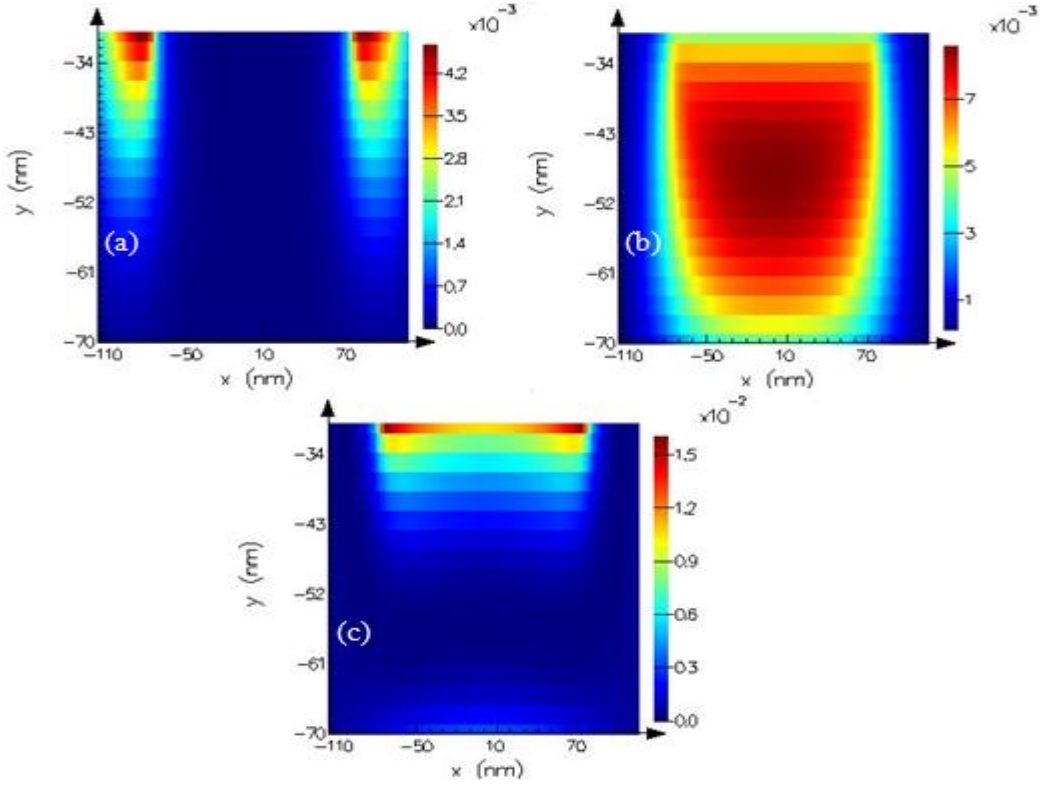

Figure 3.33: Magnetic field component intensities at 2160 nm on constant *z=40 nm* (top) surface of antenna part 2: (a) H_x, (b) H_y, and (c) H_z.

At the third step, let's examine the magnetic field components on the surfaces of antenna part 2 (as named in Figure 3.20). It is observed from Figure 3.30-Figure 3.33 that H_z is the dominant and continuous tangential field component on the inner (y=-30 nm) surface of antenna part 2. It has the largest value of $\sim 2.8 \times 10^{-2}$ near the edges (x=$\pm$75 nm) and decreases towards the middle. Therefore, the current flow on the inner (y=-30 nm) surface of antenna part 2 is along $\pm x$ directions.Similarly, on the outer (y=-70 nm) surface of antenna part 2, H_z is the dominant and continuous tangential field component. It has the largest value of nearly 6×10^{-3} in the middle and decreases towards the edges. Consequently, the surface current flow on the outer surface is in the same direction ($\pm x$) with the inner surface but with lower intensity.

In addition, similar to unconnected double C-shape result, the continuous and dominant tangential magnetic field component is H_y on the bottom (z=0 nm) and top (z=40 nm) surfaces of antenna part 2. It is maximum in the middle and decreases towards edges. Also, as expected, H_y is larger on the bottom surface than the top surface but on both surfaces it is much larger than H_y fields on the same surfaces of unconnected double C-shape antenna. As a result, surface currents on bottom and top surfaces are in $\pm x$ directions with magnitudes much stronger than currents on the same surfaces of our previously simulated antenna structures.

In summary, all these figures (Figure 3.21-Figure 3.33) indicate that the current density **J** is directed along $+x$ on the first unconnected dipole arm (antenna part 1), along $-y$ on the right connection part and along $-x$ on the second connected dipole (antenna part 2) in the first half time period and reversed in the second half time period. It means that current flows over SRR-shaped antenna continuously by shaping a loop. This current flow is much higher than the currents of other antenna geometries that we have examined. Also, the current flows on the surfaces, which look inside region, are much higher than flows on the surfaces, which look outside. These currents are

continuous in magnitude, i.e., they smoothly flow at the edges between dipoles (antenna parts 1 and 2) and the connection part. Therefore, the radiations from edges and corners are very small in SRR-shaped antenna than other cases. It means that we reached our goal of increasing field localization inside the gap region by connecting end points of the dipoles, which decreases radiations from end points and allows continuous current flow.

Since our structure is symmetric with respect to x=0 nm plane, these results are hold true for the left part, too. If we plot resultant surface currents, they will be as in Figure 3.34, where we again facilitated from the symmetry.

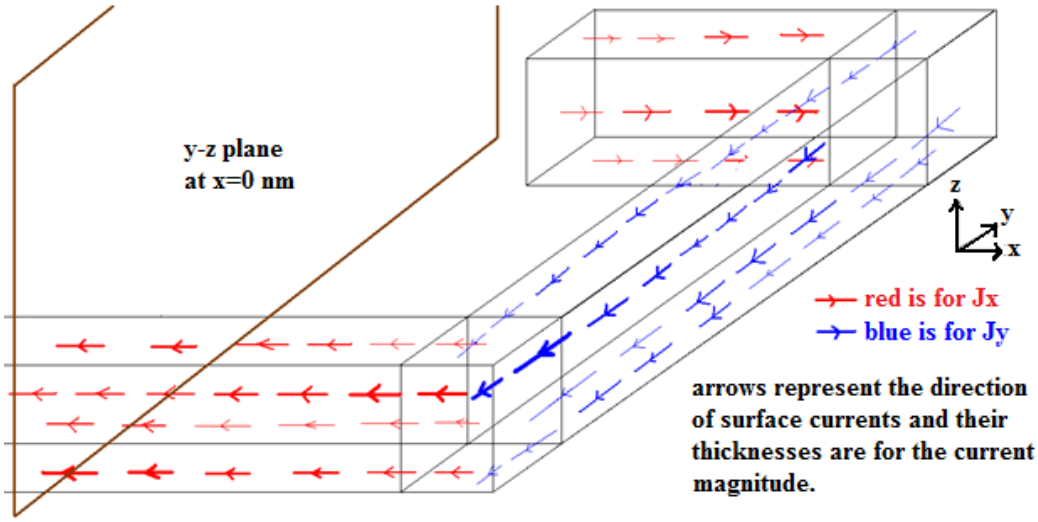

Figure 3.34: Surface currents on SRR-shaped antenna (only its half shown due to the symmetry).

After examining resonance at 2160 nm, we analyzed the magnetic field intensities and the currents on the surfaces of SRR-shaped antenna at the other resonance wavelength of 930 nm. First, we immediately observed that the tangential fields and so the surface currents are smaller on resonance at 930 nm than on resonance at 2160 nm, which is consistent with the field enhancement values. Also, we found that the dominant and continuous tangential magnetic field components are similar within the 2160 nm resonance case. In other words, on the bottom and top faces of unconnected and connected dipoles (antenna parts 1 and 2) H_y is the dominant and continuous tangential magnetic field

component; on the other (constant y) faces, H_z is dominant and continuous. But for the right connection part, H_x is the dominant and continuous field on the bottom and top surfaces; on the other (constant x) faces, H_z is the dominant and continuous one. Therefore, the current path is the same with the path of excitation at 2160 nm wavelength on resonance, i.e., it flows in $\pm x$ directions on antenna parts 1 and 2 and $\pm y$ directions on the right and left connection parts. In short, current still circulates on SRR antenna by forming a loop.

However, two main dissimilarities are observed. First, the intensity distributions and, therefore, peak locations of tangential field components are different. This is explained by the fact that different modes are being supported by antenna at these different resonance wavelengths. Second aberration is that, because the magnitudes of dominant and continuous magnetic fields decrease, the magnitudes of refractive field components become comparable with them. Therefore, discontinuous surface currents become comparable to continuous surface currents especially near edges and corners.

3.3 Conclusion

In conclusion, in this chapter we examined the normalized field intensity enhancement changes and its relationship with the resulting surface currents for different antenna geometries starting from single dipole to SRR shape step by step.

We first simulated single dipole nanoantenna using a chosen set of geometrical parameters and observed an averaged field intensity enhancement of 455 inside the gap region on resonance at 765 nm wavelength. This stems from tangential magnetic field intensity distributions on resonance such that the surface current is along $\pm x$ direction (the same with the incident light

polarization). This is consistent with our previous explanation of the field-charge (plasmon) interaction in Chapter 2.

After that, we numerically analyzed the double dipoles (with s=100 nm center-to-center distance). The simulation results of double dipoles show that the field intensity enhancement inside the gap region of dipoles decreases in this case with respect to single dipole. This is explained by the coupling of dipoles. In addition, as can be predicted from the field enhancement result, the tangential field plots of the double dipoles indicate that the surface currents are still in $\pm x$ direction (again the same with the incident light polarization) but with a lower intensity level than the single dipole case.

Furthermore, we analyzed the double C-shaped antenna architecture, which is obtained by connecting the end points of the double dipoles. Our numerical results present that the localized field intensity inside the gap regions does not increase too much and the existed surface current is still in $\pm x$ direction (the same with the incident light polarization) in these C-shaped antenna parts, including the connection part, too.

Finally, we numerically examined the SRR-shaped nanoantenna, which is obtained by simply connecting one gap sides of the double C-shaped antenna. We achieved our aim of enhancing localized field intensity via this architecture. The normalized field intensity enhancement of 4 orders of magnitude is reached at the resonance wavelength of 2160 nm. Also, it is observed that an additional resonance peak arises in our SRR-shaped antenna. When we investigate the tangential field components on each surface, it is found that different from the other cases in SRR-shaped antenna, the resulting surface current on the fundamental resonance (2160 nm) forms a loop. It means that, under x-polarized light, the surface current is along x-direction on the dipole arms and along y-direction on the connection part. We also observed that the same situation holds for the second resonance, i.e., resonance at 930 nm. All these large field

enhancements and the current flow in a loop were expected because we aimed to increase the field enhancement inside the gap region of dipole by connecting their end points, which decreases the radiation from end points and allows for a continuous current flow.

Additionally, we numerically analyzed a similar set of structures, i.e., the double dipoles, the double C-shaped antenna, and the SRR-shaped antenna with *s*=200 nm center-to-center distance. Different field enhancements inside the gap regions and different magnetic field intensities with respect to *s*=100 nm architectures are expectedly observed. However, the modifications in field intensity enhancements and surface currents with the resonator shape antenna are the same as the *s*=100 nm simulations. Again, for SRR-shaped antenna with *s*=200 nm center-to-center distance, we obtain very large field enhancement inside the gap region and the surface current circulates by forming a loop.

Chapter 4

Parametric Studies of Dipole Antennas vs. SRR- and Comb-Shaped Antennas

In the previous chapter, we demonstrated that the field intensity enhancement inside the gap region of a single dipole nanoantenna can be increased extensively by simply connecting end points of it, which yields a resonator shaped nanoantenna. However, the resonance wavelength does not remain constant. The resonance wavelength of the antenna red-shifts considerably with respect to the single dipole, whose lengths in *x*-direction are the same. To have a fair and complete comparison, we should analyze the field enhancements of both antenna architectures that are resonant at the same wavelength. This is necessary because the optical applications operate usually at a constant wavelength or in fixed wavelength spans. For instance, in optical communication systems, fiber optics operating around 1.55 μm wavelength is used because of the minimum loss at this wavelength [50].

To this end, in this chapter we parametrically study the SRR-shaped and single dipole nanoantennas. We compare SRR-shaped and single dipole architectures both among themselves and between each other. This chapter is based in our paper in submission process [51]. Subsequently, we repeat a similar set of simulations and analyses to study the evolution from a dipole to the comb-shaped antenna.

4.1 Dipole Antenna vs. SRR-Shaped Antenna

4.1.1 Method and Geometry

The method and geometry of our simulations in this chapter is very similar to the simulations in the previous chapter. In our analysis, we again focus on the field intensity enhancement inside the gap regions of optical antennas in SRR architecture and single dipole structures but at this time in the spectral range of 400 to 4000 nm. Instead of making simulations over a large spectral range, we divided this spectral range into small pieces. We fit material indices over these small wavelength regions and perform our simulations. By this way, we obtained more accurate simulation results.

Similar to previous simulations, the normalized field intensity enhancement averaged over the gap volume is calculated by using (3.1), which is rewritten in (4.1):

$$field\ enhancement = \frac{1}{V}\int_{V}\left|\frac{E(x,y,z)}{E_{inc}}\right|^{2} dV \qquad (4.1)$$

where V is the gap volume, and $E(x, y, z)$ and E_{inc} are the field inside the gap region and the incident (source) field, respectively. Again, we illuminate the antennas through the substrate with a plane wave polarized along the x-direction.

A part of the computational domain that includes the antenna and some extra volume surrounding the antenna (extended by 100 nm, 100 nm and 25 nm from the antenna in the *x*-, *y*- and *z*-directions, respectively) is meshed uniformly with a mesh size of 2.5 nm. The rest of the computational domain is meshed using a coarser mesh size and the computational domain is truncated with perfectly matched layers.

Again in this chapter, silica (for example, SiO_2 [49]) is used as the dielectric platform because of the same reasons explained in previous chapter. Also, the metal is selected as gold [48] because of its high melting temperature, which is important for not being affected by high field intensity. In addition, the geometrical parameters of the antennas (gap size *g*, metal width *w* and the metal thickness *t*) are still kept constant to avoid an unfair comparison due to the lightning rod effect [13, 21]. The architectures of SRR and single dipole antennas are sketched in Figure 4.1. In our simulations we systematically change the length of the dipole (*d*) and the dimensions of the SRR (*l* and *s*) in *x*- and *y*-directions.

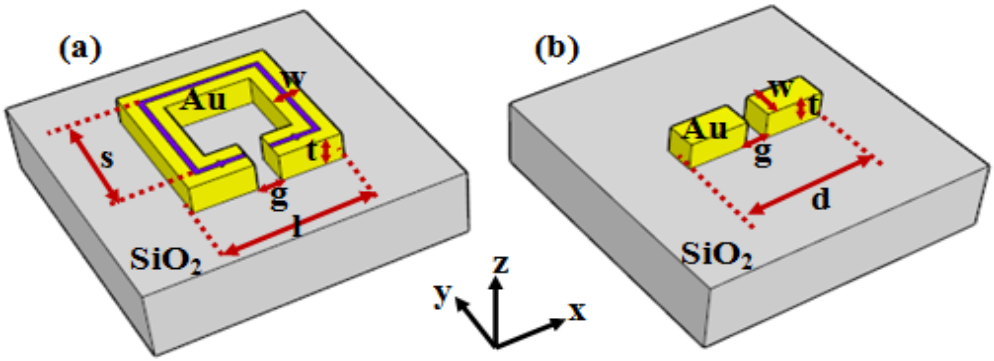

Figure 4.1: Optical antenna architectures based on split ring resonator (SRR) (a) and single dipole structure (b).

4.1.2 Simulation Results and Discussions

We first study the field intensity enhancement behavior of the SRR architecture as a function of antenna dimensions in the *x*- and *y*-directions. We have

performed simulations for l=110, 150, 190 nm and s=50, 60, 80, 100, 120, 140, 160, 180, 200, 220, 240 nm. The minimum sizes (l_{min} and s_{min}) are set to be 110 and 50 nm, respectively, given the constant metal width (w) and the gap length (g). The geometry of a single SRR antenna with l_{min}=110 nm turns into a U-shape and s_{min} is taken to be longer than w (40 nm) to obtain a ring shape. On the other hand, the single dipole antenna with various lengths from 110 to 1110 nm is simulated for comparison purposes. The size in x-direction (d) of the dipole antenna starts from 110 nm. This is again due to the constant w and g of the antennas.

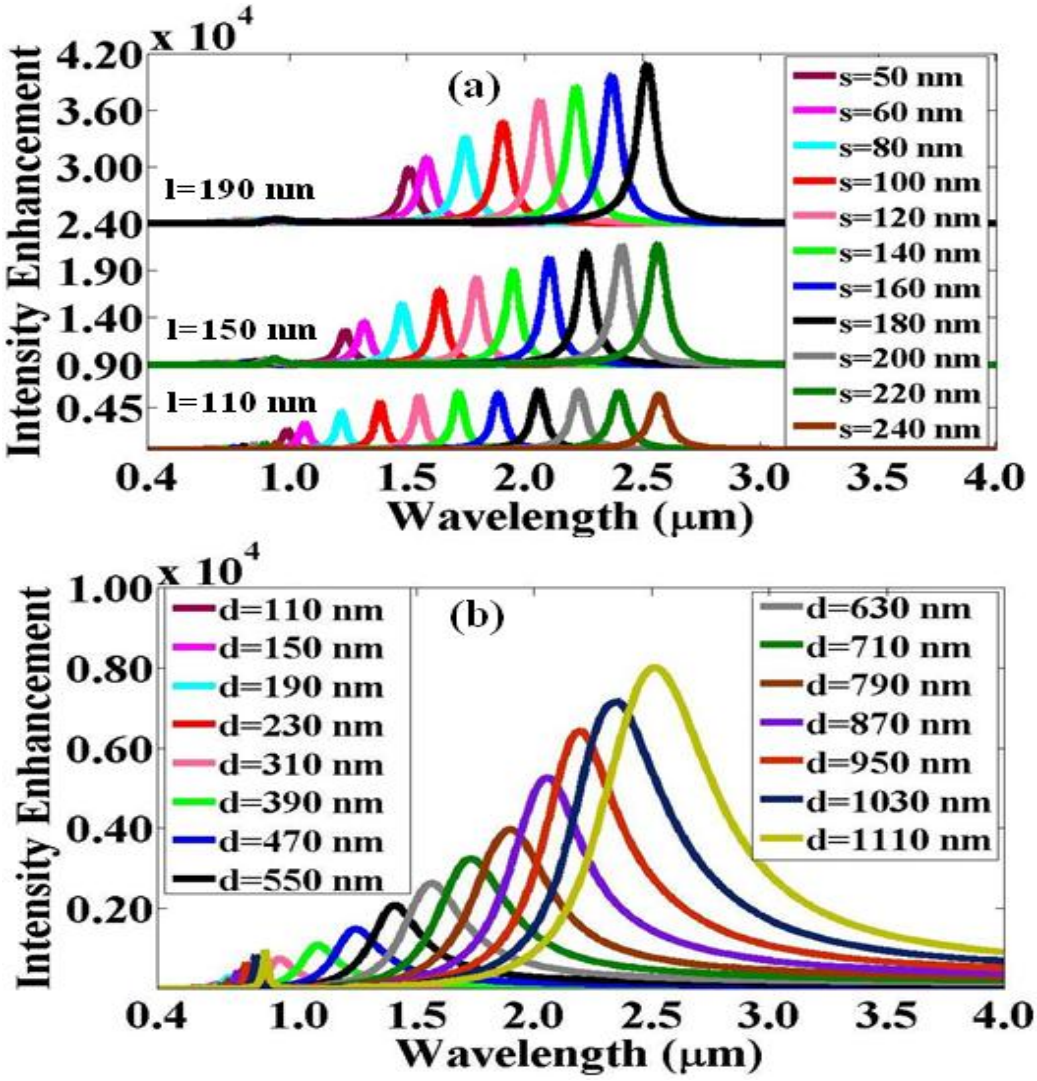

Figure 4.2: Computed field intensity enhancement profiles for the SRR (a) and the dipole (b). In (a) the results of SRR for l=190, 150 and 110 nm are represented starting from the top to the bottom, respectively, with their zero levels shifted for clarity.

In Figure 4.2(a) and (b) the resultant field enhancements inside the gap regions of the SRR and dipole antennas are presented, respectively. Figure 4.2(a) demonstrates that the resonance wavelength red-shifts as the geometry of the antenna enlarges. The tuning of the resonance wavelength with *l* and *s* is depicted in Figure 4.3.

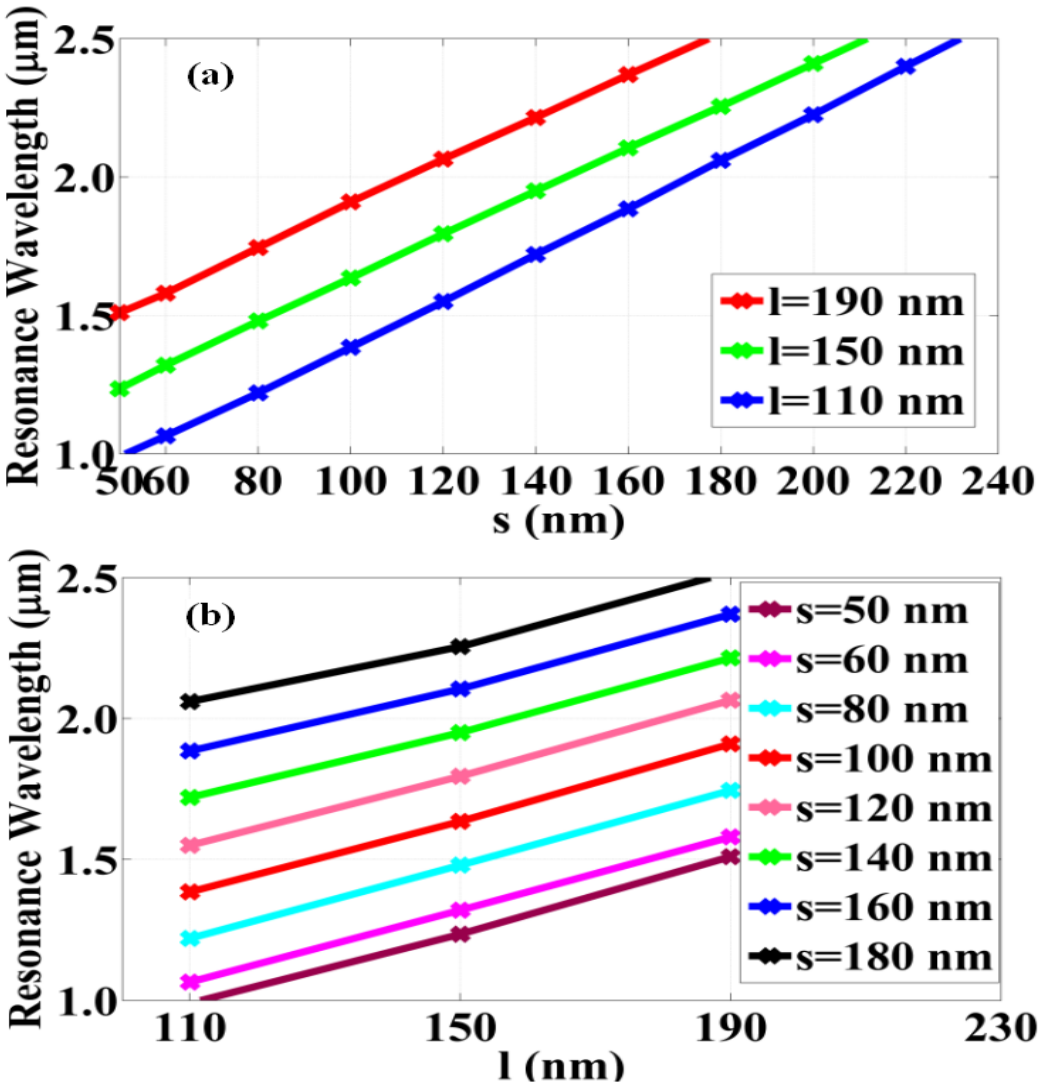

Figure 4.3: Resonance wavelength shift of the SRR antenna (a) with length *s* in *y*-direction and (b) with length *l* in *x*-direction.

Also, Figure 4.2(a) shows that the peak value of the field enhancement for an SRR antenna increases with the size of the antenna both along the *x*- and *y*-

directions. These maximum field enhancement dependencies on *l* and *s* geometrical parameters are shown in Figure 4.4(a).

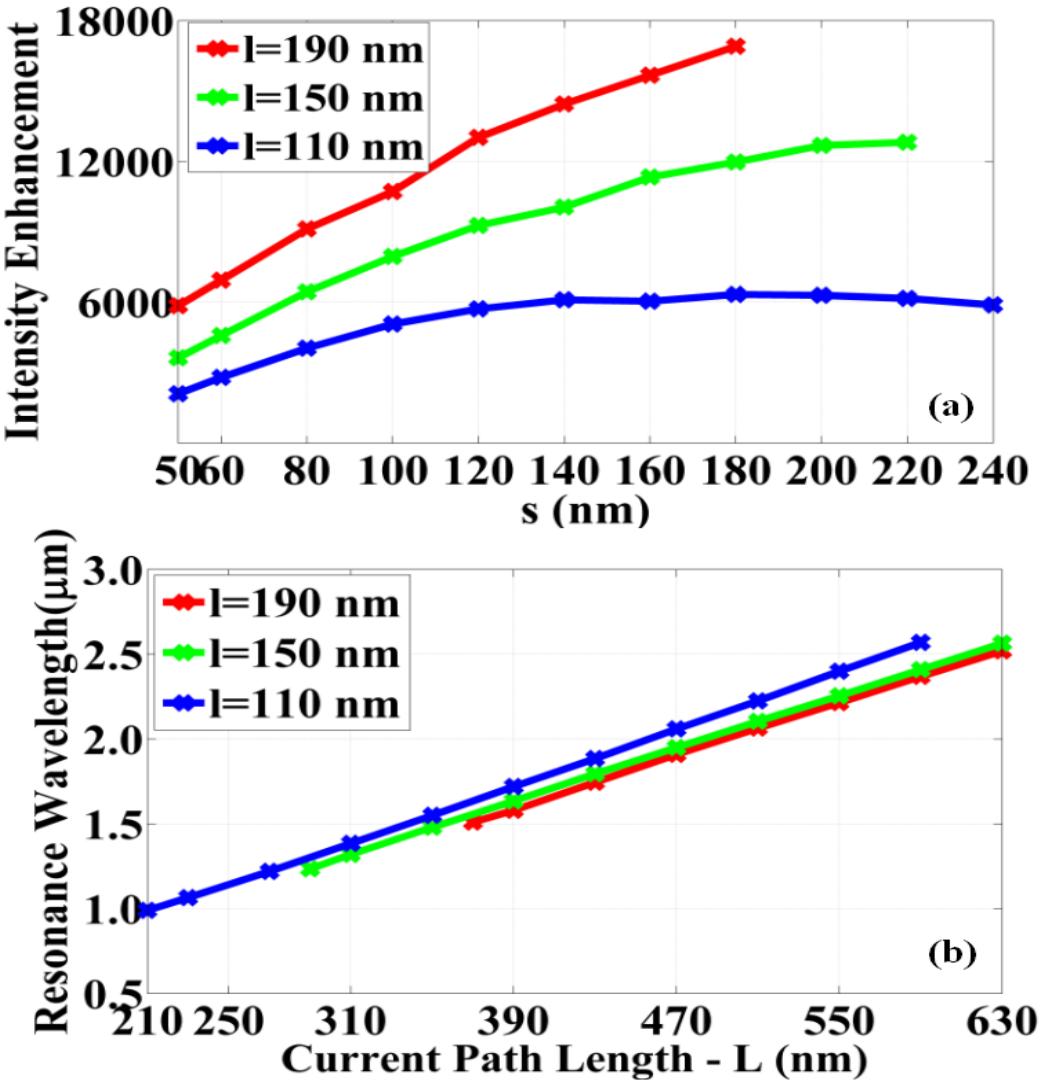

Figure 4.4: (a) Maximum field enhancement dependency on antenna geometries and (b) resonant wavelength shift with the current path length (*L*) in the SRR antenna architecture.

Considering the current path length in the resonator antenna (represented with purple arrow in Figure 4.1(a)) for the resonance wavelength shift would be more meaningful for comparison with the dipole simulation results. The averaged current path length, *L*, in the SRR is calculated by using (4.2)

$$L=(l-w-g)+(l-w)+2s \tag{4.2}$$

Since the metal width and gap length are constant (w=40 nm, g=30 nm), (4.2) turns into (4.3).

$$L = 2(l + s) - 110\,nm \tag{4.3}$$

Figure 4.4(b) illustrates the shift of the resonance wavelength with the current path length for our SRR antennas.

Computational results show that the resonance wavelength increases almost linearly with the current path length for all cases (*i.e.*, for l=110, 150 and 190 nm) (Figure 4.4(b)). However, the resonance wavelength is shorter for horizontally large resonator antennas than horizontally small resonator antennas, which have the same current path lengths. Such different linear behavior for different geometries can be explained by the fact that the electrons in the metal parts of an antenna act with the effective wavelength, which depends on the geometry and the incident wavelength through a scaling rule [52, 53] of

$$\lambda_{eff} = n_1 + n_2\left(\frac{\lambda}{\lambda_p}\right) \tag{4.4}$$

where λ and λ_p are the incident and plasma wavelengths, respectively, and n_1 and n_2 are constants that depend on the antenna geometry.

For comparison purposes, we also study a single dipole antenna with various lengths. The intensity enhancement values for 15 different dipole lengths are calculated, as presented in Figure 4.2(b). We observe that the peak value of the field enhancement scales up with the length of the dipole in a similar fashion with that of an SRR antenna (Figure 4.5(a)). In addition, it is deduced from Figure 4.2(b) that the resonance wavelength increases linearly with the dipole length, as depicted in Figure 4.5(b). This linear shift is expectedly compatible with the scaling rule (4.4). However, Figure 4.4(b) and Figure 4.5(b) show that the resonance wavelength of a single dipole antenna is shorter than that of a single SRR antenna, even though the dipole antenna length and the SRR current path length are the same.

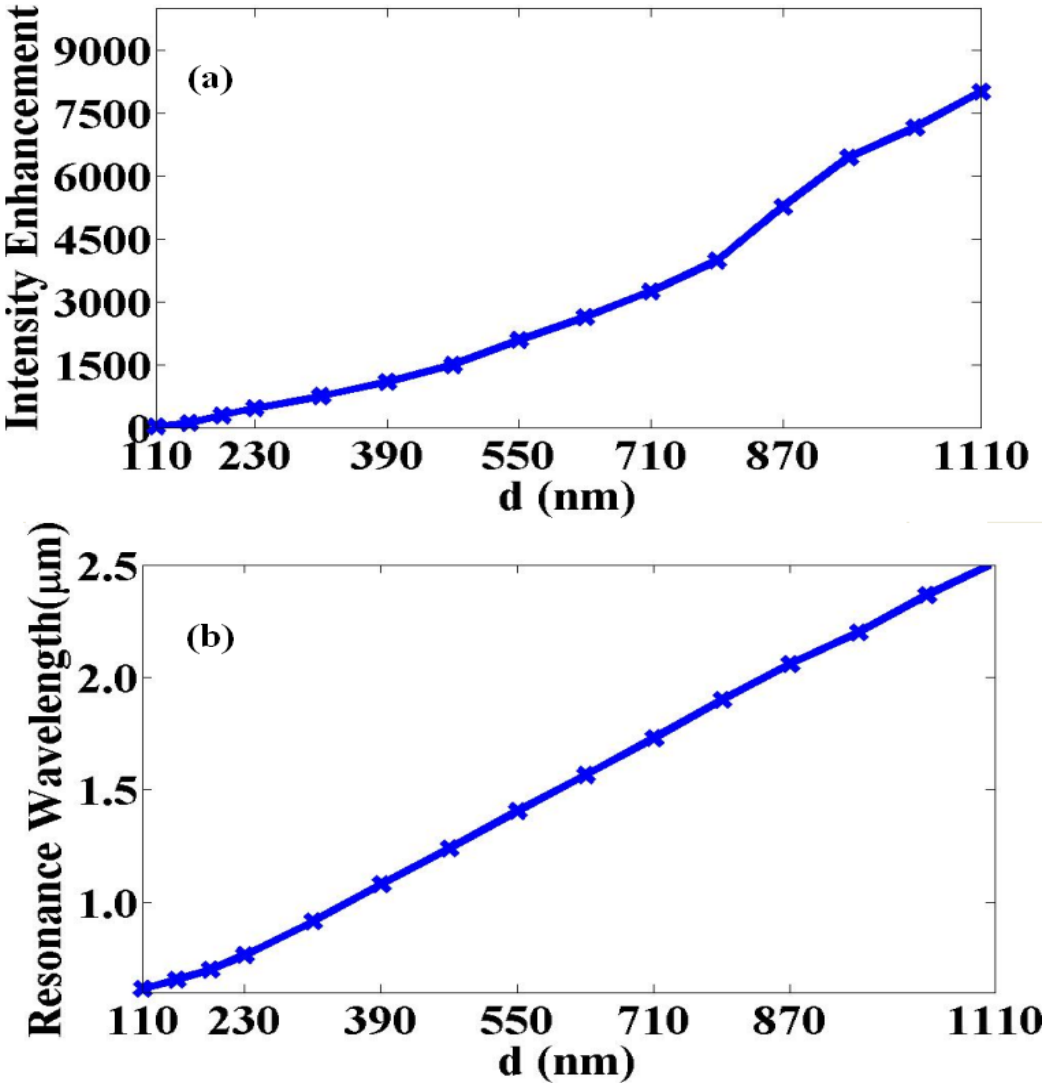

Figure 4.5: (a) Maximum field enhancement level and (b) resonance wavelength shift as a function of the dipole antenna length *d*.

Furthermore, the maximum field enhancements of the SRR and dipole antennas are given as a function of their resonance wavelengths in Figure 4.6. The black dotted line in this figure indicates the optimum field enhancements using our SRR designs with different lengths in the *x*-direction (*l*). The ratio of this field enhancement for the optimum SRR designs to that for the dipole antenna (represented with blue line in Figure 4.6) is calculated and shown as the improvement factor in Figure 4.7. This demonstrates that the resonance field

intensity enhancement of a single dipole nanoantenna can be increased more than two folds with a single SRR nanoantenna.

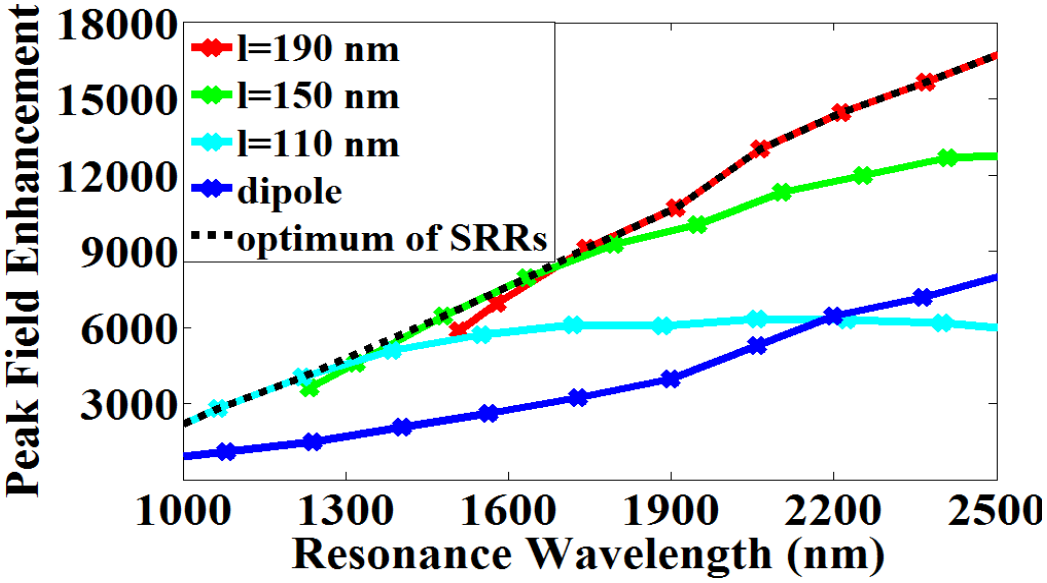

Figure 4.6: Maximum field enhancement *vs.* resonance wavelength for single dipole and SRR antennas.

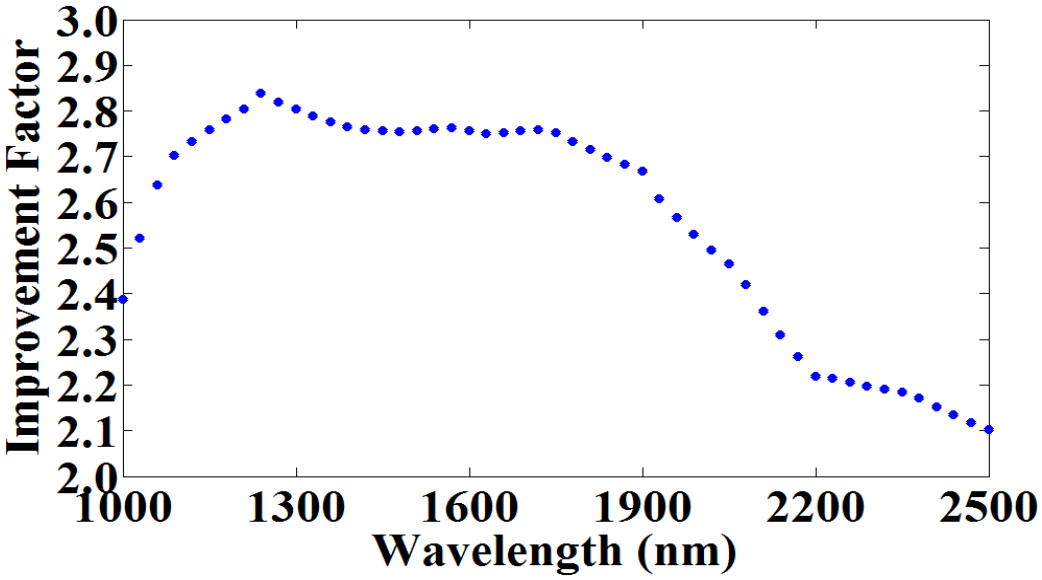

Figure 4.7: Improvement factor *vs.* wavelength for our SRR antenna with respect to single dipole antenna.

4.1.3 Conclusion

In this section, we parametrically studied planar optical antennas based on split ring resonators that outperform dipole antennas for localized field intensity inside the gap region. We numerically demonstrated that the field intensity localization of a dipole antenna can be at least doubled using the SRR architecture with the same gap size. In addition, we showed that the resonance wavelength of the SRR antenna exhibits a linear dependency on the antenna dimensions as the dipole. Also, we presented the peak value of the field enhancement contingent upon the antenna size in the SRR designs. We believe that this simple design strategy of resonator antennas can be beneficial for current and future optical antenna applications that call for increased field localization.

4.2 Various Antenna Architectures from a Single Dipole to Comb-Shaped Antenna

In the previous section, we have already examined optical antennas of split ring resonator evolved from dipole architectures. It is proved that the large field enhancements are achieved with a simple connection, which allows continuous current flow. Based on a similar idea, we work on different antenna structures derived from SRR shape such as comb-shaped architecture in optical antennas, which has been previously studied in RF antennas by our group [28]. We expect to observe advanced field localization inside the gap regions in the comb case compared to those of single and array of dipoles.

For this purpose, in this section we analyze various shaped optical antennas. We start our analyses from the beginning of all our simulations, which is a single dipole antenna, and continue with other structures derived from that such as SRR shape and array of dipoles. We extend our examination to comb-shaped architectures having different teeth number and some other variants. Here, we represent all these antenna simulations step by step and at the end compare them. Part of this section was presented in a conference [54] and will be submitted soon.

4.2.1 Method and Geometry

The method and geometry of antenna simulations in this section are the same with that of simulations in the previous chapter, except for one little change. Here, we are interested in the field enhancements inside the gap regions over a wide wavelength regime spanning from 400 to 7000 nm. The field intensity

enhancement with respect to the incident field intensity averaged over the gap volume is calculated by using (5.1), which is the same with (3.1) and (4.1).

$$field\ enhancement = \frac{1}{V}\int_{V}\left|\frac{E(x,y,z)}{E_{inc}}\right|^{2} dV \qquad (5.1)$$

where V is the gap volume, and $E(x, y, z)$ and E_{inc} are the field inside the gap region and the incident (source) field, respectively.

Also, in our simulations antennas are meshed uniformly with a 2.5 nm mesh size and all the boundaries in *x*, *y* and *z*-directions are set perfectly matched. In addition, in our designs all the antennas have constant parameters to prevent unfair comparisons due to lightning rod effect [13, 21], i.e., 40 nm metal width, 40 nm metal thickness, 30 nm gap length, 230 nm dipole or teeth lengths. Moreover, we illuminate all the antennas from substrate side with a plane wave polarized along the *x*-direction.

The only difference between the simulations in this section and the simulations in the third chapter is the material indices fitting. Although in both sets of simulations we used Au [48] and SiO_2 [49] as our metal and substrate, respectively, we fit material indices better (with more fitting parameters) in this section than Chapter 3. This is the reason of why field enhancement peak values differ slightly. The architecture of a single connected comb antenna with 2 teeth investigated in this section is sketched in Figure 4.8 as an example.

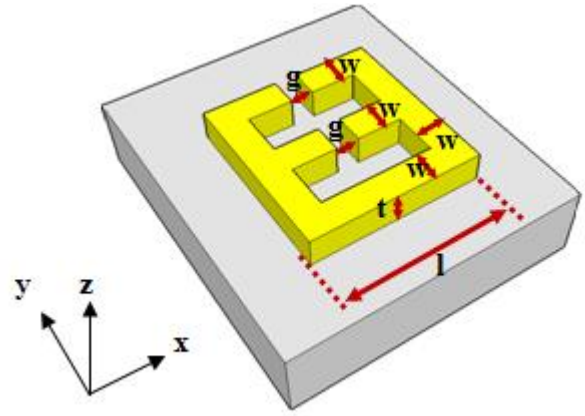

Figure 4.8: Architecture of single connected comb antenna with 2 teeth.

Since we have a constant gap size (g), metal thickness (t), metal width (w) and dipole or teeth length (l), we will not present these parameters again in the following antenna structures. Also, since we are dealing with the peak field enhancements on resonance and the resonance wavelengths, we will tabulate these data for each gap size of each antenna structures.

4.2.2 Simulation Results and Discussions

Our antenna structures and their tabulated simulation results starting from a single dipole to the comb shape are given step by step in a full list below for the sake of completeness. The first seven set of simulations are the same with the simulations in the third chapter and the previous section. Thus, we had identical results. Here are our observations. First, the field localization inside the gap region of a dipole antenna can be increased enormously by connecting its end points and obtaining a SRR-shaped antenna. This SRR-shaped nanoantennna red-shifts the resonance wavelength and yields additional resonances at shorter wavelengths. In addition, it is observed that enlarging the geometry of resonator antenna effects the field enhancement and the resonance wavelength. The resonance wavelength increases as the antenna enlarges, which is examined deeply in the previous section.

- **Single dipole:**

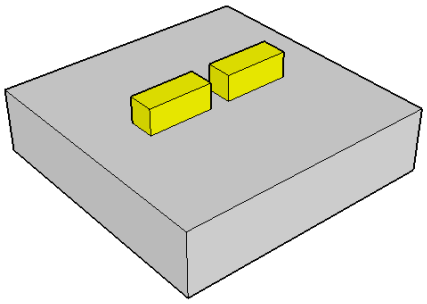

Figure 4.9: Single dipole antenna geometry.

	Inside the gap region
Single peak	455 at 765 nm

Table 4.1: Peak field enhancement and resonance wavelength inside the gap region of the single dipole antenna.

- Double dipoles (with s=100 nm center-to-center distance):

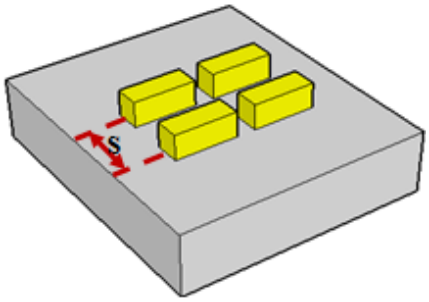

Figure 4.10: Double dipoles with s=100 nm center-to-center distance.

	Inside both gap regions
Single peak	171 at 780 nm

Table 4.2: Peak field enhancement and resonance wavelength inside the gap regions of the double dipole antennas (with s=100 nm).

- Double C-shapes (with s=100 nm center-to-center distance):

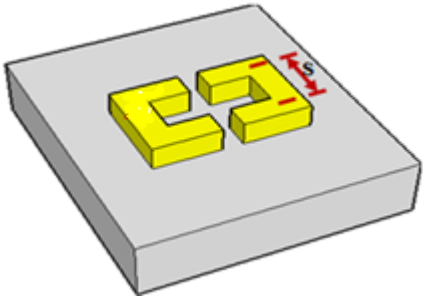

Figure 4.11: Double C-shape antenna structure (with s=100 nm center-to-center distance).

	Inside both gap regions
Single peak	188 at 795 nm

Table 4.3: Peak field enhancement and resonance wavelength inside the gap regions of the double C-shape antenna (with s=100 nm).

- SRR shape (with s=100 nm center-to-center distance):

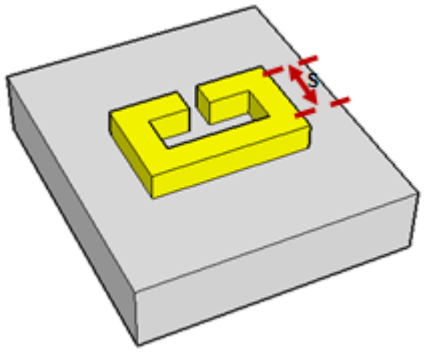

Figure 4.12: SRR shape antenna structure (with s=100 nm center-to-center distance).

	Inside the gap region
1st peak	68 at 685 nm
2nd peak	418 at 935 nm
3rd peak	14,893 at 2160 nm

Table 4.4: Peak field enhancements and resonance wavelengths inside the gap region of the SRR shape antenna (with s=100 nm).

- Double dipoles (with s=200 nm center-to-center distance):

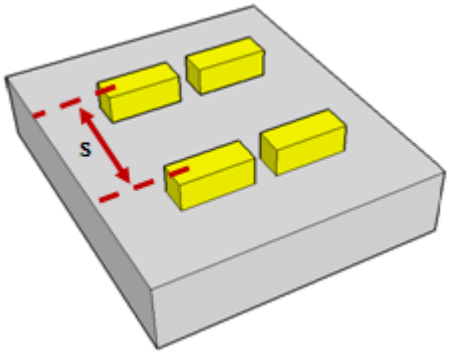

Figure 4.13: Double dipoles with s=200 nm center-to-center distance.

	Inside both gap regions
Single peak	231 at 755 nm

Table 4.5: Peak field enhancement and resonance wavelength inside the gap regions of the double dipole antennas (with s=200 nm).

- Double C-shapes (with s=200 nm center-to-center distance):

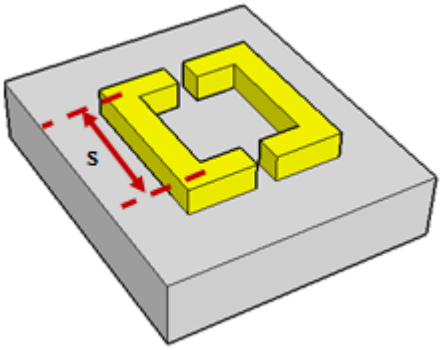

Figure 4.14: Double C-shape antenna structure (with s=200 nm center-to-center distance).

	Inside both gap regions
1st peak	34 at 655 nm
2nd peak	460 at 870 nm

Table 4.6: Peak field enhancements and resonance wavelengths inside the gap regions of the double C-shape antenna (with s=200 nm).

- SRR shape (with s=200 nm center-to-center distance):

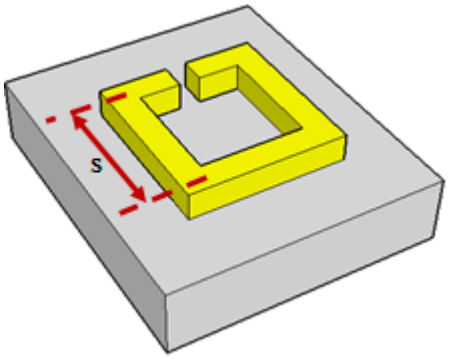

Figure 4.15: SRR shape antenna structure (with s=200 nm center-to-center distance).

	Inside the gap region
1st peak	56 at 665 nm
2nd peak	116 at 775 nm
3rd peak	681 at 1080 nm
4th peak	20,795 at 2900 nm

Table 4.7: Peak field enhancements and resonance wavelengths inside the gap region of the SRR shape antenna (with s=200 nm).

- Triple dipoles (with s=100 nm center-to-center distances):

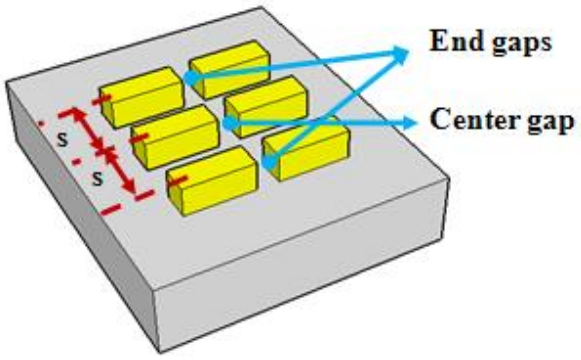

Figure 4.16: Triple dipoles with s=100 nm center-to-center distances.

	Inside the end gaps	Inside the center gap
1st peak	300 at 750 nm	47 at 720 nm
2nd peak	X	200 at 765 nm

Table 4.8: Peak field enhancements and resonance wavelengths inside the gap regions of the triple dipoles antenna (with s=100 nm).

- Double E-shapes (with s=100 nm center-to-center distances):

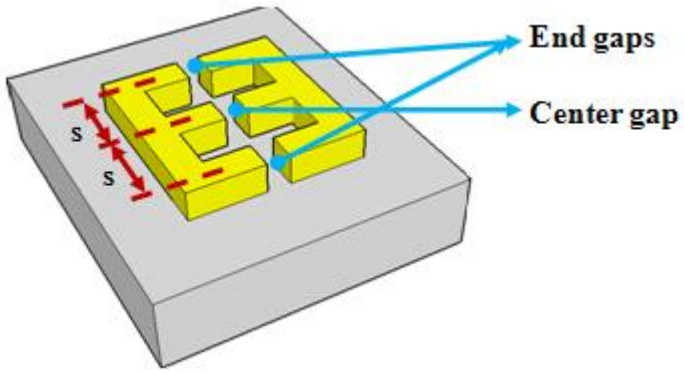

Figure 4.17: Double E-shape antenna structure (with s=100 nm center-to-center distance).

	Inside the end gaps	Inside the center gap
1st peak	121 at 805 nm	112 at 795 nm
2nd peak	100 at 1100 nm	143 at 1135 nm

Table 4.9: Peak field enhancements and resonance wavelengths inside the gap regions of the double E-shape antenna (with s=100 nm).

- Single connected double E-shapes (Connected comb geometry with 2 teeth) (with s=100 nm center-to-center distances):

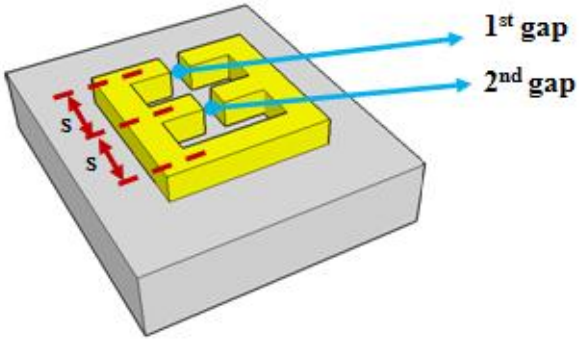

Figure 4.18: Single connected double E-shape antenna structure (with s=100 nm center-to-center distances).

	Inside the 1st gap	Inside the 2nd gap
1st peak	208 at 750 nm	48 at 735 nm
2nd peak	1,984 at 1220 nm	3,172 at 1210 nm
3rd peak	16,020 at 3060 nm	8,079 at 3060 nm

Table 4.10: Peak field enhancements and resonance wavelengths inside the gap regions of the single connected double E-shape antenna (with s=100 nm).

- Double connected double E-shapes with a single gap at the end (with s=100 nm center-to-center distances):

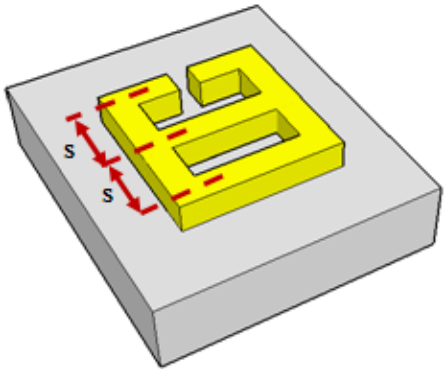

Figure 4.19: Double connected double E-shape antenna structure with a single gap at the end (with s=100 nm center-to-center distance).

	Inside the gap region
1st peak	192 at 760 nm
2nd peak	290 at 1080 nm
3rd peak	13,823 at 2050 nm

Table 4.11: Peak field enhancements and resonance wavelengths inside the gap region of the double connected double E-shape antenna with a single gap at the end (with s=100 nm).

- Double connected double E-shape with a single gap at the center (with s=100 nm center-to-center distances):

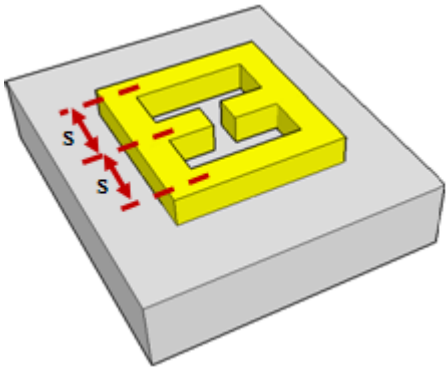

Figure 4.20: Double connected double E-shape antenna structure with a single gap at the center (with s=100 nm center-to-center distances).

	Inside the gap region
1st peak	11 at 640 nm
2nd peak	630 at 980 nm
3rd peak	6,834 at 1600 nm

Table 4.12: Peak field enhancements and resonance wavelengths inside the gap region of the double connected double E-shape antenna with a single gap at the center (with s=100 nm).

- Triple dipoles (with s=200 nm center-to-center distances):

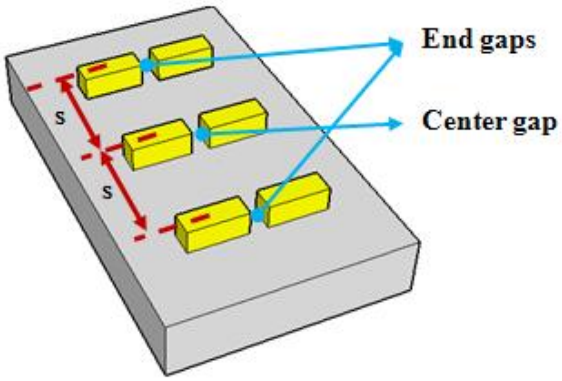

Figure 4.21: Triple dipoles with s=200 nm center-to-center distances.

	Inside the end gaps	Inside the center gap
1st peak	460 at 775 nm	246 at 735 nm
2nd peak	N/A	91 at 830 nm

Table 4.13: Peak field enhancements and resonance wavelengths inside the gap regions of the triple dipoles antenna (with s=200 nm).

- Double E-shapes (with s=200 nm center-to-center distances):

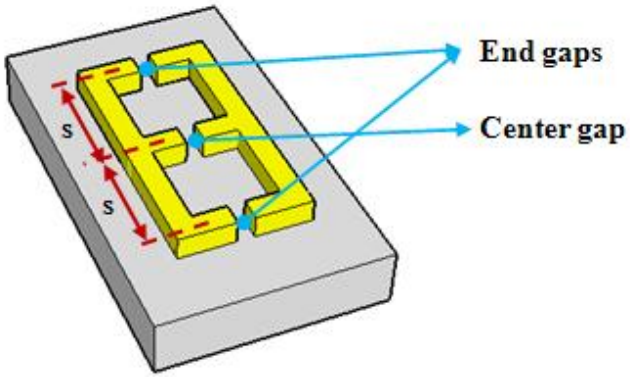

Figure 4.22: Double E-shape antenna structure (with s=200 nm center-to-center distances).

	Inside the end gaps	Inside the center gap
1st peak	154 at 715 nm	746 at 860 nm
2nd peak	217 at 880 nm	318 at 1415 nm
3rd peak	165 at 1450 nm	N/A

Table 4.14: Peak field enhancements and resonance wavelengths inside the gap regions of the double E-shape antenna (with s=200 nm).

- Single connected double E-shapes (Connected comb geometry with 2 teeth) (with s=200 nm center-to-center distances):

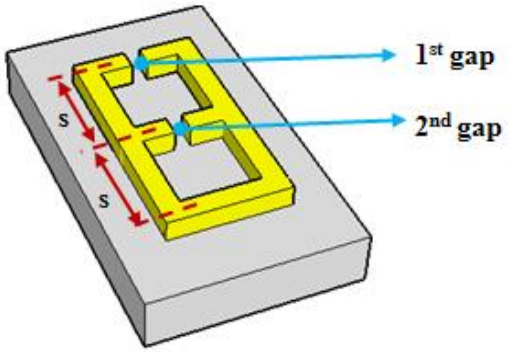

Figure 4.23: Single connected double E-shape antenna structure (with s=200 nm center-to-center distances).

	Inside the 1st gap	Inside the 2nd gap
1st peak	58 at 755 nm	469 at 855 nm
2nd peak	494 at 875 nm	726 at 1085 nm
3rd peak	4,782 at 1645 nm	6,087 at 1640 nm
4th peak	15,666 at 4435 nm	7,557 at 4435 nm

Table 4.15: Peak field enhancements and resonance wavelengths inside the gap regions of the single connected double E-shape antenna (with s=200 nm).

- Double connected double E-shapes with a single gap at the end (with s=200 nm center-to-center distances):

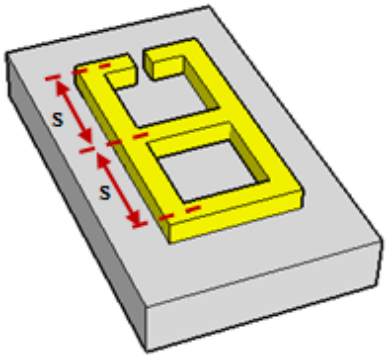

Figure 4.24: Double connected double E-shape antenna structure with a single gap at the end (with s=200 nm center-to-center distances).

	Inside the gap region
1st peak	360 at 770 nm
2nd peak	264 at 945 nm
3rd peak	377 at 1325 nm
4th peak	22,726 at 2825 nm

Table 4.16: Peak field enhancements and resonance wavelengths inside the gap region of the double connected double E-shape antenna with a single gap at the end (with s=200 nm).

- Double connected double E-shape with a single gap at the center (with s=200 nm center-to-center distances):

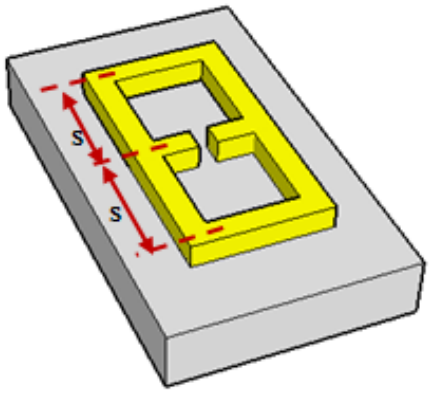

Figure 4.25: Double connected double E-shape antenna structure with a single gap at the center (with s=200 nm center-to-center distance).

	Inside the gap region
1st peak	15 at 625 nm
2nd peak	20 at 765 nm
3rd peak	1,142 at 1035 nm
4th peak	18,258 at 2220 nm

Table 4.17: Peak field enhancements and resonance wavelengths inside the gap region of the double connected double E-shape antenna with a single gap at the center (with s=200 nm).

- Connected comb geometry with 3 teeth (with s=100 nm center-to-center distances):

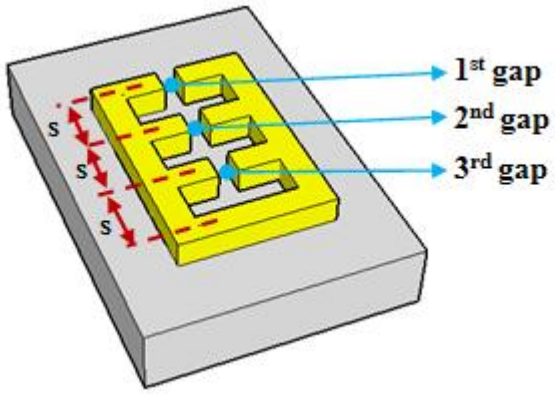

Figure 4.26: Connected comb antenna geometry with 3 teeth (with s=100 nm center-to-center distances).

	Inside the 1st gap	Inside the 2nd gap	Inside the 3rd gap
1st peak	187 at 780 nm	95 at 775 nm	964 at 1095 nm
2nd peak	472 at 1100 nm	2,266 at 1105 nm	4,243 at 1480 nm
3rd peak	2,808 at 1485 nm	457 at 1470 nm	4,020 at 3935 nm
4th peak	13,200 at 3935 nm	9,281 at 3935 nm	N/A

Table 4.18: Peak field enhancements and resonance wavelengths inside the gap regions of the connected comb shaped antenna with 3 teeth (with s=100 nm).

- Connected comb geometry with 4 teeth (with s=100 nm center-to-center distances):

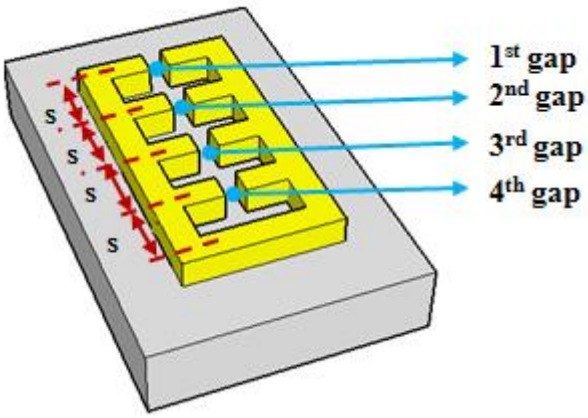

Figure 4.27: Connected comb antenna geometry with 4 teeth (with s=100 nm center-to-center distances).

	Inside the 1st gap	**Inside the 2nd gap**	**Inside the 3rd gap**	**Inside the 4th gap**
1st peak	22 at 650 nm	113 at 775 nm	56 at 715 nm	20 at 650 nm
2nd peak	198 at 760 nm	667 at 1070 nm	43 at 800 nm	19 at 705 nm
3rd peak	197 at 1080 nm	1,482 at 1230 nm	742 at 1075 nm	480 at 1060 nm
4th peak	942 at 1225 nm	106 at 1785 nm	897 at 1235 nm	1,607 at 1225 nm
5th peak	3,293 at 1765 nm	8,109 at 4765 nm	2,535 at 1755 nm	4,125 at 1760 nm
6th peak	10,103 at 4765 nm	N/A	5,086 at 4765 nm	2,060 at 4765 nm

Table 4.19: Peak field enhancements and resonance wavelengths inside the gap regions of the connected comb-shaped antenna with 4 teeth (with s=100 nm).

The results of triple dipoles tabulated in Table 4.8 and Table 4.13 indicate that the field localization inside the gap regions of the triple dipoles is different than that of single and double dipoles. This is again because of coupling of the dipole antennas, but this time 3 dipoles interact with each other. In addition, Table 4.9 and Table 4.14 present that connecting end points of the dipoles changes the peak values of the field enhancement and the resulting resonance wavelengths so much that the triple dipoles turns into a totally different antenna as a whole. However, the peak field enhancement does not show an increasing trend in the E-shape antennas.

On the other hand, if we tie one of dipole`s arm and obtain a connected comb geometry with 2 teeth, as going from Figure 4.18 to Figure 4.23, the field intensity enhancement inside both gaps increases from the level of hundreds to the level of thousands. Also, the resonance wavelength of the connected comb-shaped antenna is red-shifted with respect to the single and array of dipoles with the same arm lengths. In addition, one of the interesting observations is that the peak field enhancements inside the gaps of connected comb antenna are achieved at the same resonance wavelength. It means that our connected comb antenna behaves as a single antenna as a whole.

Moreover, when we connect one more dipole and obtain antenna structures as in Figure 4.19 (or Figure 4.20) and Figure 4.24 (or Figure 4.25) we have field enhancements inside the gap region with 3 to 4 orders of magnitude. However, these field enhancements around similar resonance wavelengths are achieved with SRR antenna structures. Therefore, the double connected double E-shapes with a single gap are not superior to our SRR design. They indeed occupy more area than SRR.

Consequently, the connected comb antenna architectures provide larger field enhancements inside their gap regions than those of the single and array of dipoles with the same teeth number and length. To observe modifications on the field localization properties, we also analyze single connected comb shape antennas with more teeth from Figure 4.26 to Figure 4.27.

The comparison of the simulated data given in Table 4.10, Table 4.18 and Table 4.19 indicates that the peak field enhancements inside the gap regions of the connected comb-shaped antenna does not show further enhancement as opposed to our expectations. The field enhancements averaged over the gap regions still have 3 to 4 orders of magnitude. However, it can be useful that the resonance wavelengths of the connected comb-shaped nanoantennas red-shift and additional resonances come out at shorter wavelengths as we increase the number of teeth.

4.2.3 Conclusion

In conclusion, in this section we numerically studied and demonstrated the resonance behavior of various shaped optical nanoantennas starting from a single dipole to connected comb shapes. Our initial simulations in this section prove some results of the previous chapter and the previous section. For

instance, the peak field intensity enhancement of the dipole antenna can be enhanced largely with a SRR-shaped antenna but at longer wavelengths and the resonance wavelength of SRR-antenna red-shifts as we enlarge it.

Furthermore, in this section we showed that comb nanoantennas resonate at longer wavelengths and the total field intensity enhancement on resonance is larger in the comb architecture than those in the dipole cases using the same lengths. Localizing near-infrared and mid-infrared light within a region of tens of nanometers can be achieved at an intensity enhancement level up to 4 orders of magnitude by these comb structures. In addition, in comb-shaped nanoantennas, as a result of adding comb teeth, main resonance red-shifts and additional resonances emerge at shorter wavelengths. We believe that such comb-shaped optical antennas are promising for applications that require intense optical spots beyond the diffraction limit in the infrared.

Chapter 5

Conclusions

In this thesis work, we proposed and demonstrated novel optical antennas inspired by metamaterial architectures with the aim of increasing the field intensity enhancement of localized light obtained by the antenna. Although in the literature different types of optical antennas have been widely investigated to date, they are either hard to fabricate or lack maximum field enhancement. To overcome both deficiencies, we present split ring resonator and connected comb shaped nanoantennas and compare their simulation results with those of the single and array dipoles.

In this thesis, we reviewed the fundamentals of plasmonics. We shortly described the history of plasmons and explained the basics of surface plasmon polaritons and localized surface plasmons. We also presented an overview of the plasmonics in optical antennas and briefly discussed the finite-difference time-domain (FDTD) method and simulation tool, Lumerical.

In our work, we first demonstrated that the localized field intensity enhancement of a dipole antenna is increased from the level of hundreds to the level of ten thousands by simply connecting its end points and obtaining a SRR-shaped antenna. This was an expected result because our design idea of a resonator antenna relies on decreasing the field radiations from end points of the dipole by connecting them and allowing for a continuous current flow. To observe this surface current-field enhancement relation, we analyzed the surface currents on optical antennas starting from a dipole to a SRR shape evolved step by step. In these analyses, it is observed that under the incident light of polarization along *x*-direction (the same with the dipole orientation) the resulting surface currents on resonance are along the same (*x*) direction, but in the SRR antenna they are not along *x*-direction. Instead, in SRR, the surface currents on resonance follow a continuous path that forms a loop.

In addition, we parametrically studied the SRR-shaped and single dipole nanoantennas. Since the resonance wavelength of a dipole nanoantenna considerably shifts during the construction of a SRR nanoantenna, to have fair comparison we systematically changed the dimensions of the SRR and dipole antennas in our simulations. Our results demonstrate that the peak value of the field enhancement and the resonance wavelength depend on the antenna size in the SRR-shaped nanoantenna. It is shown that the resonance wavelength changes linearly with the resonator dimensions both in *x*- and *y*- directions. Also, as one of the most important remarks, it is concluded from the peak intensity and resonance wavelength data that the field intensity enhancement of the dipole antenna can be increased more than 2-folds by using a SRR-shaped antenna with the same gap size and arranged geometry at the same resonance wavelength.

Furthermore, we worked on variants of optical antennas derived from the SRR-shaped antenna such as the comb architectures. Our simulations demonstrate that the connected comb shape antenna resonates at much longer

wavelengths than the dipoles, whose respective teeth and arm lengths are the same. Also, it is found that the total field intensity enhancements obtained inside the gap regions of the connected comb antenna structure is larger than those of single and array dipoles again with the same arm lengths. These two consequences indicate that the light in mid- and near-infrared can be localized inside the gap region of tens of nanometers by the connected comb antenna architecture with a field intensity enhancement on the four orders of magnitude, which can be achieved only by very long antennas in the dipole architecture. In addition, our simulations of the connected comb antennas with various numbers of teeth show that the main resonance of antenna red-shifts and new resonances emerge at shorter wavelengths if we add more teeth.

We believe that SRR and connected comb shaped antennas can be favorable to use in future optical antenna applications that require intense optical spots. We also think that, based on their simple geometry, these antenna structures are open to further advancements. The future steps of this thesis work include experimental fabrication and characterization of some of the antenna designs presented in this thesis.

BIBLIOGRAPHY

[1] B. E. A Saleh and M. C. Teich, *Fundamentals of Photonics*., Wiley, 1991.

[2] A. S. van de Nes, J. J. M. Braat and S. F. Pereira, "High-density optical data storage," *Rep. Prog. Phys.* **69**, pp.2323-2363 (2006).

[3] S. A. Maier, *Plasmonics: Fundamentals and Applications.*, Springer, 2007.

[4] M. L. Brongersma and P. G. Kik, *Surface Plasmon Nanophotonics.*, Springer, 2007.

[5] H. Raether, *Surface Plasmons on Smooth and Rough Surfaces and on Gratings.*, Springer-Verlag, 1988.

[6] K. Gramotnev and S. I. Bozhevolnyi, "Plasmonics beyond the diffraction limit," *Nat. Photonics* **4**, pp.83-91 (2010).

[7] V. M. Shalaev and S. Kawata, *Nanophotonics with Surface Plasmons.*, Elseiver, 2007.

[8] L. Novotny and N. van Hulst, "Antennas for light," *Nat. Photonics* **5**, pp.83-90 (2011).

[9] K. B. Crozier, A. Sundaramurthy, G. S. Kino, and C. F. Quate, "Optical antennas: Resonators for local field enhancement," *J. Appl. Phys.* **94**, pp.4632-4642 (2003).

[10] H. Fischer and O. J. F. Martin, "Engineering the optical response of plasmonic nanoantennas," *Opt. Express* **16,** pp.9144-9154 (2008).

[11] P. Muhlschlegel, H.-J. Eisler, O. J. F. Martin, B. Hecht, and D. W. Pohl, "Resonant Optical Antennas," *Science* **308**, pp.1607-1609 (2005).

[12] J. Merlein, M. Kahl, A. Zuschlag, A. Sell, A. Halm, J. Boneberg, P. Leiderer, A. Leitenstorfer and R. Bratschitsch, "Nanomechanical control of an optical antenna," *Nat. Photonics* **2**, pp.230-233 (2008).

[13] D. P. Fromm, A. Sundaramurthy, P. J. Schuck, G. Kino, and W. E. Moerner, "Gap-Dependent Optical Coupling of Single "Bowtie" Nanoantennas Resonant in the Visible," *Nano Lett.* **4**, pp.957-961 (2004).

[14] M. D. Wissert, A. W. Schell, K. S. Ilin, M. Siegel, and H.-J. Eisler, "Nanoengineering and characterization of gold dipole nanoantennas with enhanced integrated scattering properties," *Nanotechnology* **20**, 425203 (2009).

[15] E. Cubukcu, E. A. Kort, K. B. Crozier, and F. Capasso, "Plasmonic Laser Antenna," *Appl. Phys. Lett.* **89**, pp.093120 (2006).

[16] A. Sundaramurthy, K. B. Crozier, G. S. Kino, D. P. Fromm, P. J. Schuck, and W. E. Moerner, "Field enhancement and gap-dependent resonance in a system of two opposing tip-to-tip Au nanotriangles," *Phys. Rev. B* **72**, pp.165409 (2005).

[17] P. J. Schuck, D. P. Fromm, A. Sundaramurthy, G. S. Kino, and W. E. Moerner, "Improving the Mismatch between Light and Nanoscale Objects with Gold Bowtie Nanoantennas," *Phys. Rev. Lett.* **94**, pp.017402 (2005).

[18] W. Zhang, L. Huang, C. Santschi, and O. J. F. Martin, "Trapping and Sensing 10 nm Metal Nanoparticles Using Plasmonic Dipole Antennas," *Nano Lett.* **10**, pp.1006-1011 (2010).

[19] H. Tamaru, H. Kuwata, H. T. Miyazaki, and K. Miyano, "Resonant light scattering from individual Ag nanoparicles and particle pairs," *Appl. Phys. Lett.* **80**, pp.1826-1828 (2002).

[20] L. Rogobete, F. Kaminski, M. Agio, and V. Sandoghdar, "Design of plasmonic nanoantennae for enhancing spontaneous emission," *Opt. Lett.* **32**, pp.1623-1625 (2007).

[21] Y. C. Martin, H. F. Hamann, and H. K. Wickramasinghe, "Strength of the electric field in apertureless near-field optical microscopy," *J. Appl. Phys.* **89**, pp.5774-5778 (2001).

[22] R. M. Bakker, A. Boltasseva, Z. Liu, R. H. Pedersen, S. Gresillon, A. V. Kildishev, V. P. Drachev, and V. M. Shalaev, "Near-field excitation of nanoantenna resonance," *Opt. Express* **15**, pp.13682-13688 (2007).

[23] J. Yang, J. Zhang, X. Wu, and Q. Gong, "Electric field enhancing properties of the V-shaped optical resonant antennas," *Opt. Express* **15**, pp.16852-16859 (2007).

[24] K.-S. Lee and M. A. El-Sayed, "Gold and Silver Nanoparticles in Sensing and Imaging: Sensitivity of Plasmon Response to Size, Shape and Metal Composition," *J. Phys. Chem. B*, **110**, pp.19220-19225 (2006).

[25] B. C. Stipe, T. C. Strand, C. C. Poon, H. Balamane, T. D. Boone, J. A. Katine, J.-L. Li, V. Rawat, H. Nemoto, A. Hirotsune, O. Hellwig, R. Ruiz, E. Dobisz, D. S. Kercher, N. Robertson, T. R. Albrecht, and B. D. Terris,

"Magnetic recording at 1.5 Pb m^{-2} using an integrated plasmonic antenna" *Nat. Photonics* **4**, pp.484-488 (2010).

[26] P. Biagioni, J. S. Huang, L. Duo, M. Finazzi, and B. Hecht, "Cross Resonant Optical Antenna," *Phys. Rev. Lett.* **102**, pp.256801 (2009).

[27] E. Ogut, G. Kiziltas, and K. Sendur, "Circularly polarized localized near-field radiation at the nanoscale," *Appl. Phys. B – Lasers O.* **99**, pp.67-74 (2010).

[28] R. Melik, E. Unal, N. K. Perkgoz, B. Santoni, D. Kamstock, C. Puttlitz, and H. V. Demir, "Nested Meatmaterials for Wireless Stain Sensing," *IEEE J. Sel. Top. Quant.* **16**, pp.450-458 (2010).

[29] A. Taflove, "Application of the Finite-Difference Time-Domain Method to Sinusoidal Steady-State Electromagnetic-Penetration Problems," *IEEE T. Electromagn. C.* **22**, pp.191-202 (1980).

[30] A. Taflove, *Computational electrodynamics: the finite-difference time-domain method.*, Artech House, 2000.

[31] D. Sullivan, *Electromagnetic Simulation Using the FDTD Method.*, IEEE Press, 2000.

[32] R. W. Wood, "On a remarkable case of uneven distribution of light in a diffraction grating spectrum," *Phil. Mag.* **4**, pp.396 (1902).

[33] J. C. M. Garnett, "Colours in metal glasses and in metallic films," *Philos. Trans. R. Soc. London* **203**, pp.385 (1904).

[34] G. Mie, "Beiträge zur Optik trüber Medien, speziell kolloidaler Metallösungen," *Ann. Phys. (Leipzig)* **25**, pp.377 (1908).

[35] D. Pines, "Collective energy losses in solids," *Rev. Mod. Phys.* **28**, pp.184-198 (1956).

[36] R. H. Ritchie, "Plasma losses by fast electrons in thin films," *Phys. Rev.* **106**, pp.874 (1957).

[37] R. H. Ritchie, E. T. Arakawa, J. J. Cowan, and R. N. Hamm, "Surface-plasmon resonance effect in grating diffraction," *Phys. Rev. Lett.* **21**, pp.1530-1532 (1968).

[38] E. Kretschmann, and H. Raether, "Radiative decay of non-radiative surface plasmons excited by light," *Z. Naturf.* **23A**, pp.2135 (1968).

[39] J. Takahara, S. Yamagishi, H. Taki, A. Morimoto, and T. Kobayashi, "Guiding of a one-dimensional optical beam with nanometer diameter,"*Opt. Lett.* **22**, pp.475-478 (1997).

[40] T. W. Ebessen, H. J. Lezec, H. F. Ghaemi, T. Thio, and P. A. Wolff, "Extraordinary optical transmission through subwavelength hole arrays," *Nature (London)* **391,** pp.667-669 (1998).

[41] U. Kreibig, and M. Vollmer, *Optical Properties of Metal Clusters.*, Springer-Verlag, 1995.

[42] C. F. Bohren and D. R. Huffman, *Absorption and Scattering by Small Particles.*, Wiley, 1983.

[43] M. Kerker, *The Scattering of Light and Other Electromagnetic Radiation.*, Academic Press, 1969.

[44] R. K. Chang, and T. E. Furtak, *Surface Enhanced Raman Scattering.*, Plenum Press, 1982.

[45] J. D. Jackson, *Classical Electrodynamics.*, Wiley, 1962.

[46] K. S. Yee, "Numerical Solution of Initial Boundary Value Problems Involving Maxwell`s Equations in Isotropic Media," *IEEE T. Antenn. Propag.* **14,** pp.302-307 (1966).

[47] A. Taflove, and M. E. Brodwin, "Numerical Solution of Steady-State Electromagnetic Scattering Problems Using the Time-Dependent Maxwell`s Equations," *IEEE T. Microw. Theory* **23,** pp.623-630 (1975).

[48] D. R. Lide, *CRC Handbook of Chemistry and Physics.*, CRC Press, 2004.

[49] E. D. Palik, *Handbook of Optical Constants of Solids.*, Academic, 1985.

[50] C. R. Pollock, *Fundamentals of Optoelectronics.*, Richard D. Irwin, 1995.

[51] V. T. Kilic, V. B. Erturk, and H. V. Demir, "Planar optical antennas of split ring resonator as an alternative to dipole antennas for increased field localization," *in submission to Opt. Lett.* (2011).

[52] P. Bharadwaj, B. Deutsch, and L. Novotny, "Optical Antennas," *Adv. Opt. Photon.* **1**, pp.438-483 (2009).

[53] L. Novotny, "Effective Wavelength Scaling for Optical Antennas," *Phys. Rev. Lett*. **98**, pp.266802 (2007).

[54] V. T. Kilic, V. B. Erturk, and H. V. Demir, “Novel Optical Nanoantenna Designs of Comb-shaped Plasmonic Architectures for Increased Field Localization in NIR and MIR,” *Graduate Research Conference.* Bilkent University (2011).